2010-06

Numerical and experimental investigation of performance improvements of a cross-flow fan

Antoniadis, Vlassios.

Monterey, California. Naval Postgraduate School

http://hdl.handle.net/10945/5306

NAVAL POSTGRADUATE SCHOOL

MONTEREY, CALIFORNIA

THESIS

NUMERICAL AND EXPERIMENTAL INVESTIGATION OF PERFORMANCE IMPROVEMENTS OF A CROSS-FLOW FAN

by

Vlassios Antoniadis

June 2010

Thesis Advisor:	Garth V. Hobson
Co-Advisor:	Anthony J. Gannon

Approved for public release; distribution is unlimited

REPORT DOCUMENTATION PAGE		*Form Approved OMB No. 0704-0188*

1. AGENCY USE ONLY *(Leave blank)*	**2. REPORT DATE** June 2010	**3. REPORT TYPE AND DATES COVERED** Master's Thesis

4. TITLE AND SUBTITLE Numerical and Experimental Investigation of Performance Improvements of a Cross-Flow Fan **6. AUTHOR(S)** Vlassios Antoniadis	**5. FUNDING NUMBERS**
7. PERFORMING ORGANIZATION NAME(S) AND ADDRESS(ES) Naval Postgraduate School Monterey, CA 93943-5000	**8. PERFORMING ORGANIZATION REPORT NUMBER**
9. SPONSORING /MONITORING AGENCY NAME(S) AND ADDRESS(ES) N/A	**10. SPONSORING/MONITORING AGENCY REPORT NUMBER**

11. SUPPLEMENTARY NOTES The views expressed in this thesis are those of the author and do not reflect the official policy or position of the Department of Defense or the U.S. Government. IRB Protocol number ________________.

12a. DISTRIBUTION / AVAILABILITY STATEMENT Approved for public release; distribution is unlimited	**12b. DISTRIBUTION CODE**

13. ABSTRACT (maximum 200 words)

The cross-flow fan has an inherent ability to provide thrust to an airfoil as well as provide boundary layer control. The thrust can be easily vectored and usually the cross-flow fan is fully embedded within the airfoil, making its operation relatively safe. Those characteristics make it very favorable as a propulsive means for a vertical takeoff and landing (VTOL) aircraft. However, further design improvements are needed for competitive comparison with existing conventional aircraft propulsion methods.

The baseline configuration was scaled from a 12-inch diameter, 30-bladed rotor developed by Vought Systems in the 1970s to a 6-inch rotor as a more realistic size for integration into a propulsive wing. Using the computational fluid dynamics (CFD) software, ANSYS CFX, previous baseline configuration models were validated at full-speed range to verify the software's prediction. Then, a model with the cross-flow fan embedded at the trailing edge was built and different configurations were examined. An attempt was made to improve the performance of the cross-flow fan embedded airfoil by thrust and thrust-to-power ratio, and lift and drag forces were calculated.

CFD results have shown that a rotor with fewer blades can improve performance and a 22-bladed rotor was selected and examined experimentally. Results were compared with the baseline 30-bladed rotor.

14. SUBJECT TERMS Fan, Cross Flow, Propulsive Wing, Thrust Vectoring, Casing Configurations, Blade Geometry	**15. NUMBER OF PAGES** 125
	16. PRICE CODE

17. SECURITY CLASSIFICATION OF REPORT Unclassified	**18. SECURITY CLASSIFICATION OF THIS PAGE** Unclassified	**19. SECURITY CLASSIFICATION OF ABSTRACT** Unclassified	**20. LIMITATION OF ABSTRACT** UU

NSN 7540-01-280-5500 Standard Form 298 (Rev. 2-89)
Prescribed by ANSI Std. 239-18

THIS PAGE INTENTIONALLY LEFT BLANK

NUMERICAL AND EXPERIMENTAL INVESTIGATION OF PERFORMANCE IMPROVEMENTS OF A CROSS-FLOW FAN

Vlassios Antoniadis
Lieutenant Junior Grade, Hellenic Navy
B.S., Hellenic Naval Academy, 2002

Submitted in partial fulfillment of the
requirements for the degree of

MECHANICAL ENGINEER
and
MASTER OF SCIENCE IN MECHANICAL ENGINEERING

from the

NAVAL POSTGRADUATE SCHOOL
June 2010

Author: Vlassios Antoniadis

Approved by: Garth V. Hobson
Thesis Advisor

Anthony J. Gannon
Co-Advisor

Knox T. Millsaps
Chairman, Department of Mechanical and Aerospace Engineering

THIS PAGE INTENTIONALLY LEFT BLANK

ABSTRACT

The cross-flow fan has an inherent ability to provide thrust to an airfoil as well as provide boundary layer control. The thrust can be easily vectored, and the cross-flow fan usually is fully embedded within the airfoil, making its operation relatively safe. Those characteristics make it very favorable as a propulsive means for a vertical takeoff and landing (VTOL) aircraft. However, further design improvements are needed for competitive comparison with existing conventional aircraft propulsion methods.

The baseline configuration was scaled from a 12-inch diameter, 30-bladed rotor developed by Vought Systems in the 1970s to a 6-inch rotor as a more realistic size for integration into a propulsive wing. Using the computational fluid dynamics (CFD) software, ANSYS CFX, previous baseline configuration models were validated at full-speed range to verify the software's prediction. Then, a model with the cross-flow fan embedded at the trailing edge was built and different configurations were examined. An attempt was made to improve the performance of the cross-flow fan embedded airfoil by thrust and thrust-to-power ratio, and lift and drag forces were calculated.

CFD results have shown that a rotor with fewer blades can improve performance and a 22-bladed rotor was selected and examined experimentally. Results were compared with the baseline 30-bladed rotor.

THIS PAGE INTENTIONALLY LEFT BLANK

TABLE OF CONTENTS

LIST OF FIGURES

LIST OF TABLES

THIS PAGE INTENTIONALLY LEFT BLANK

LIST OF ACRONYMS AND ABBREVIATIONS

A	Area [units ^{2}]
ANSYS CFX-Post	Part of the ANSYS CFX package that allows for post-processing of results obtained by ANSYS CFX-Solver
ANSYS CFX-Pre	Part of the ANSYS CFX package for application of boundary and initial conditions as well as solver settings
ANSYS CFX-Solver	Part of the ANSYS CFX package that performs the actual computations and allows for real-time monitoring of the solution status
ANSYS WORKBENCH	Simulation package used to import SOLIDWORKS files, create CFX geometries, meshing, and problem setup for use by CFX-PRE
CAD	Computer-assisted design
CFD	Computational fluid dynamics
CFF	Cross-flow fan
CFL	Courant-Friedrichs-Lewey number—used to indicate stability in solving hyperbolic partial differential equations using an explicit solver; also referred to as Courant number
CFTA	Cross-flow fan test assembly
C_p	Specific heat of air at constant pressure [J/(kg·K)]
C_θ	Tangential component of absolute velocity; further subscripts denote particular location (blade entrance, blade exit)
DSA	Digital sensing array
δ	Non-dimensional total pressure correction term
F_{Thrust}	Thrust [F]
GUI	Graphical user interface
γ	Ratio of specific heats at constant pressure and constant volume

HPC	High-pressure cavity—referred to as “Secondary Vortex Cavity” in Ref [11]
h	Enthalpy
IGV	Inlet guide vane
k	Turbulent kinetic energy Equation (6)
LPC	Low-pressure cavity—referred to as “Primary Vortex Cavity” in Ref [12]
M	Mach Number
$\dot{m}$	Mass flow rate [kg/sec]
NACA	National Advisory Committee for Aeronautics (predecessor of NASA)
NPS	Naval Postgraduate School
N	Shaft speed [rpm]
η	Efficiency
u	Velocity in the u or x direction, subscript denotes particular location
P	Pressure
P_t	Total pressure
$\overline{P}_t$	Mass-averaged total pressure
π	Non-dimensional ratio of mass-averaged total pressure at outlet to total pressure at inlet
ρ	Density
SOLIDWORKS	Three-dimensional drafting and solid modeling software package
STOL	Short takeoff and landing
S_E	Energy source Equation (3)
S_M	Momentum source Equation (2)
T	Temperature [K]

T_t	Total temperature; further subscripts denote particular location
$\overline{T}_t$	Mass-averaged total temperature
TPL	Turbopropulsion Laboratory
TTR	Turbine test rig
τ	Non-dimensional ratio of mass-averaged total temperature at outlet to total temperature at inlet
θ	Non-dimensional total temperature correction term
UAV	Unmanned aerial vehicle
V	Velocity
U	Velocity Equation (1)
υ	Velocity in the y direction
VSD	Vought Systems Division
VTOL	Vertical takeoff and landing
X_i	Non-dimensional velocity at location *i*
6D	6-inch diameter (0.1524 [m])
6D1.5L	6-inch diameter, 1.5-inch span
12D	12-inch diameter
12D1.5L	12-inch diameter, 1.5-inch span
λ	Thermal conductivity Equation (3)
μ	Dynamic viscosity Equations (3), (6), (7)
μ_t	Turbulent viscosity Equations (5), (6), (7)
ε	Viscous dissipation

ACKNOWLEDGMENTS

I would like to express my gratitude and appreciation to the following people:

Professor Garth Hobson, for his great cooperation. I sincerely appreciate his endless knowledge, interest and enthusiasm in the laboratory.

Dr. Antony Gannon, for his assistance in CFD programming and for his great advice in every difficulty I had.

John Gibson, for making the experiment run smoothly every day and for maintaining the test rig properly.

Professor Max Platzer, for his great teaching in class and for sparking my interest in aeronautics and fluids science.

All my predecessors who have worked on cross-flow fans. We were able to use their results for further investigation and improvements.

The Hellenic Navy for giving me the opportunity to complete my studies.

Finally, I express my gratitude to my wife, Anastasia Chondrogianni, and to my children, Eirini and Evelina, for their support and understanding.

THIS PAGE INTENTIONALLY LEFT BLANK

I. INTRODUCTION

A. BACKGROUND

In recent years, there has been a growing desire for an air vehicle able to transport passengers with the convenience of a common car. Continuous development in other areas, such as avionics, lightweight airframes and engines with high power-density characteristics, enhances the idea of “highways in the sky.” This type of car would be a valuable solution to surface traffic congestion in overpopulated cities. It could also have other roles where conventional transportation means fail. A prototype named Sky-Car was developed by Moller [1], which uses four ducted fans to produce both lift and thrust. However, the Sky-Car has lower flight efficiency than a fixed-wing aircraft.

Many prototypes exist for vertical takeoff and landing (VTOL) aircraft, and the cross-flow fan (CFF) is one propulsive device with strong potential for this application. Characteristics like simplicity in construction, dimensional length-scalable rotor and easy thrust-vectoring are only a few factors that make its application very attractive. CFF as a propulsive device retains the advantages of both a ducted lift fan and a fixed-wing aircraft, as it has the advantage of shielding users and bystanders compared with external rotating blades as found on helicopters, turboprops and commercial jets. That is especially true when it is embedded in a fixed, propulsive wing. Fanwing [2] and Kummer [3], [4], [5] from Syracuse University, as well as Gologan, Mores, Steiner, and Seitz [6], have investigated the application of a CFF in the trailing or leading edge of a wing.

Vough Systems Division (VSD) [7] of LTV Aerospace Corporation in the mid- to late-1970s first explored different configurations of the CFF concept for the development of a low subsonic aircraft. A 12-inch (30.48 cm) rotor with 30 blades was tested and it was found that, among forty-six different configurations, an inlet arc angle of 105^0 and an exit duct height of 4.6 inches (11.68 cm), as shown in Figure 1, was one of the optimal candidates. Later research at Naval Postgraduate School (NPS) by Seaton [8], Cheng [9], Schreiber [10], Yu [11], Ulvin [12], and Cordero [13], as well Gannon, Utschig, Hobson, and Platzer [14], incorporated the performance characteristics of a 6-inch diameter rotor with 30 double circular arc blades.

The CFF is not restricted only to aviation applications; for many years, CFFs have been used in commercial and industrial applications, primarily to move air in a linear fashion producing a long, thin airstream. CFF was first patented by Mortier [15] in 1893. CFF applications can be seen from computer-cooling air-conditioning to “air curtains” that maintain heating and cooling boundaries. Another invention, from Kummer [5], is a personal ventilation and filtration system using CFF technology to remove dust and allergens from the air in confined spaces.

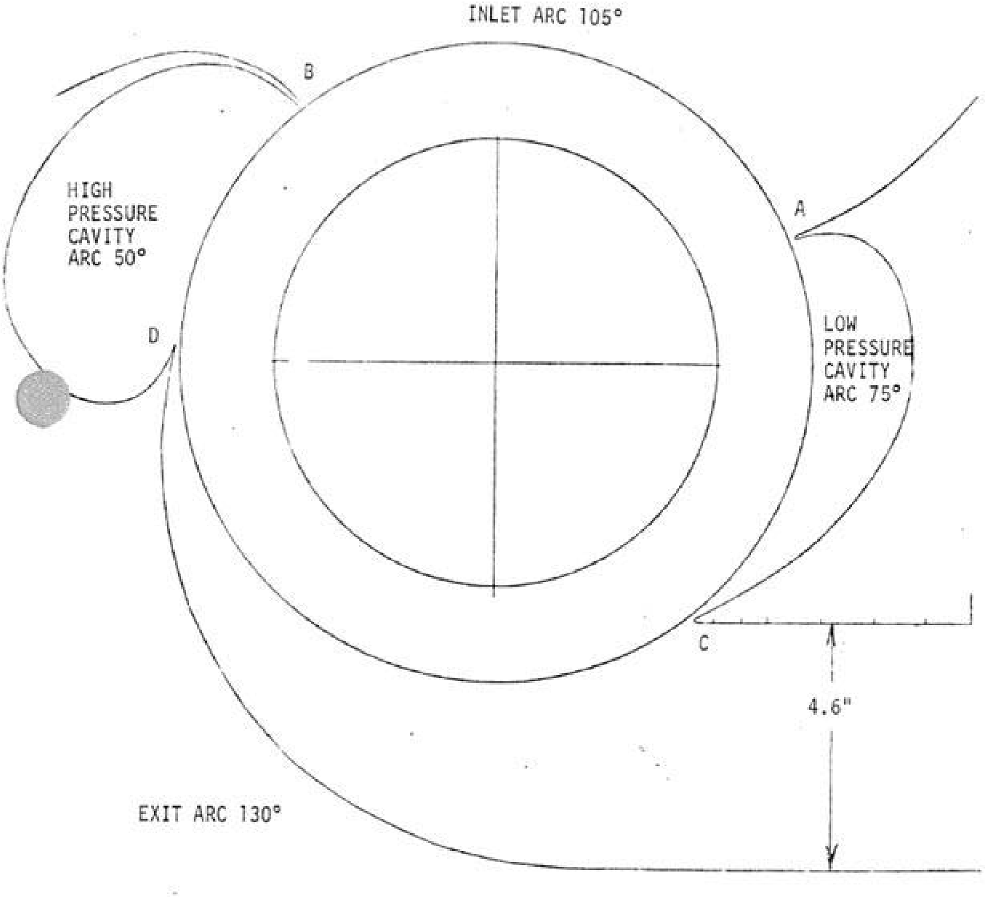

Figure 1. Vought Systems Division (VSD) Multi-Bypass Ratio Propulsion System Fan Housing #6 (Counterclockwise Rotation). From [7]

B. RESEARCH AIMS

The design target depends on the purpose of the application being pursued. Sometimes higher thrust is more important, whereas other times efficiency has a major role. The characteristics of thrust, pressure ratio, efficiency, and thrust-to-power ratio (T/P) are contradictory, and one cannot increase all of them to the desired levels with one single design geometry. For example, where higher lift is needed the pressure ratio and thrust are more important than the efficiency, which is more important for range.

The aim of this thesis was to improve the performance of a CFF embedded in an airfoil by considering various housing configurations, location of the rotor in the airfoil and number of rotor blades.

C. CURRENT STUDY

At the Naval Postgraduate School, a verification of VSD's results was started in addition with numerical computational fluid dynamics (CFD) models. At this point, some important results from previous investigations will be referred. Cheng [9] found that the efficiency was highest with the low-pressure cavity (LPC) closed and the high-pressure cavity (HPC) open. When both cavities were closed, a decrease in the total pressure ratio was observed, but an increase in efficiency was noted when compared to the case of both cavities open. The same result was also computed by Kummer [3].

Scaling laws from Gannon, Utschig, Hobson, and Platzer between the 12-inch (30.48 cm) and 6-inch (15.14 cm) rotors were verified [14]. Schreiber [10] made CFF comparisons of different span length, one of 1.5-inch span (6D1.5L) and the other of 6-inch span length (6D6L) at speeds 2,000, 3,000, 4,000, and 4,500 revolutions per minute (rpm) and concluded the following:

- 1:1 ratio between both fans in terms of specific thrust per unit length
- 0.86 ratio (6D1.5L to 6D6L) of mass flow rate per unit span
- 0.96 ratio (6D1.5L to 6D6L) of thrust to power per mass flow rate per unit span
- 3–9% higher efficiencies, generally, for the 6D6L CFF vs. the 6D1.5L CFF

An attempt was made by Cordero [13] to increase the thrust of the CFF by incorporating inlet guide vanes at the inlet of the CFF. This theoretically can be achieved by changing the inlet tangential velocity components, and so from Equation 6 Cordero [13], the pressure ratio. Assuming constant mass flow rate with the use of the inlet guide vane (IGV), the increase in pressure means higher exit velocity and so higher thrust. The concept of using IGVs did not have the desired results because of higher losses being induced and the dramatic reduction in efficiency. At 3,000 rpm and open throttle condition, a CFD model simulation with IGVs predicts a 15% reduction in efficiency, from 64 % to 49%.

II. COMPUTATIONAL MODEL

A. OVERVIEW

Previous studies from Yu [11] and Cordero [13] have treated the CFF simulation with CFD successfully. Although Yu's model results were close to the experimental results, the computational model was quite complex, as it utilized a hybrid structured grid, and was not appropriate for a parametric study. On the other hand, Cordero's model, in an effort to reduce the computational time, treated the flow as two-dimensional (2-D); he chose a thinned rotor solid disk of 1/16 inch (1.59 mm) thickness. Cordero's model was able to treat the casing domain of CFF as 2-D, but not the rotor domain. Although the computational model was improved, it was still difficult for use in parametric study.

The procedure, as regards the solution of each case, involves the following steps. First, each model was designed in a computer-assisted drafting (CAD) program like SOLIDWORKS and then exported to the ANSYS-CFX meshing tool for grid generation. That mesh was then imported into ANSYS-CFX Pre, for setting the suitable boundary conditions and the solution parameters as described in detail in Appendix A. Once the changes in ANSYS-CFX Pre were saved, a new definition file (*.def) was created for later import into ANSYS-CFX Solver. That file was the starting point in each simulation and the subsequent results were processed in ANSYS-CFX Post.

B. GEOMETRY AND GRID GENERATION

Initially, geometric models were created in SOLIDWORKS. These solid models consisted of two major parts, the 6-inch rotor domain with a 1/16-inch span, and the casing domain with the same span length. The casing domain accommodated the rotor with its blades. Then each individual part was exported to ANSYS-WORKBENCH for grid generation. The result is two separate grid files (*.cmdb), which are assembled in ANSYS-CFX Pre in order to construct the whole CFF configuration.

The advantage of this strategy is the ability to control the grid quality in each domain separately. For example, in the rotor domain, a more dense mesh was used, since blades encompassed steep curves compared with the casing domain, where the geometry was much simpler. In the same way, the number of elements was chosen and point-control application could also be used. Because the CFF model was 2-D, and in order to improve the meshing from the default CFX ANSYS WORKBENCH, a way had to be found to also make a 2-D mesh in the span-wise direction for the rotor domain.

Initially, on working with the thin 6-inch diameter (15.24 cm) rotor disk from Cordero [13], it was realized that a 2-D mesh extraction from the default 3-D was not possible. An investigation found that in the curve points of the double circular arc airfoil, there were some erroneous points near the extremities of the rotor (outer tip radius). In reality, those points were outside of the rotor domain, as can be demonstrated from Figure 2 in MATLAB and Appendix B. The same can be seen from SOLIDWORKS in Figure 3. It is believed that scaling down from 12-inch diameter to 6-inch diameter produced that interpolation error at the outer tip edge of the blade airfoil. Also, it is the main reason why the CFX ANSYS WORKBENCH meshing tool did not permit the generation of a 2-D mesh on the rotor. After that observation, a new model was generated by extruding the plain thin disk in SOLIDWORKS with the entire blade within it (Figure 4).

In SOLIDWORKS, an extruded cut is not possible out of a closed curve previously designed on a plane with the composite curve feature tool. In order to proceed with the extruded cutout of the blade, it was necessary to proceed manually point-by-point constructing the four curves (corresponding to the inner tip edge, suction side, pressure side and outer tip edge). The faulty outer tip edge points were corrected at the same time (Appendix B). The points between the airfoil were connected using splines and a smoothing tool was also used for the curves (curvature control). The result is a new thin rotor disk (Figure 4). In Figure 5, we can see the 2-D meshing generation of the thin rotor disk (1/16 inch), and in Figure 6 the mesh for the casing domain is shown. These meshes were refined, resulting in 36,383 elements for rotor domain and 8,747 for the casing domain (= 45,130 total, 3.3 times coarse). The default coarse grid contains 12,112 elements for the rotor and 1,633 elements for the casing domain. Refinement of the grid gives us satisfactory results regarding expected pressure ratio, efficiency and mass flow rate predictions. Also, the solution is grid independent, verified by increasing the number of elements. The above slightly coarse refinement will be used for the full-speed range modeling and it is less computationally intensive.

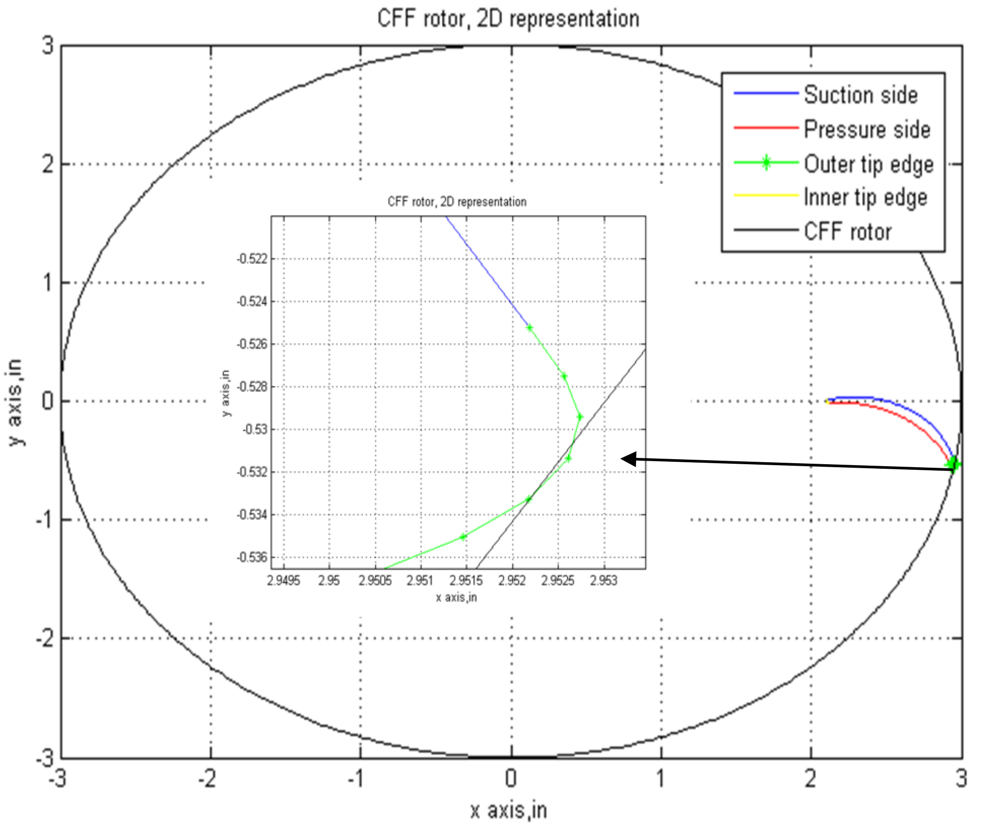

Figure 2. General 2-D Representation in MATLAB of CFF Rotor Domain With One Blade and With Fault Outer Tip Radius Detail

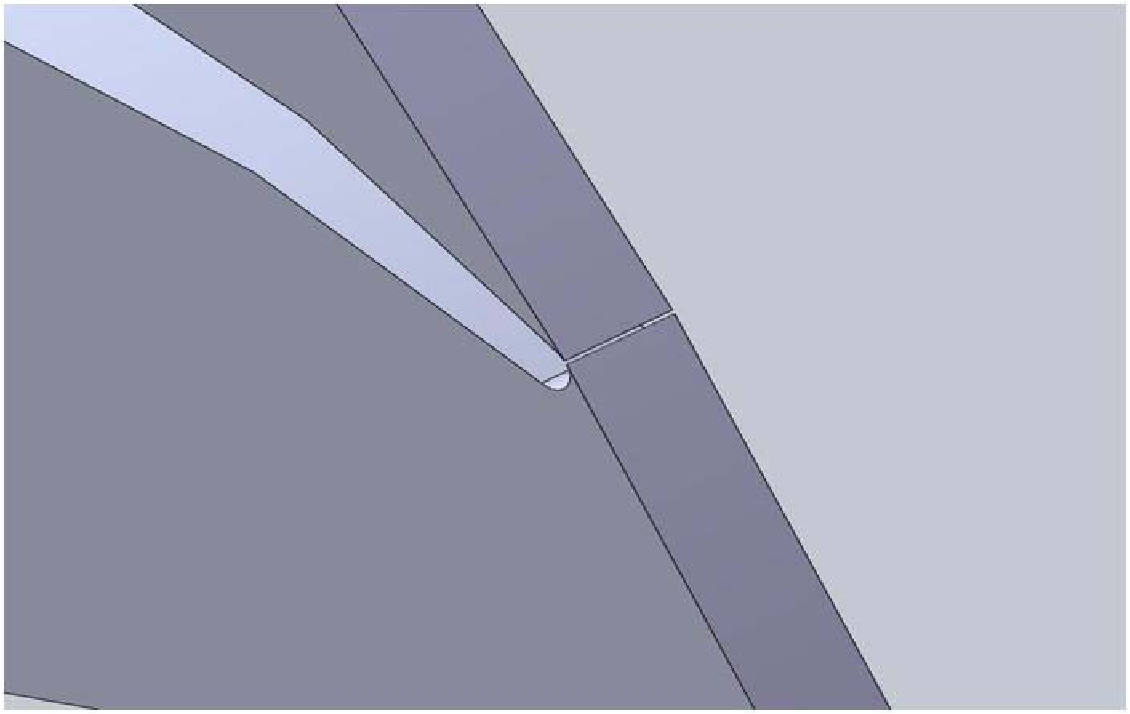

Figure 3. Fault Outer Tip Edge of Double Circular Arc Airfoil

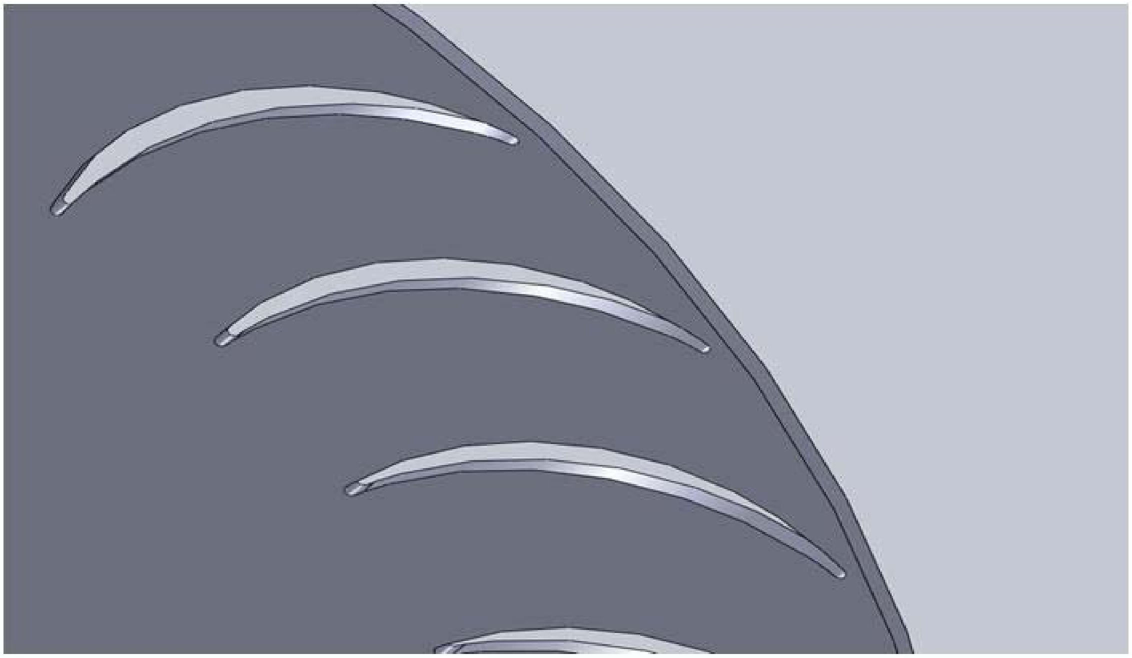

Figure 4. Corrected Airfoil Geometry of Thin Rotor Disk

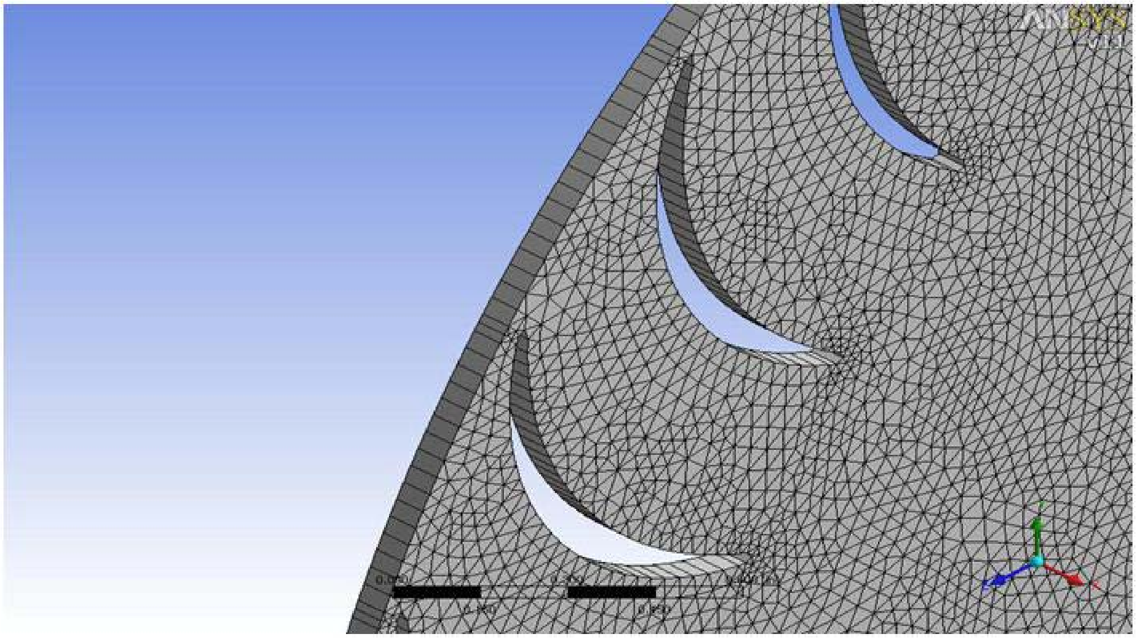

Figure 5. Two-Dimensional (2-D) Meshing (Rotor 36,383 elements) in ANSYS CFX Mesh Tool, Without Inflated Layers

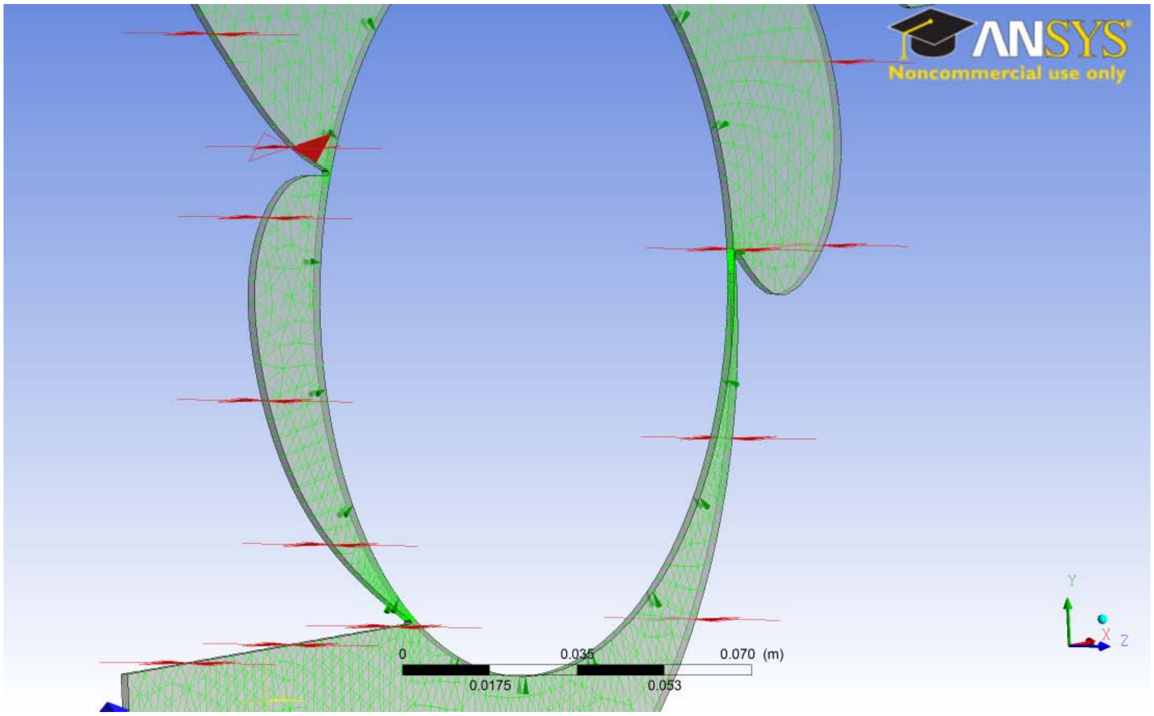

Figure 6. Two-Dimensional (2-D) Meshing (Casing 8,747) in ANSYS CFX Mesh Tool, Without Inflated Layers

Also, the boundary layers in the grid were not inflated in the rotor and casing domain to reduce the computation time. Although this is less accurate, it does give satisfactory results as will be demonstrated in Table 3, paragraph II.D.

C. METHODOLOGY AND BOUNDARY CONDITIONS

The methodology used for the simulations was the same as that used previously by Yu [11] and Cordero [13], and is reintroduced at this point for completeness.

The CFF flow field is transient and not steady-state, due to the continuous rotation of the rotor. Due to the transient nature of the problem, the interface between rotor and stator was selected as “Transient Rotor-Stator” in ANSYS-CFX. Typically, the solver of the transient model needs the specification of some initial values by the user. That can be skipped by selecting transient initialization override. The fluid was selected as air-ideal gas with constant specific heat at constant pressure. The reference pressure was set at one atmosphere. The inlet was specified as a free opening, because at start-up an uncertainty exists regarding the flow direction. Static temperature at inlet and outlet was specified as 300K. The no slip condition was selected for the wall surfaces, including the blade, while turbulent intensity factor was set at 5% for both inlet and outlet.

The center of rotation was the center of the rotor disk around the vertical axis which is parallel to the z-axis. Special care had to be given when defining the rotor speed to ensure the correct direction of rotation (positive or negative, depending on the flow direction). The parameters for the total energy model and k-epsilon turbulence model were selected in order to include heat transfer and turbulence phenomena. The automatic time stepping method was used similar to Cordero [13] in contrast to Yu [11], who used fixed time steps. An initial time step was set at 8e-6 seconds with the option of RMS Courant number selected and set equal to unity for time accuracy. Equations that the solver uses include continuity, momentum, energy, turbulence eddy dissipation, turbulent kinetic energy, and an equation of state. These are:

Continuity equation:

$$\frac{\partial \rho}{\partial t} + \nabla \bullet (\rho U) = 0 \tag{1}$$

Momentum equation:

$$\frac{\partial \rho U}{\partial t} + \nabla \bullet (\rho U \otimes U) = \nabla \bullet (-p\delta + \mu(\nabla U + (\nabla U)^T)) + S_M \tag{2}$$

Energy equation:

$$\frac{\partial \rho h_{tot}}{\partial t} - \frac{\partial p}{\partial t} + \nabla \bullet (\rho U h_{tot}) = \nabla \bullet (\lambda \nabla \mathrm{T}) + \nabla \bullet (\mu \nabla U + \nabla U^T - \frac{2}{3} \nabla \bullet U \delta U) + S_{\mathrm{E}} \tag{3}$$

$$h_{tot}(p,T) = h_{stat}(p,T) + \frac{1}{2} U^2 \tag{4}$$

Turbulent eddy viscosity:

$$\mu_t = C_\mu \rho \frac{\kappa^2}{\varepsilon} \tag{5}$$

Turbulent kinetic energy:

$$\frac{\partial(\rho k)}{\partial t} + \nabla \bullet (\rho U k) = \nabla \bullet \left[\left(\mu + \frac{\mu_t}{\sigma_\kappa} \right) \nabla k \right] + P_k - \rho\varepsilon \tag{6}$$

Turbulence Eddy Dissipation:

$$\frac{\partial(\rho\varepsilon)}{\partial t} + \nabla \bullet (\rho U \varepsilon) = \nabla \bullet \left[\left(\mu + \frac{\mu_t}{\sigma_\varepsilon} \right) \nabla \varepsilon \right] + \frac{\varepsilon}{\kappa} (C_{\varepsilon 1} P_\kappa - C_{\varepsilon 2} \rho \varepsilon) \tag{7}$$

The equation of State:

$$\rho(p,T) = \frac{w(p + p_{ref})}{R_0 T} \tag{8}$$

The above equations contain five proportionality constants (C_μ, σ_κ, σ_ε, $C_{\varepsilon 1}$, $C_{\varepsilon 2}$). The standard κ-ε model from Reference [16] employs values that arrived by comprehensive data fitting. Those are $C_\mu = 0.09$, $\sigma_\kappa = 1$, $\sigma_\varepsilon = 1.3$, $C_{\varepsilon 1} = 1.44$, $C_{\varepsilon 2} = 1.92$. In Equation (3), δ is the Kronecker delta term from [16].

D. SIMULATION PLANS

1. Validation of Baseline Configurations Plans

As previously shown, the CFF model was treated successfully as a 2-D model. Both the casing and the rotor domain in the ANSYS-CFX were extruded successfully in a 2-D manner instead of the default 3-D. Also, the number of periodic layers in the 2-D model was defined as one (span direction), see Figures 5 and 6. Since the model behaves linearly in the span-wise direction, there is no reason for more than one periodic layer. The time for each simulation was reduced—a fact that allowed more parametric studies in order to improve the design objective(s).

An effort was made to verify in the CFD environment the experimental data from Cordero [13]. This is due to the fact that the 2-D grid drastically reduced the computational time. For that reason, four different configurations were selected, which are the following (Figure 8):

- CFF Configuration (1): vertical inlet with both cavities open, baseline configuration
- CFF Configuration (2): horizontal inlet with both cavities open
- CFF Configuration (3): horizontal inlet with cavities blanked off
- CFF Configuration (4): horizontal inlet without cavities

The above four models were selected to investigate the advantages and disadvantages of each regarding the pressure ratio, efficiency, thrust, and general overall operating characteristics. Those four configurations will be referred to in this study, by their numbers. Before the presentation of those results, it is worth noting that the difference in terminology between saying that CFF operates without cavities, which is Configuration (4), and saying that CFF operates with the cavities blanked off, which is Configuration (3), Figures 8 (c) and (d), respectively. Although it was expected to get the same results, since eliminating the cavities and observing the mesh characteristics to be the same, this is not very accurate. The slight difference in the entry region caused the model without cavities (Configuration 4) to have less efficiency; it had a higher pressure ratio and higher thrust compared to the model with cavities blanked off (Configuration 3) (Figures 11, 12).

On the other hand, the inlet region in Configuration 3, acted like a nozzle (Figure 8 (c)). The flow accelerated to the inlet and so it is reasonable for it to have a higher efficiency and lower mass flow rate. This observation drove the conclusion to investigate CFF in a CFD environment with cavities blanked off (Configuration 3), where this model compared favorably with from [13, Table 7].

For each configuration, a speed range of 3,000 rpm to 8,000 rpm was selected in 1,000 rpm increments. Speeds higher than 8,000 rpm were avoided because they translate to the transonic flow over the blades. In those regions, there may be higher losses due to the induced shock waves. The mesh statistics are given in Table 1:

Table 1. Mesh Statistics for the Four Configurations of Figure 8

Number of nodes	Configuration 1	Configuration 2	Configuration 3	Configuration 4
Casing Domain	9530	9530	12504	10622
Rotor Domain	39010	39010	39010	39010
All Domains	48540	48540	51514	49632
Number of elements	**Configuration 1**	**Configuration 2**	**Configuration 3**	**Configuration 4**
Casing Domain	8747	8747	9069	8544
Rotor Domain	36383	36383	36383	36383
All Domains	45130	45130	45452	44927

The mesh elements are approximately 3.3 times the default coarse grid of the ANSYS CFX mesh tool. Intentionally, inflation layers were not used in an effort to reduce the computation time. Before that, a test was made showing that there was not a significant error for this model in doing so. Table 3 demonstrates this comparison in the case of Configuration 3 comparing the inflated layer and non-inflated layer cases at 4,000 rpm and open-throttle condition. Also, because it was desirable to make a complete comparison with both experimental and CFD results, each model was used without inflation layers similar to Cordero [13]. The number of calculations was thus reduced dramatically. With Cordero’s model [13], using a 3-D rotor mesh, a single revolution simulation was completed in a day, with the solver running in distributed parallel mode on four processors on a local personal computer. With the final 2-D grid approach, ten revolutions were completed, in two days of computational time on the same local personal computer. When the same model was run on a Cluster (a high-performance supercomputer at NPS) on four processors, the simulation time was further reduced to one day for ten revolutions. The number of ten revolutions was selected because it gave enough time for the transient flow in the CFF to be stabilized and accurately simulate the “steady-state” solution (Figure 7).

In Table 2, the numerical CFD is presented for the above configurations and correspond to Figures 9, 11, 12, and 13. As was expected, the predicted efficiency for the whole speed range was highest for Configuration 3 (CFF horizontal inlet with the cavities blanked off; (Figure 9 (b)). In contrast, Configuration 4 (CFF without cavities) had higher thrust and lower efficiency. These two results are in agreement with Table 7 from [13] and Figures 10 and 11. Also, the mass flow rate per unit meter span was higher in Configuration 4 due to the bigger inlet region (Figure 13) and the same holds for the thrust per unit meter span length (Figure 11 (a)). In addition, the pressure ratio, which plays a key role in VTOL, was highest for Configuration 4 and the next highest was Configuration 2, CFF horizontal inlet with cavities (Figure 9 (a)).

Table 2. Numerical Results from CFD for the Four Design Configurations: (a) Configuration 1: Vertical Inlet With Cavities Open, (b) Configuration 2: Horizontal Inlet with Cavities Open, (c) Configuration 3: Horizontal Inlet with Cavities Blanked off, (d) Configuration 4:Horizontal Inlet Without Cavities

Configuration 1 CFF Vertical Inlet with Cavities, case (a) Figure 8

Speed	mdot/L ((kg/sec)/m)	Press. Ratio	Temper. Ratio	Isentropic Efficiency	Thrust per unit length (N/m)	Power per unit length (W/m)	Thrust/ Power (N/Watts)
Rpm 3,000	3.05039	1.0119	1.00516	0.65398	138.655	5094.91	0.027214
4,000	3.97543	1.0205	1.00913	0.63806	235.784	11947.21	0.019735
5,000	5.13140	1.0343	1.0151	0.64457	393.937	24023.24	0.016398
6,000	6.07590	1.0485	1.02123	0.6425	552.476	40234.45	0.013731
7,000	7.15023	1.0679	1.0301	0.62958	768.674	63807.87	0.012046
8,000	8.07370	1.0876	1.03846	0.63194	984.573	97262.36	0.010122

Configuration 2 CFF Horizontal Inlet with Cavities, case (b) Figure 8

Speed	mdot/L ((kg/sec)/m)	Press. Ratio	Temper. Ratio	Isentropic Efficiency	Thrust per unit length (N/m)	Power per unit length (W/m)	Thrust/ Power (N/Watts)
Rpm 3,000	3.14670	1.0127	1.00586	0.61922	147.576	5661.102	0.026068
4,000	4.16617	1.0225	1.0103	0.62082	259.268	13662.99	0.018975
5,000	5.20056	1.0353	1.01616	0.61736	404.663	26614.17	0.015204
6,000	6.26733	1.0517	1.02286	0.63577	588.738	45814.17	0.012850
7,000	7.26362	1.0704	1.03196	0.61417	794.903	73385.83	0.010831
8,000	8.35527	1.0940	1.04256	0.61085	1054.746	107464.6	0.009814

Configuration 3 CFF Horizontal Inlet with Cavities Blanked Off, case (c) Figure 8

Speed	mdot/L ((kg/sec)/m)	Press. Ratio	Temper. Ratio	Isentropic Efficiency	Thrust per unit length (N/m)	Power per unit length (W/m)	Thrust/ Power (N/Watts)
Rpm 3,000	2.85064	1.0105	1.0045	0.65773	121.055	4239.37	0.028555
4,000	3.8966	1.0197	1.0084	0.66299	226.506	10066.14	0.022501
5,000	4.88283	1.0311	1.0131	0.66901	356.236	19319.69	0.018439
6,000	5.8422	1.0448	1.019	0.6642	511.225	34009.45	0.015031
7,000	6.7483	1.0603	1.025	0.65817	683.874	52629.92	0.012994
8.000	7.7096	1.0793	1.0338	0.65193	894.702	81007.87	0.011044

Configuration 4 CFF Horizontal Inlet without Cavities, case (d) Figure 8

Speed	mdot/L ((kg/sec)/m)	Press. Ratio	Temper. Ratio	Isentropic Efficiency	Thrust per unit length (N/m)	Power per unit length (W/m)	Thrust/ Power (N/Watts)
Rpm 3,000	3.26866	1.0133	1.00623	0.6075	157.287	6746.457	0.023314
4,000	4.46355	1.0247	1.012	0.58458	290.769	16535.43	0.017584
5,000	5.57574	1.0388	1.01873	0.58433	454.939	31766.93	0.014321
6,000	6.49700	1.0532	1.02496	0.59794	619.095	52875.59	0.011708
7,000	7.66929	1.0749	1.03506	0.59473	866.166	84850.39	0.010208
8,000	8.74834	1.0987	1.04676	0.58286	1131.849	112252	0.010083
9,000	9.74299	1.1245	1.0599	0.56913	1413.039	162393.7	0.008701

Table 3. CFD Comparison Results Eliminating Inflated Boundary Layers for Configuration 3 at Open Throttle Condition.

Configuration 3 CFF Horizontal Inlet with Cavities Blanked Off							
Speed	mdot/L (kg/sec)/m)	Press. Ratio	Temper. Ratio	Isentropic Efficiency	Thrust per unit length (N/m)	Power per unit length (W/m)	Thrust/ Power (N/Watts)
Rpm 4,000 Without Inflated Layers	3.8966	1.0197	1.0084	0.66299	226.5065	10066.14	0.022501
Rpm 4,000 With Inflated Layers	3.8896	1.0199	1.0084	0.67249	227.0966	10091.33	0.022504

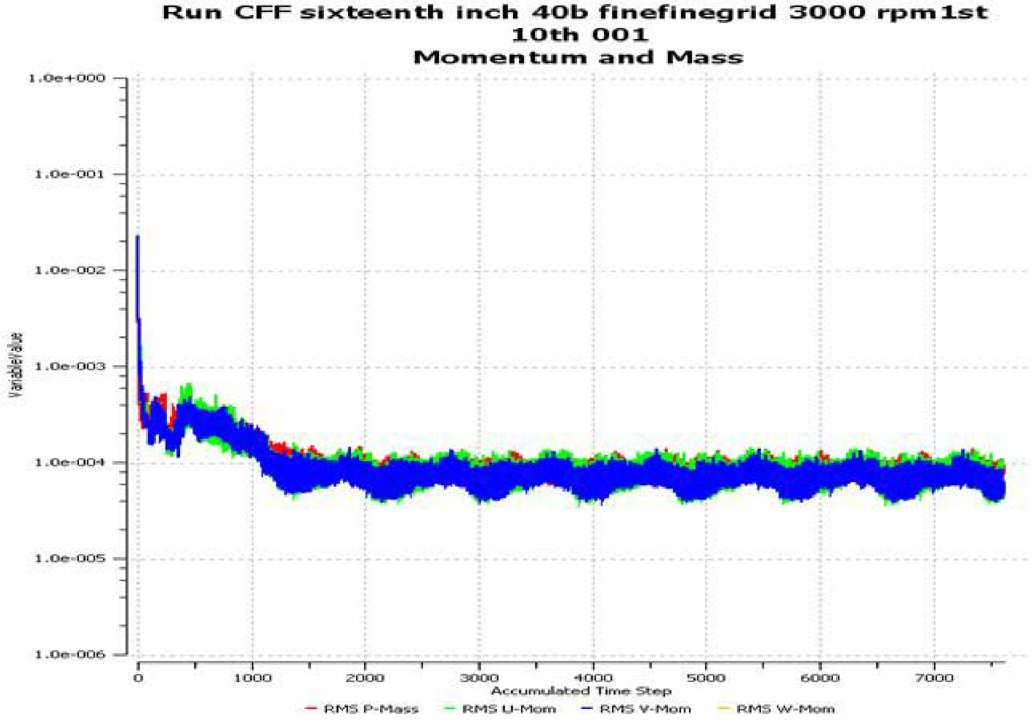

Figure 7. Solver Time History Representation

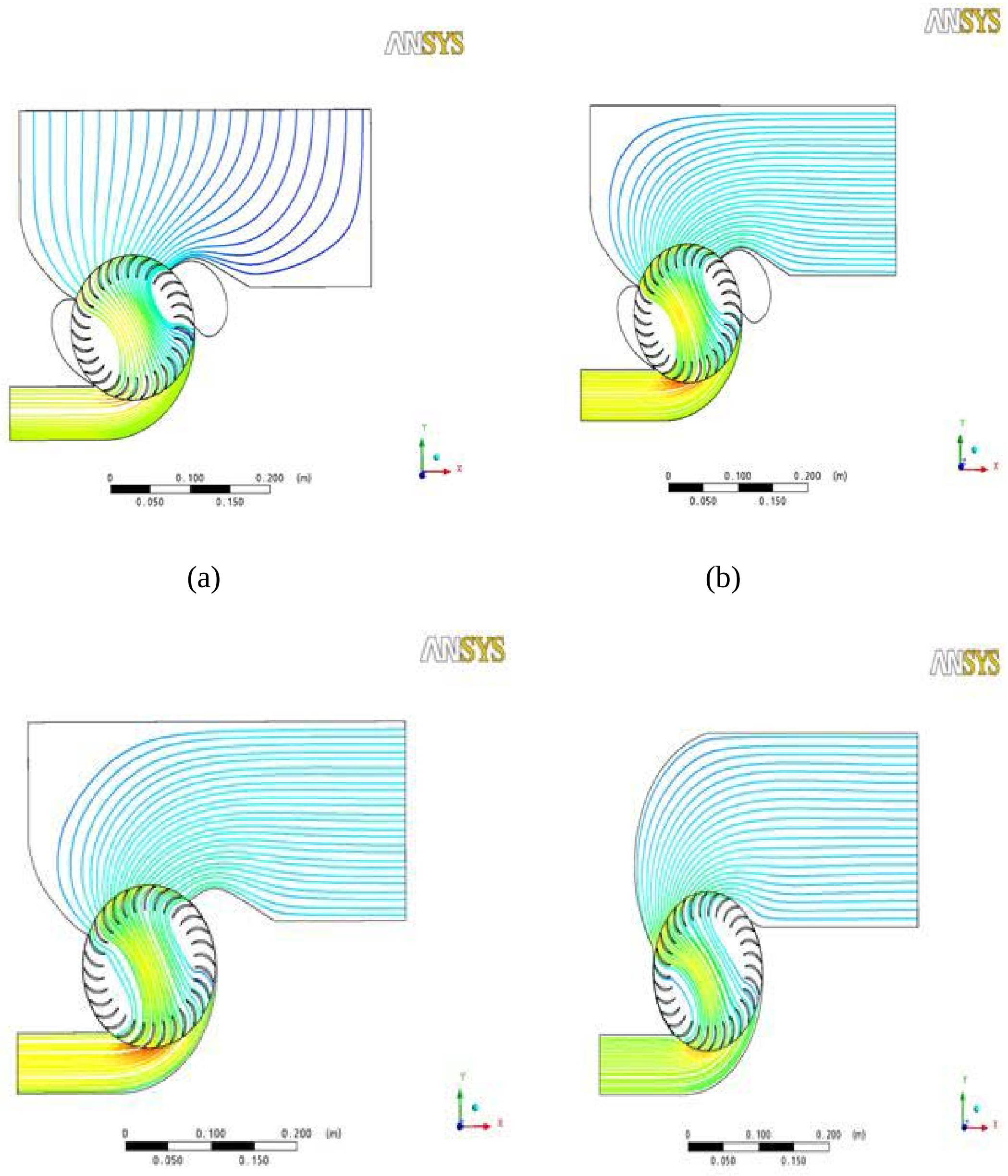

(a) (b)

(c) (d)

Figure 8. Features of the Four Different CFF Configurations With Typical Velocity Streamlines (a) Configuration 1: Vertical Inlet With Cavities Open, (b) Configuration 2: Horizontal Inlet With Cavities Open, (c) Configuration 3: Horizontal Inlet With Cavities Blanked off, (d) Configuration 4:Horizontal Inlet Without Cavities

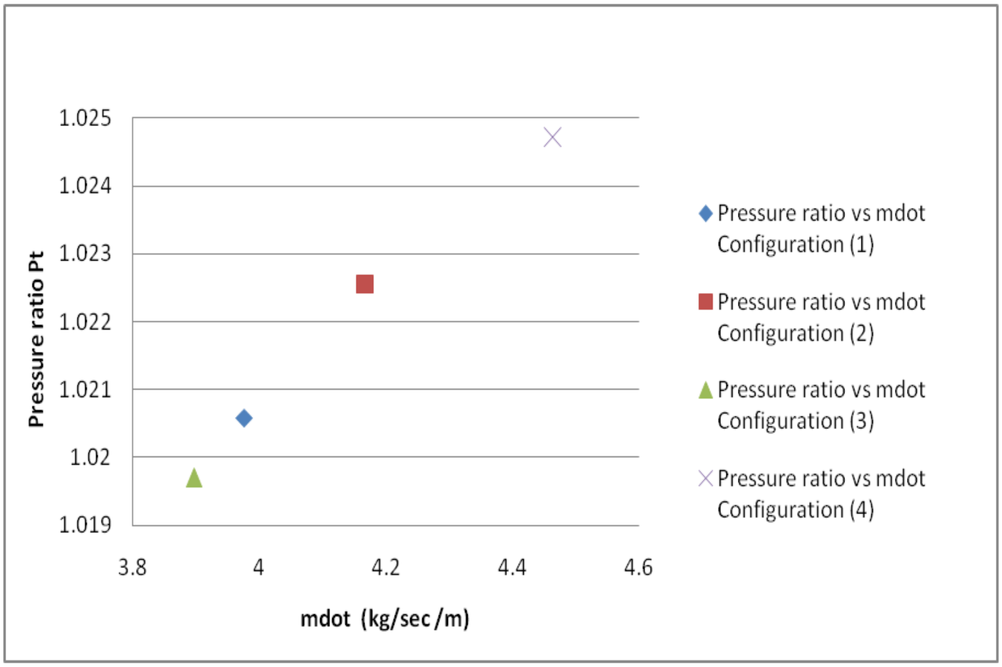

(a)

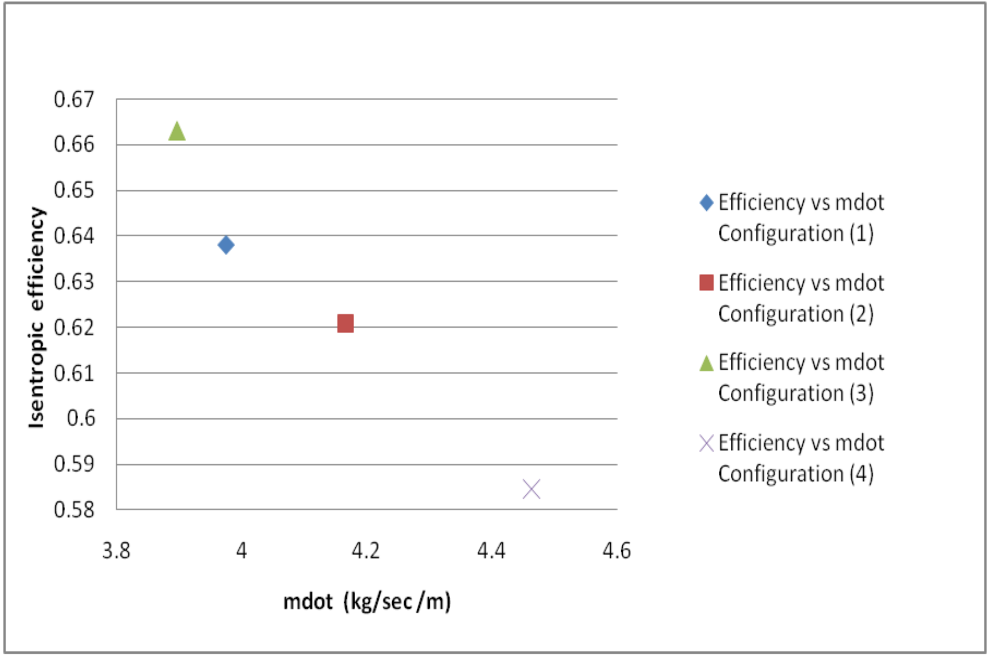

(b)

Figure 9. Numerical CFD Results for the Four Different Configurations at 4,000 rpm (a) Pressure Ratio vs. mdot, (b) Isentropic Efficiency vs. mdot

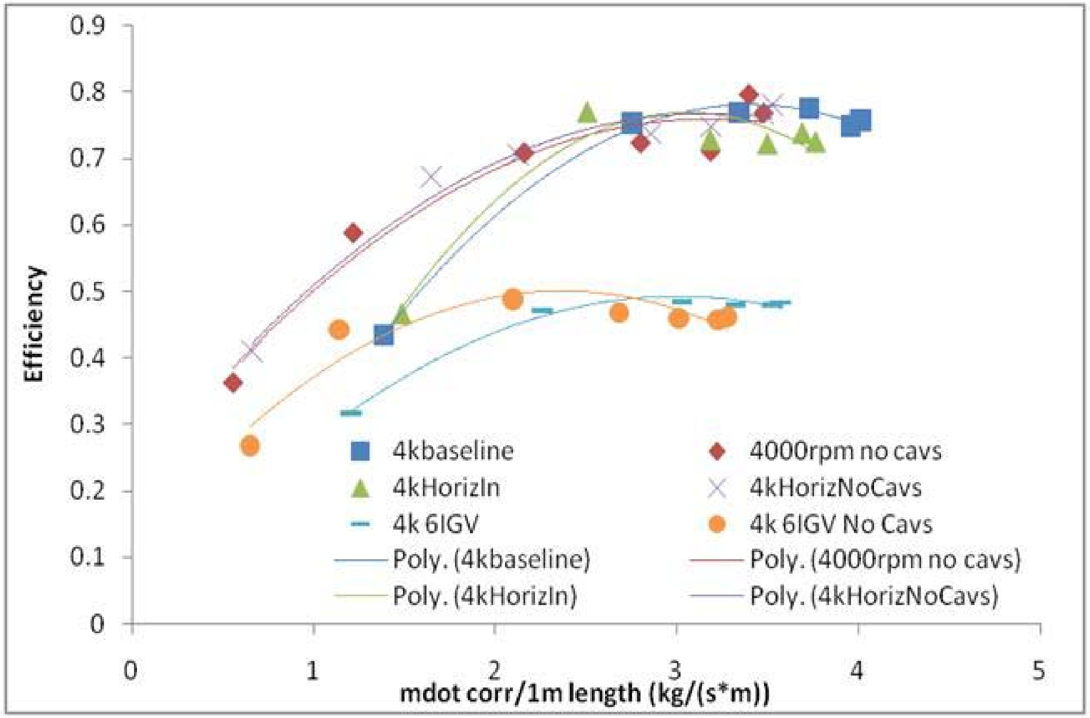

Figure 10. Efficiency for all Experimental Configurations at 4,000 rpm. From [13]

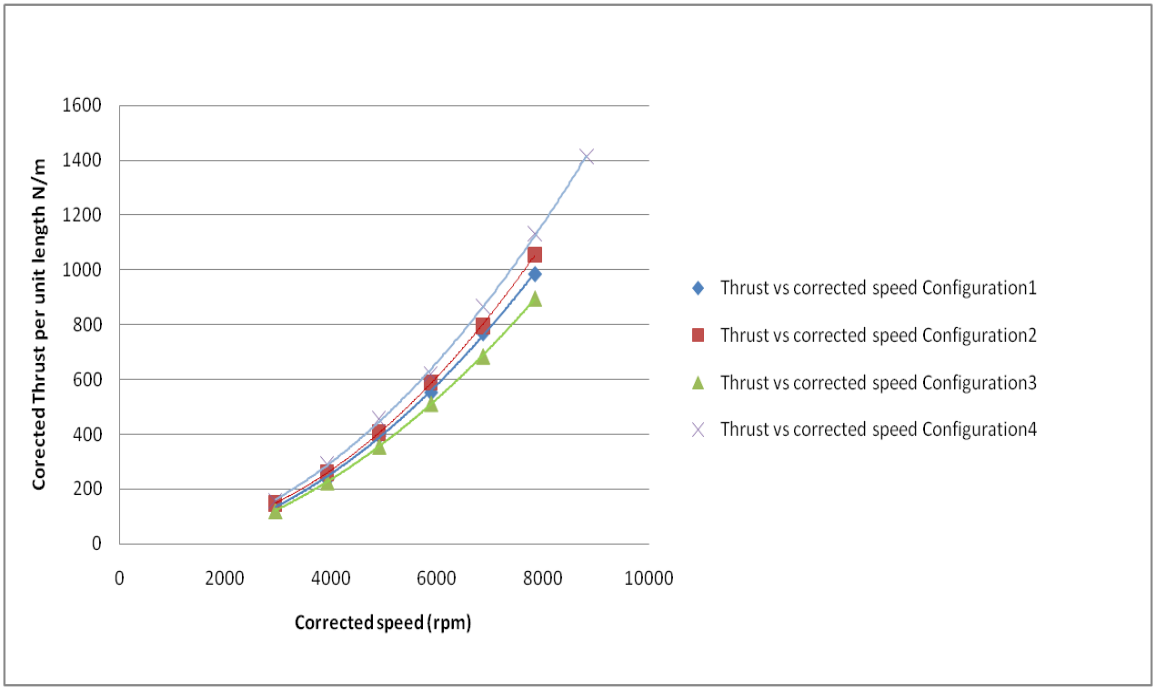

(a)

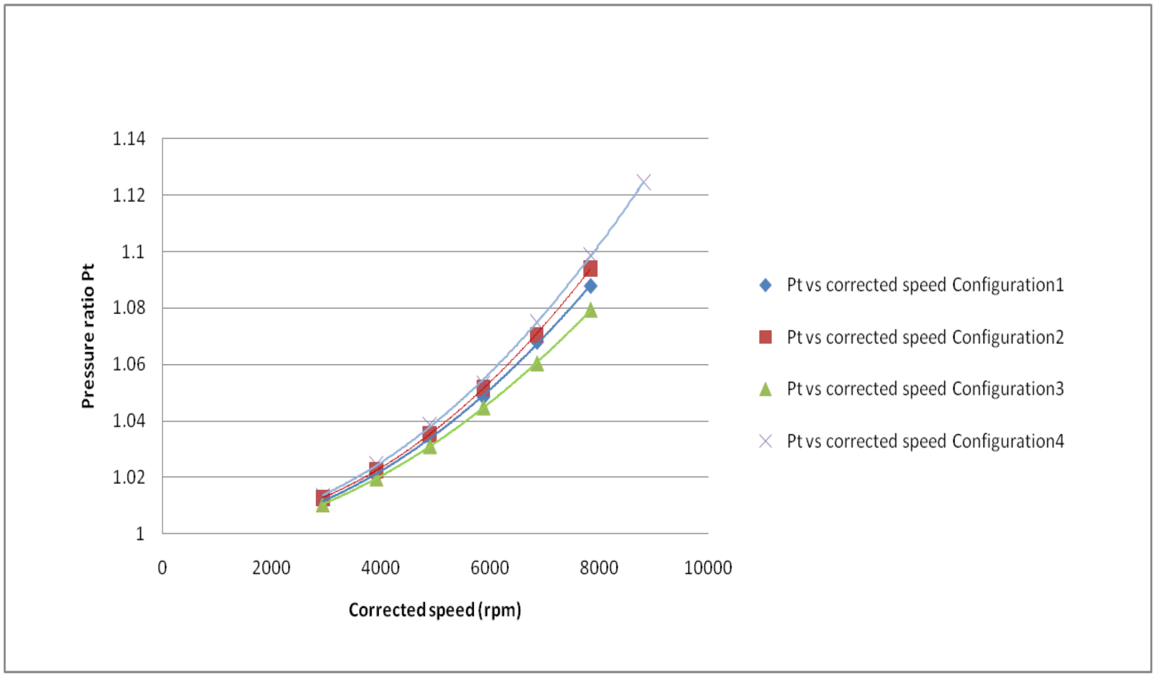

(b)

Figure 11. Numerical CFD Results for (a) Corrected Thrust per Unit Length vs. Corrected Speed, (b) Pressure Ratio vs. Corrected Speed

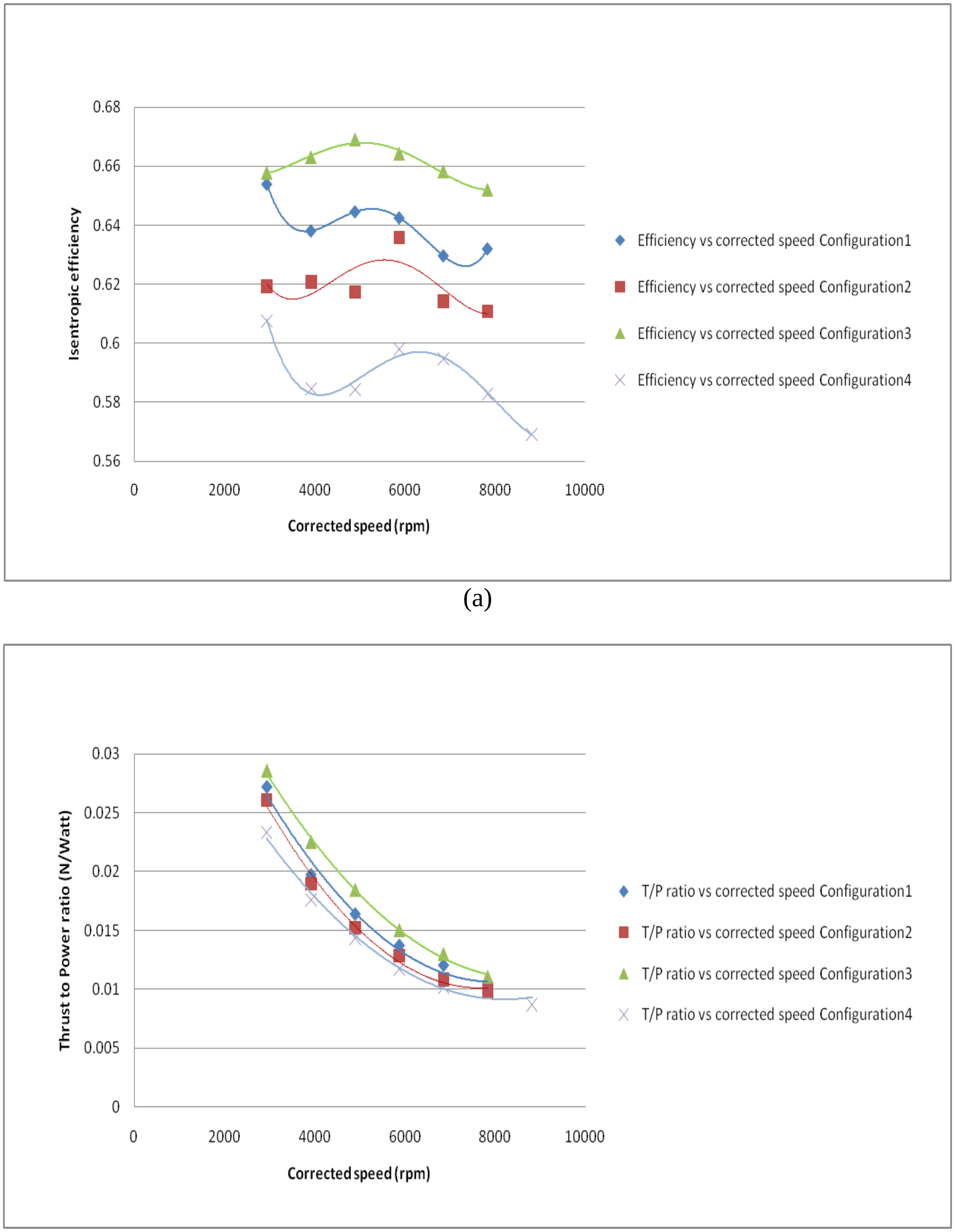

(a)

(b)

Figure 12. Numerical CFD Results for (a) Efficiency vs. Corrected Speed, (b) Thrust to Power Ratio vs. Corrected Speed

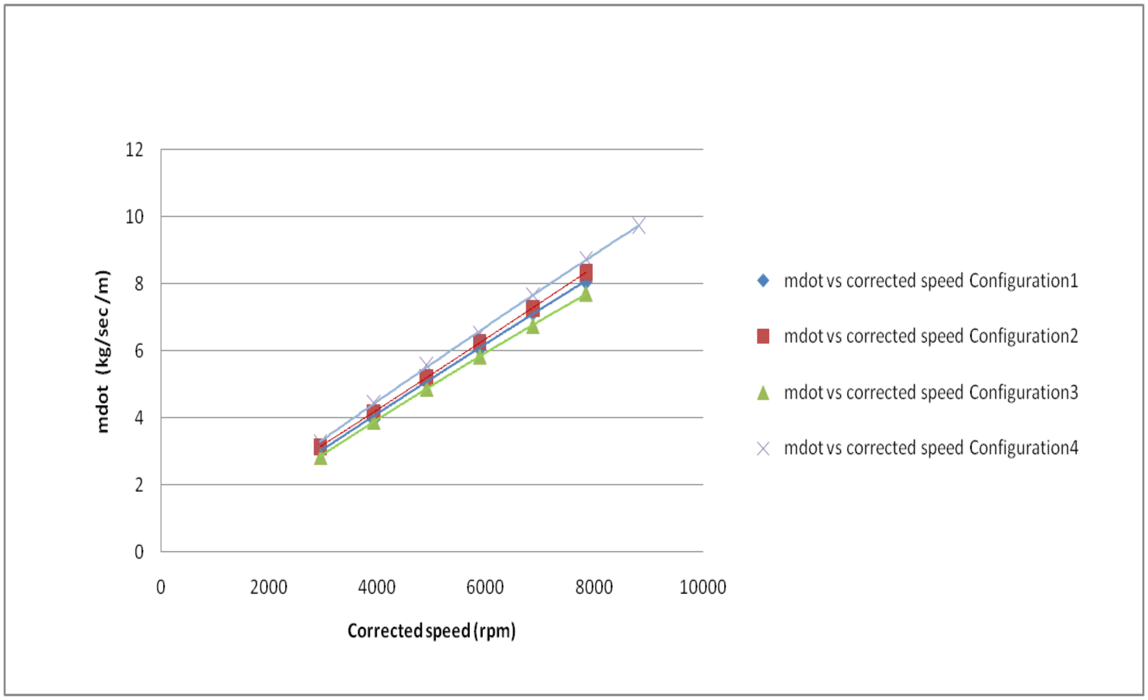

Figure 13. Numerical CFD Results for mdot (kg/sec/m) vs. Corrected Speed

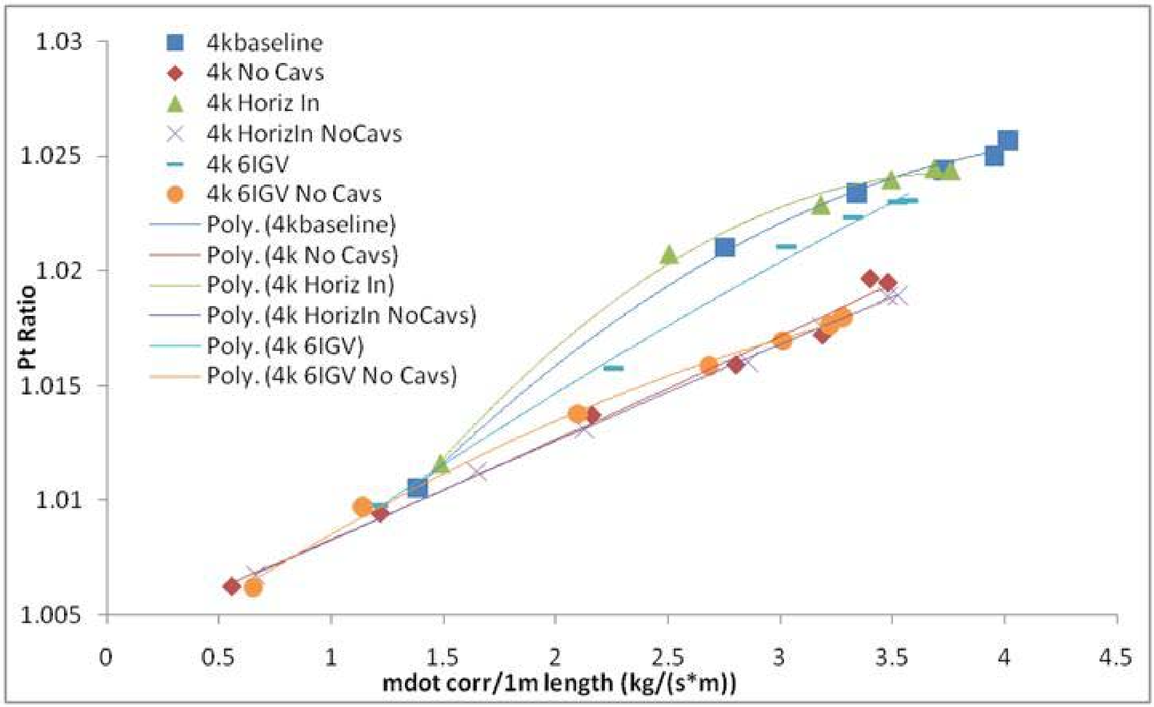

Figure 14. Experimental Results for Different CFF Configurations at 4,000 rpm. From [13]

From Figure 12 (a), it is observed that the higher efficiency is for Configuration 3, but it produced less thrust compared to the other three configurations. Also, regarding efficiency at higher speeds, there was a dramatic reduction for all models. This can be attributed to higher losses at those speeds and compressibility effects. Around 6,000 rpm, a peak in efficiency was computed, which indicated a region of optimum operation for the efficiency and open-throttle condition. In the same way, Figure 9 (a) shows that the prediction of the highest pressure ratio was for Configuration 4 and the next highest was Configuration 2, which was in agreement with experimental data, Figure 14 from [13]. The lowest pressure ratio was for Configuration 3, which for reference [13] was the CFF model with horizontal inlet and cavities blanked off.

As the specific thrust is considered important, from Figure 12 (b), the highest thrust-to-power ratio was for Configuration 3. This is very important regarding the application of CFF embedded in a propulsive wing. That result, in conjunction with the need to save space in an airfoil for fuel or other reasons, makes Configuration 3 very favorable to be embedded in the trailing or leading edge of an airfoil. Also, both higher efficiency and thrust-to-power ratio are translated into reduction of fuel consumption. The only disadvantage is the lower pressure ratio, but with a careful design, it may be possible to achieve higher performance in terms of thrust.

2. CFD Blade Number Investigation

Initially, fewer blades were used in the propulsive wing concept as an increase in performance was observed compared with the 30-bladed rotor. Table 13 section IV.B demonstrates this comparison of NACA 2421 using 30 and 20 blades, respectively. This result drove the idea of parametric investigation into the optimum number of rotor blades. Configuration 3, horizontal inlet CFF with cavities blanked off, (Figure 8 (c)) and open-throttle condition was used because it is the most favorable for application in a propulsive wing. The results from this study are presented in Tables 4 and 5.

Table 4. Numerical Results for Different Number of Rotor Blades, Using Configuration 3 at 4,000 rpm and Open-Throttle Condition, Without High-Speed Numerics.

Num. of blades	Revol. (rpm)	Elem.	mdot/L (kg/sec)/m)	Isentropic efficiency	Thrust per unit length (N/m)	Power per unit length (W/m)	Thrust/ Power (N/W)	Pressure Ratio
Without High Speed Numerics used in the Solver								
30	4,000	45452	3.8966	0.66298	226.506	10068.54	0.022496	1.0197
24	4,000	47469	3.7397	0.69639	208.595	8881.89	0.023485	1.0181
22	4,000	47011	3.675	0.75945	201.299	7899.212	0.025483	1.0175
20	4,000	45659	3.6275	0.69732	196.279	8296.062	0.023659	1.0171
18	4,000	44467	3.4985	0.67541	182.568	7256.692	0.025158	1.0159
16	4,000	44271	3.38878	0.67193	171.311	6777.952	0.025274	1.0149
14	4,000	43195	3.2929	0.6777	161.700	5529.448	0.029243	1.014
10	4,000	46648	2.7993	0.65228	116.751	4090.708	0.028540	1.004
7	4,000	44137	2.27716	0.62256	77.241	2907.08	0.026570	1.0067

Table 5. Numerical Results for Different Number of Rotor Blades, Using Configuration 3 at 4,000 rpm and Open-Throttle Condition, With High-Speed Numerics.

Num. of blades	Revol. (rpm)	Elem.	mdot/L (kg/sec) /m	Isentropic efficiency	Thrust per unit length (N/m)	Power per unit length (W/m)	Thrust/ Power (N/W)	Pressure Ratio
With High Speed Numerics used in the Solver								
30	4,000	45452	3.8346	0.7354	218.55	9669.29	0.022602	1.019
24	4,000	47469	3.686	0.6926	203.23	8541.73	0.023793	1.0177
22	4,000	47011	3.6453	0.6804	198.25	8447.24	0.023469	1.0172
20	4,000	45659	3.653	0.6834	198.00	7439.37	0.026615	1.0172
18	4,000	44467	3.4606	0.6855	178.55	7055.11	0.025307	1.0155

Results in Table 4 were derived without using high-speed numerics in the solver controller. This was intentional, because initially it was thought that at 4,000 rpm compressible flow effects would be small. The highest Mach number value at 4,000 rpm was around 0.2. Indeed, the results using high-speed numerics did not change significantly, except for the efficiency prediction. In Table 4 (without high-speed numerics), the highest efficiency was observed for the 22-bladed rotor, which was contrary to Table 5 (with high-speed numerics on) with the higher predicted efficiency for the 30-bladed rotor. In Figure 17, the difference between the two cases can be seen, whereas in Figure 15 the streamline pattern for Configuration 3 with the 22-bladed rotor is shown. The conclusion from Table 4 was the primary motivation for experimental investigation and manufacture of a new 22-bladed rotor (Figure 16). In the experimental section, comparison with CFD results, between the 22 and 30 blade rotor, will be discussed and compared extensively.

Similarly, in Figure 18, without using high-speed numerics in the solver, the 22-bladed rotor had a localized peak in thrust-to-power ratio. In contrast, using high-speed numerics, the same kind of peak held for the 20-bladed rotor. Below 16 blades, the thrust to power ratio increased because the required power decreased faster than the produced thrust. In reference [6], the CFD model of a propulsive wing incorporated 18 blades. Also from Tables 4 and 5, it is noticed that by lowering the number of blades, the pressure ratio, the required power and the thrust are reduced, as expected.

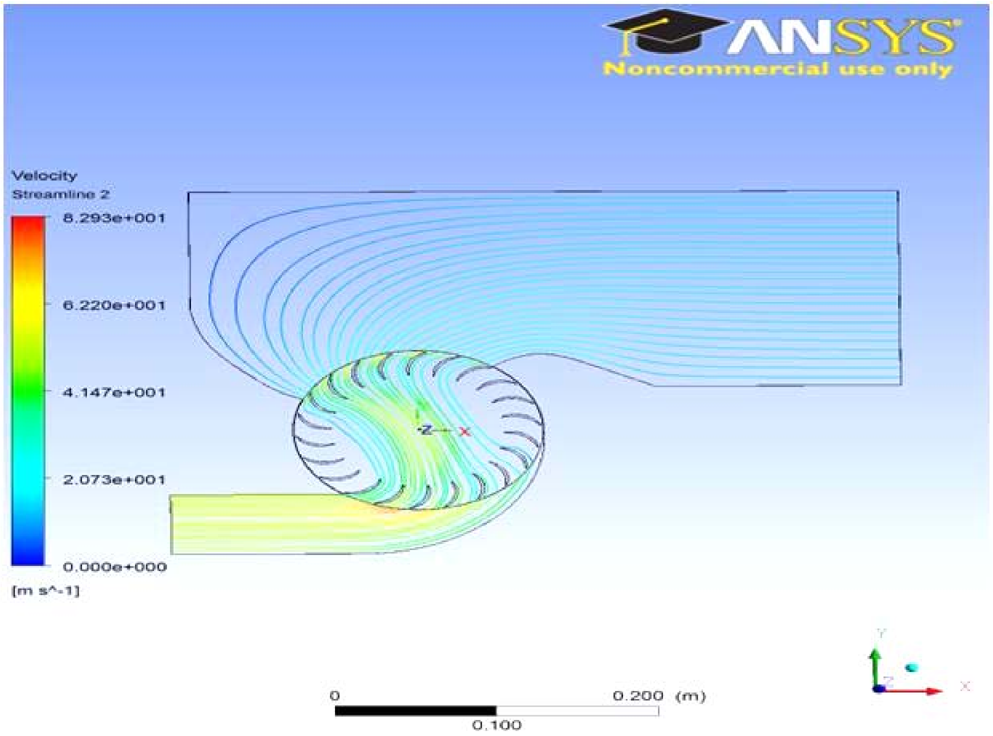

Figure 15. Streamline Pattern for Configuration 3 With 22-Bladed Rotor, Open Throttle 4,000 rpm

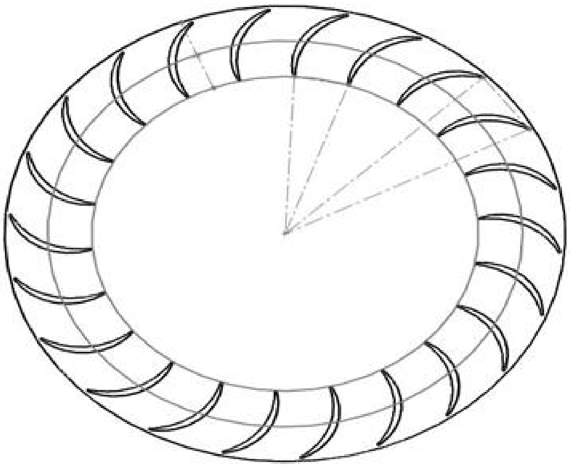

Figure 16. Drawing of 22-Bladed Rotor in SOLIDWORKS

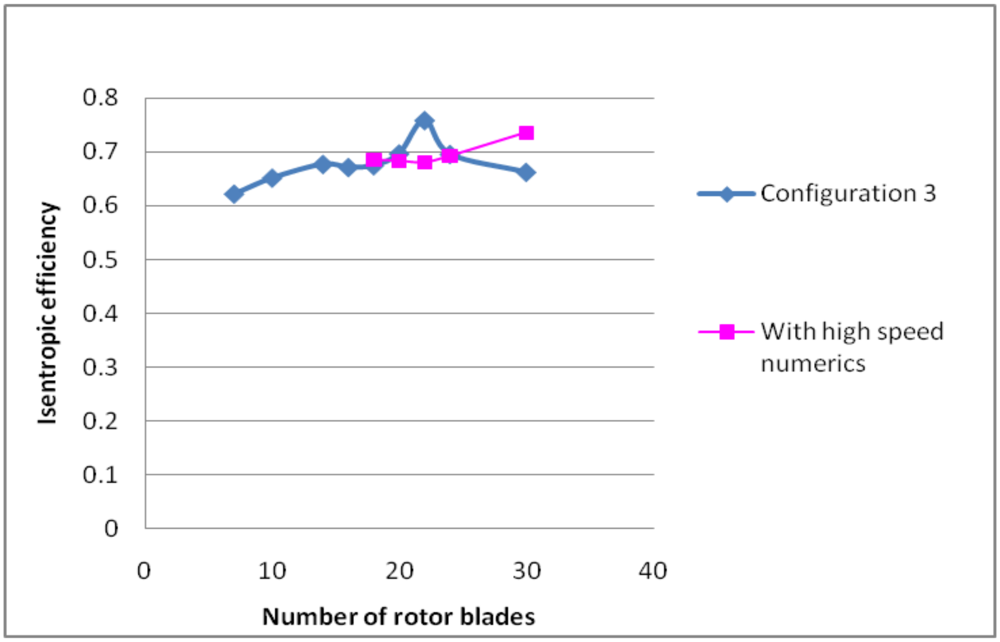

Figure 17. CFD Results for Isentropic Efficiency vs. Number of Rotor Blades, Tables 4 and 5

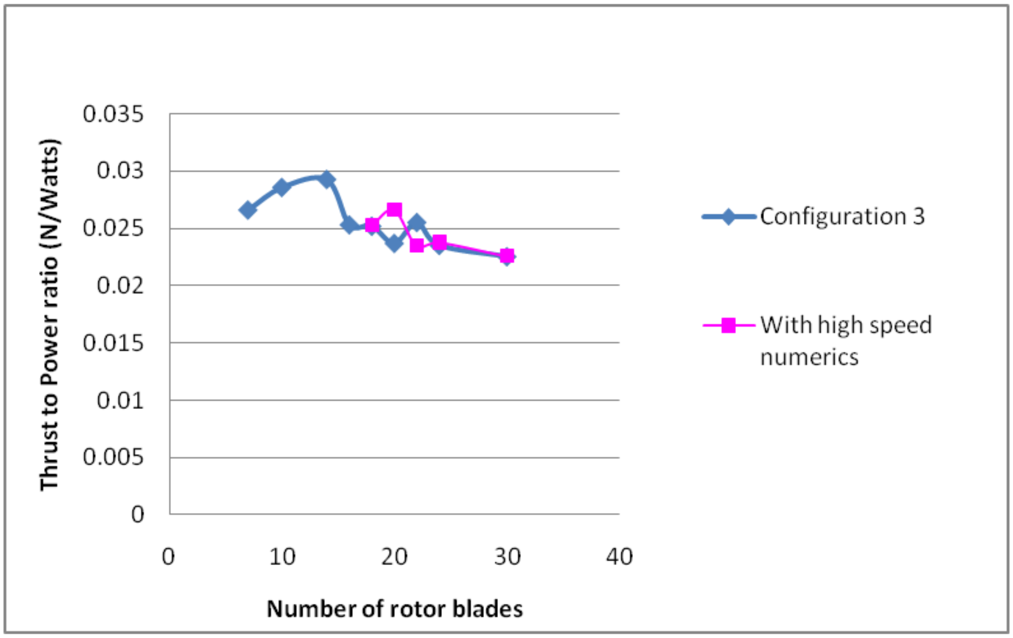

Figure 18. Numerical CFD Results for Thrust-to-Power Ratio vs. Number of Rotor Blades, Tables 4 and 5

3. CFD Throttle Simulation

An attempt was made to simulate the throttle condition at the exit of the CFF. In order to mimic the load at the exit, a nozzle was added at the outlet duct to reduce the mass flow rate. This is physically realistic, as a nozzle would be a likely control method on a flight vehicle. Figure 19 shows the load condition with Configuration 3. The ratio of the exit area to the open-throttle exit area is 50%, which correspond roughly to 50% load. The total number of mesh elements that were used on cases of Table 6 was around 51,000 and both selections of high-speed numerics were used (on and off). It was found that, using a very fine mesh (82,000 elements) produced numerical errors regarding efficiency in all cases. In that fine mesh case, the result was an isentropic efficiency higher than 1, which is physically impossible. From Table 6, comparing the different cases, it is concluded that using fewer blades reduced the mass flow, pressure ratio, thrust and power. The same did not happen for the thrust-to-power ratio. The 22- and 18-bladed rotors had higher thrust-to-power ratios compared with the 30-bladed rotor. This fact, in conjunction with a lower pressure ratio with fewer blades, produced the “CFD” conclusion that the 30-bladed rotor can be used in situations where more thrust and higher pressure ratio are needed, regardless of efficiency, e.g., hovering in a propulsive wing. However, the 22-bladed rotor would be more suitable for transit flight conditions, where minimizing fuel consumption is important. Also, regarding the slight increase in specific thrust of the 22-bladed rotor with load, Table 6 is in accordance with the open-throttle condition investigation without high-speed numerics (Table 4 and Figure 18).

At this point, the concept of two CFFs embedded in a propulsive wing near the trailing edge with a common exhaust duct can be envisioned. One of them can be selected with 30 blades and the other with 22 blades for cruise speed. With that design, when additional power is needed (e.g., for hovering, a sudden increase of speed, or fast maneuvering), the additional 30-bladed rotor can be turned on. Again, like the open-throttle condition below a 16-bladed rotor, the required power is reduced more rapidly than the produced thrust, something that increases the specific thrust. However, using fewer blades, the produced thrust and pressure ratio are too low to support real airborne applications, at least for only one rotor CFF embedded in a wing and with the volume constraints in mind.

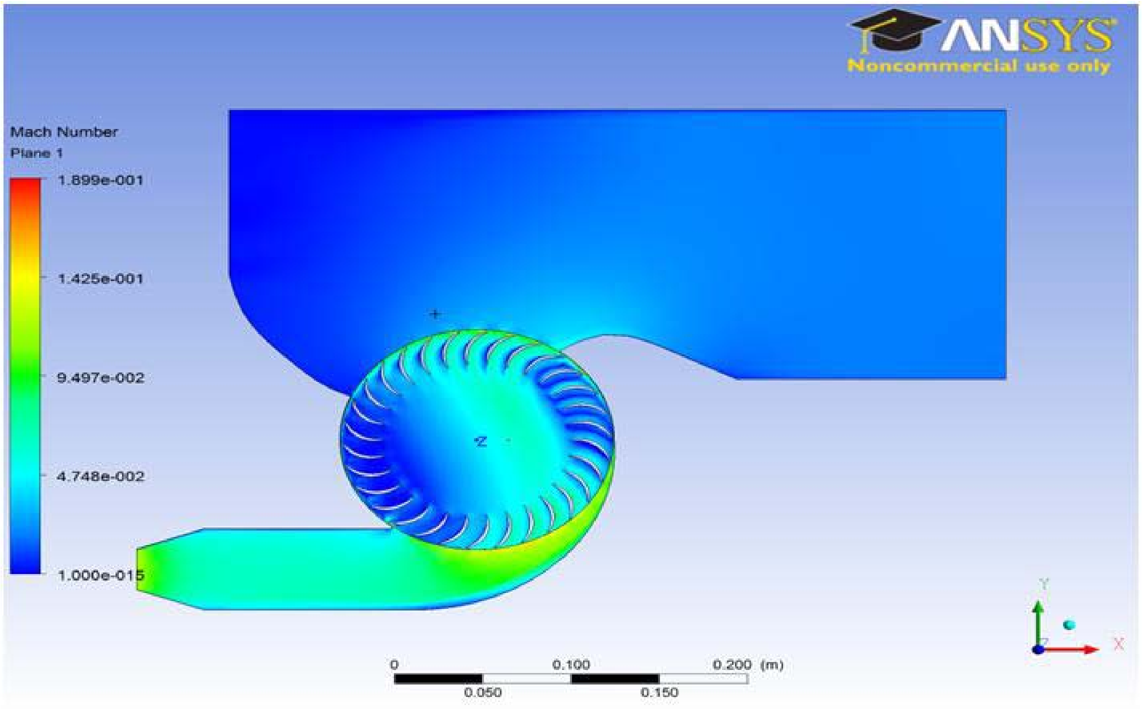

Figure 19. Mach Number Contours for Configuration 3 With 50% Load and 30-Bladed Rotor at 4,000 rpm

Table 6. CFD Comparison Results for Various Bladed Rotors CFF With Load, With and Without High-Speed Numerics Used in the Solver

Configuration 3 CFF Horizontal inlet with Cavities Blanked Off and Load, Figure 19	mdot/L ((kg/sec)/m)	Pressure Ratio	Isentropic Efficiency	Thrust per unit length (N/m)	Power per unit length (W/m)	Thrust/ Power (N/W)
Without High Speed Numerics Used in the Solver						
4,000 rpm, **30** blades	1.39307	1.0102	0.8092	55.9067	1994.33	0.02803
4,000 rpm, **24** blades	1.34670	1.0095	0.85386	52.324	1850.078	0.02828
4,000 rpm, **22** blades	1.3681	1.0098	0.8574	53.966	1862.04	0.02898
4,000 rpm, **20** blades	1.24611	1.0081	0.8805	44.7737	1844.40	0.02427
4,000 rpm, **18** blades	1.21807	1.0077	0.9346	42.8094	1461.41	0.02929
4,000 rpm, **16** blades	1.17959	1.0073	0.97942	40.1247	1266.77	0.031674
Configuration 3 CFF Horizontal inlet with Cavities Blanked Off and Load, Figure 19	mdot/L ((kg/sec)/m)	Pressure Ratio	Isentropic Efficiency	Thrust per unit length (N/m)	Power per unit length (W/m)	Thrust/ Power (N/W)
With High Speed Numerics Used in the Solver						
4,000 rpm, **30** blades	1.4049	1.0101	0.8849	56.024	2008.18	0.02789
4,000 rpm, **22** blades	1.3525	1.0093	0.8584	51.824	1734.80	0.02987
4,000 rpm, **18** blades	1.2273	1.0077	0.9246	42.850	1402.83	0.03054

4. Blade Thickness Investigation

An insight into changing CFF blade geometry was attempted. Initially, Configuration 1 was selected for modeling, which has vertical inlet with cavities. Figure 20 shows the thin blade in a MATLAB plot and its four regions (pressure side, suction side, inner blade tip edge, outer blade tip edge) (Appendix B).

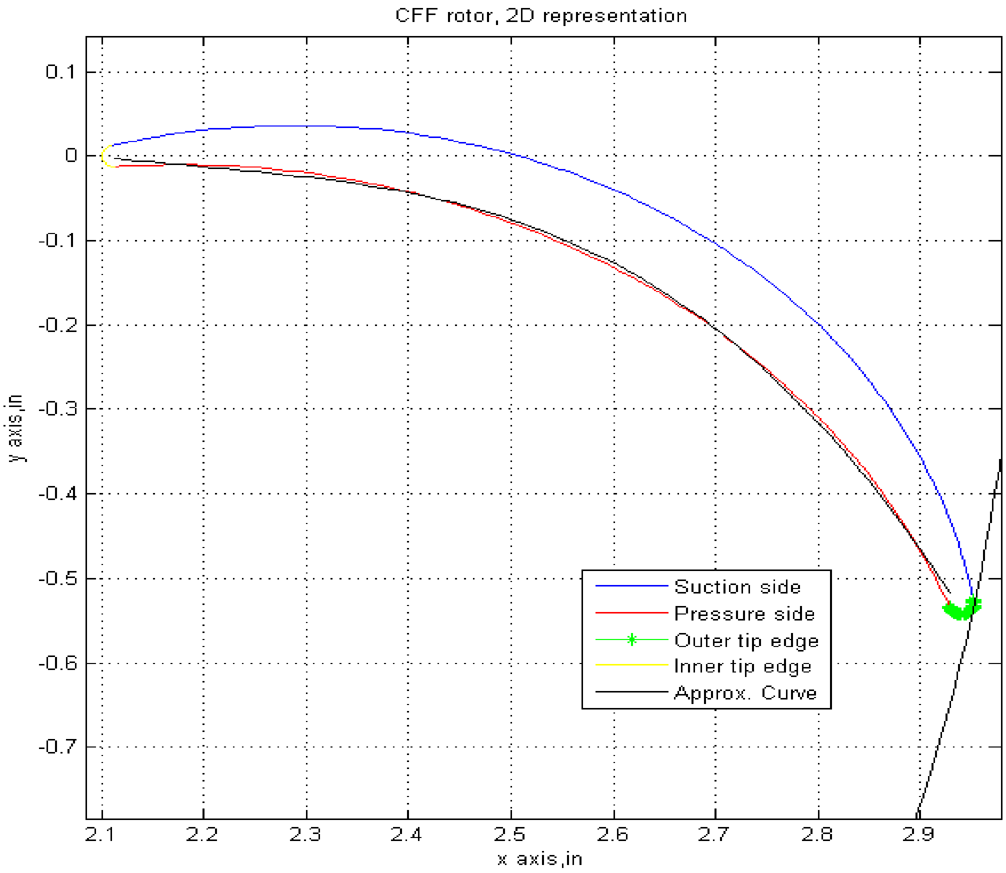

Figure 20. Thin Airfoil in MATLAB and Approximating Curve for Pressure Side

The graphical representation of the double circular arc blade in MATLAB was made using existing pair points (x, y) in Cartesian coordinates. In an effort to change the blade thickness and do parametric studies, an analytical form of the blade geometry was necessary, y = y(x). This was made using the least square technique as can be demonstrated in Figure 20 and Appendix B. An expression for both suction and pressure surfaces can be found so, for a fixed value of x, the exact vertical distance d = $|y1-y2|$ is known, where y1(x) is suction curve and y2(x) the pressure curve.

Now, since the distance d for a spatial distribution x is known, the suction curve y1 can be modified by changing the present thickness d. For example, if a 40% increase in thickness is desired, the new value for d will be 1.4*d, and so $|y1new-y2|=1.4*$d. In Figure 21, an increase in airfoil thickness by 40% can be seen. Because an accurate approximation of the two curves (pressure side, suction side) near the edges was not possible with the least square technique, a smaller broadband of the chord length x was used for the double circular arc blade geometry (Appendix B).

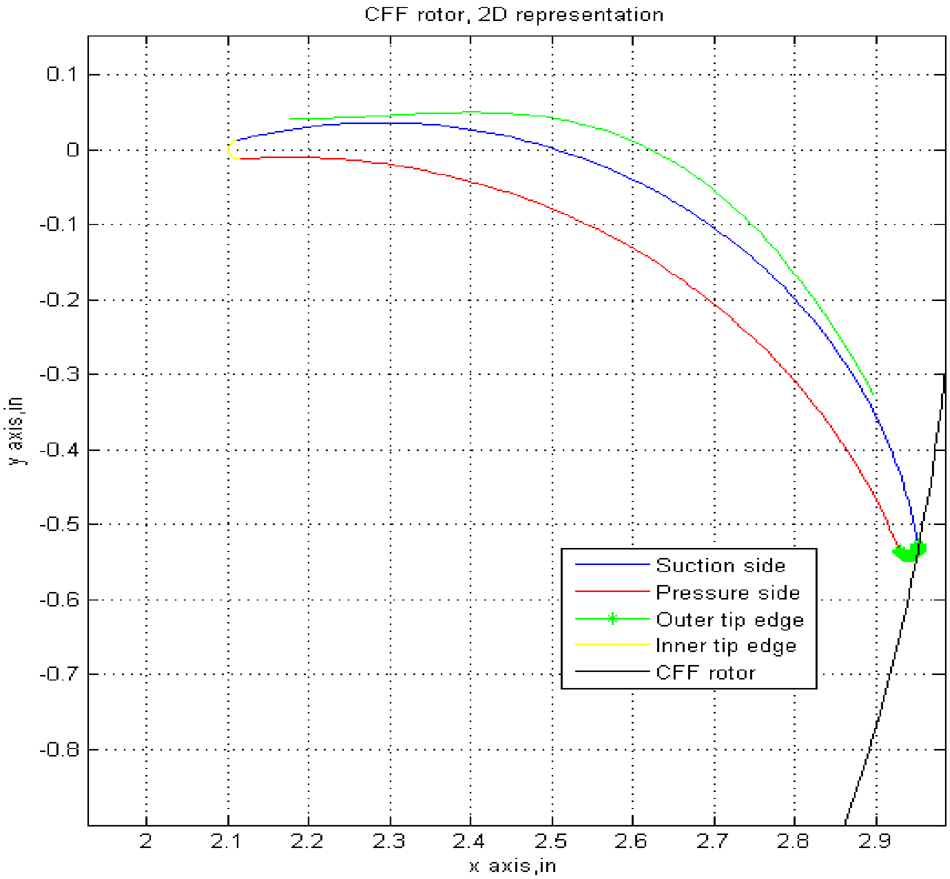

Figure 21. Airfoil Thickness Increased by 40%

The points generated in MATLAB for the thicker blade were designed in SOLIDWORKS individually and then connected together with splines. The rest of the points were estimated and a smoothing curve tool was used. A weakness of SOLIDWORKS is that one cannot use the extrude cut feature for a curve that has been created on a plane, using the curve tool with data (x, y, z) points. Thus, the strategy of manually inserting all the points was the only option for designing the thicker blade rotor disk.

Table 7. Comparison Table Between the Normal Rotor With the Increase in Blade Thickness by 40% at the Same Speed, 3,000 rpm, and Same Configuration.

Configuration 1 CFF Vertical inlet with Cavities	mdot/L ((kg/sec)/m)	Pressure Ratio	Temp. Ratio	Isent. Efficieny	Thrust per unit length (N/m)	Power per unit length (W/m)	Thrust/ Power (N/W)
Baseline airfoil blade profile	3.050393	1.0119	1.00516	0.65398	138.655	5094.91	0.0272144
40 % increase blade thickness	3.035401	1.0119	1.0054	0.62731	137.313	5257.95	0.0261152

From Table 7, a slight deterioration in performance for the thicker blade rotor at 3,000 rpm was noticed. The required power increased as the thickness increases and the resultant thrust was reduced. This makes the thrust-to-power ratio smaller compared with the normal rotor blade thickness. Also, there was a relative decrease in efficiency around 4%, when the high-speed numerics option was not used in the solver. It was believed that the thicker blade rotor could be used to alleviate the higher speed losses induced at transonic speeds. However, a CFD simulation for this case showed inconclusive results. For the open-throttle condition and baseline configuration at 8,000 rpm, the maximum Mach number remained at the same level for the thicker blade rotor disk with a slight relative increase by 3%, absolute value M max = 0.5363. All other characteristics remained at the same level analogous to the 3,000 rpm case (Table 7).

III. EXPERIMENTAL SETUP

A. DESCRIPTION OF EXPERIMENTAL APPARATUS

1. Turbine Test Rig (TTR)

The Cross-Flow Fan Test Assembly (CFTA) was powered by the existing Turbine Test Rig (TTR) at the Turbopropulsion Laboratory at the Naval Postgraduate School. The turbine of the TTR was driven by a compressed air supply system from an Allis-Chalmers 12-stage axial compressor. This compressor was capable of producing 10,000 cubic feet (283.17 m^3) of air per minute (4.72 m^3/s) at 30 pounds per square inch gauge (psig) (206.84 kPa-g). The compressor was powered by a 1,250 horsepower electric motor. The compressed air was cooled through a water heat exchanger above ambient temperature prior to supplying the TTR. A pressurized oil mist system provided lubrication for both TTR and the CFTA shaft bearing (Figure 22). Additionally, a data acquisition system on the TTR provided a control station with bearing temperature, vibration monitoring and shaft speed from a one-per-revolution measurement system.

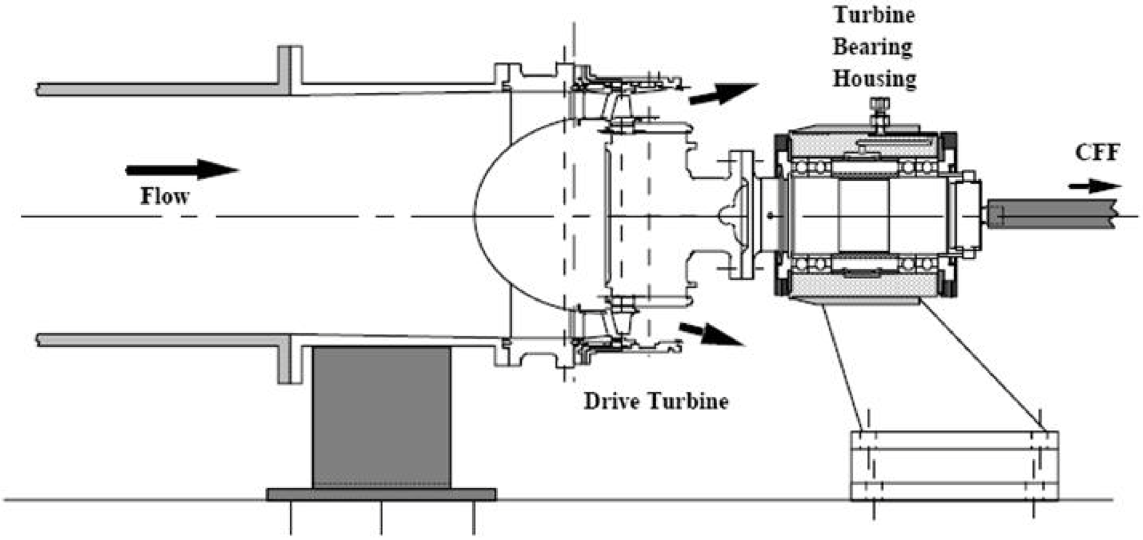

Figure 22. Schematic Representation of Turbine Test Rig (TTR). From [9]

2. Cross-Flow Fan Test Assembly (CFTA)

The CFTA was similar to other CFTAs used at the NPS TPL for previous CFF tests [8]–[14] and was derived from the VSD assembly #6. This assembly consisted of a rotor of double circular arc blades; in addition to the 30-bladed case, a 22-bladed rotor was investigated also. The rotor's diameter was 152.4 mm (6 inches) and the span length was 38.1 mm (1.5 inches), similar to that used by Cordero [13]. The 105° inlet arc, 130° exit arc and the positions of the high-pressure cavity (HPC) and the low-pressure cavity (LPC) remained the same. The inlet bellmouth for measuring the flow rate with a 82.6 mm (3.25 inches) diameter, used by Cordero [13], was unchanged. An exhaust duct with a butterfly valve was connected to the exit of the fan housing for throttling studies. In this experiment, only the horizontal inlet configuration was investigated, as shown in Figure 23.

Figure 23. Front of CFTA with Horizontal Inlet Configuration

A new rotor, inspired by CFD results was developed. A total of 22 new aluminum blades were assembled between the two concentric supporting disks. Each blade was connected with two pins on each side of the rotor disk. Between those pins and the assembly holes, epoxy glue was used to attach the blades to the hub and shroud. Figure 24 shows the 22-bladed rotor. The existing blanking plate was modified to accommodate the new rotor for this experiment. The IGVs previously tested by Cordero [13] were removed from the blanking plate.

All other components remained unchanged from the horizontal inlet configuration used in previous testing by Cordero [13] and Gannon [14]. Also, for blanking off the cavities (HPC and LPC), Teflon-made cover parts were used (Figure 24).

Figure 24. The 22-Bladed Rotor Assembly in the CFF Housing, Blanked Off Cavities

B. CONTROL AND INSTRUMENTATION

1. Control

Control of the TTR was executed by a remote station next to a window looking into the test cell. The control station was used to set the rotational speed of the CFF by adjusting the airflow from the plenum chamber into the TTR (Figure 25). Shaft speed was monitored by a one-per-revolution signal from the TTR. Throttling of the CFTA was accomplished by a manually controlled butterfly valve.

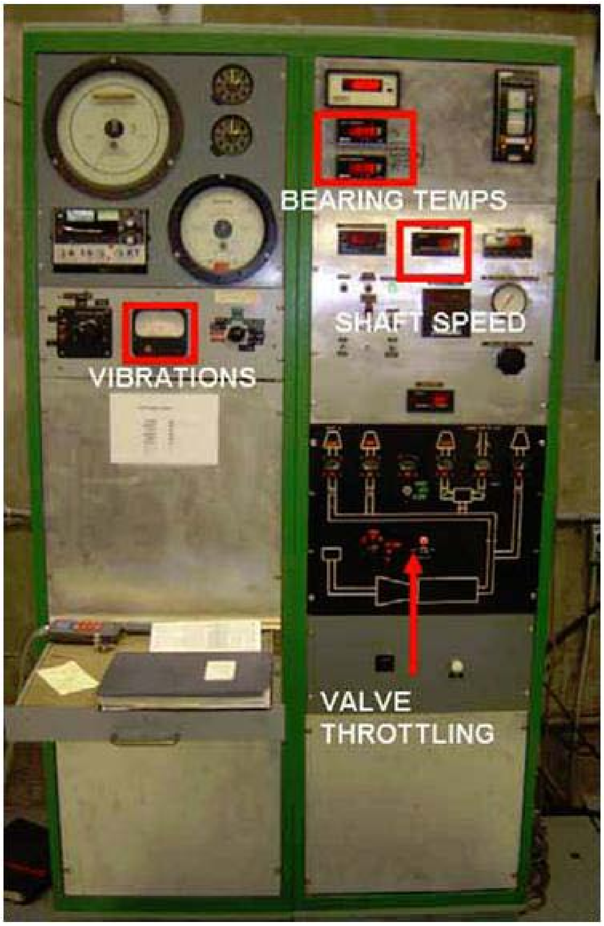

Figure 25. Turbine Test Rig (TTR) Remote Control Station. From [10]

2. Instrumentation

For this experimental investigation, similar instrumentation to that used by Cordero [13] and previous researchers at the Naval Postgraduate School [8]–[12], [14] was used. The flow field properties were measured using United Sensor Devices model USD-C-161 1/8 inch (3 mm) combination thermocouple/pressure probes and static pressure taps. Air tubes from pressure probes were connected to an 8-channel, 17,237 Pa (2.5 psig), Scanivalve digital sensing array (DSA). The purpose of the DSA was to convert mechanical pressure signals into analog electronic signals and then to digital signals.

Similarly, the thermocouple sensors were routed to a multiplexer and were recorded by the HP E1326B Multimeter Adapter within VXI mainframe. This mainframe was connected to a Pentium-based personal computer. For determination of the mass flow rate, three pressure taps were used in the inlet bellmouth. Combination probes at locations 10, 12, and 2 o'clock relative to the axis of rotation of the CFF recorded inlet stagnation pressures and temperatures. Shaft speed was measured with a counter totalizer, which converted electric pulses from a one-per-revolution sensor on the TTR into a readout of shaft speed. The multiplexer channel location and data label for thermocouples is shown in Table 8. The Scanivalve port, location, data label and measurement type for the pressure measurements are shown in Table 9. In Figure 26, a schematic of probe locations and pressure taps with horizontal inlet is presented.

Table 8. Temperature Measurements

Multiplexer Channel	**Probe**	**Nomenclature**
13	A	Tt_A
14	B	Tt_B
15	C	Tt_C
8	10 o'clock	Tt_10
9	12 o'clock	Tt_12
6	2 o'clock	Tt_2

Table 9. Pressure Measurements. After [13]

Port Number	**Probe**	**Nomenclature**	**Type**
9	A	Pt_A	Total Pressure
8	B	Pt_B	Total Pressure
6	C	Pt_C	Total Pressure
3	10 o’clock	Pt_10	Total Pressure
4	12 o’clock	Pt_12	Total Pressure
5	2 o’clock	Pt_2	Total Pressure
2		Ps_in	Static Pressure
7		Ps_out	Static Pressure
1		P_cell	Static Pressure

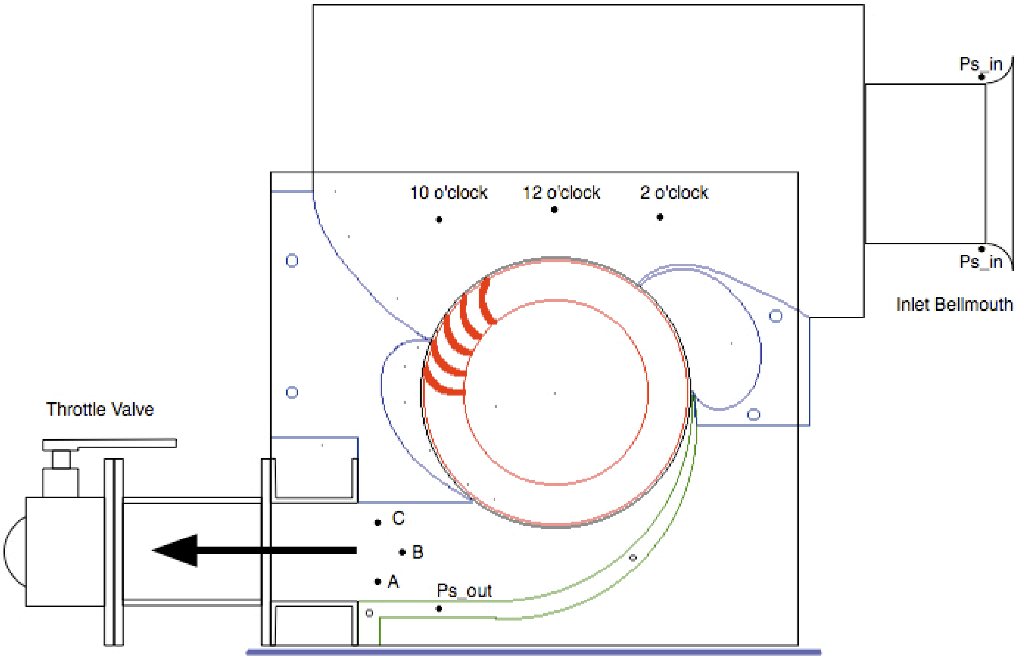

Figure 26. Location of Combo Probes and Static Pressure Taps for Experimental Setup, Horizontal Inlet

C. DATA ACQUISITION

1. Acquisition

Digital signals from pressure, temperature and rotation speed measurements were acquired using the software program, Agilent VEE, a Windows-based data acquisition program. The graphical user interface (GUI) developed by Ulvin [12] was similar to that used by Cordero [13]. All data were written to a text file (*.txt), which Microsoft Excel could read, for further processing. The three modifications in the GUI by Cordero remained the same and they will be stated again at this point for consistency reasons. The first one has to do with the elimination of mechanical averaging of the 10, 12, and 2 o'clock total pressure probes. Total pressure probes on those locations were recorded individually in the acquisition software and compared with mechanical averaging. The other two modifications take into account the change in the smaller bellmouth (3.25-inch vs. 6.25-inch diameter, 8.25 cm and 15.88 cm, respectively) and 1.5-inch (3.81 cm) span length of CFF.

2. Data Reduction

Properties of the flow field and performance of the CFF were mass averaged and calculated with a non-dimensional velocity X, using the following formulations from [13]. This method has the advantage of working at both low and high speeds:

$$X_i = \frac{v_i}{v_{i,t}} \quad \text{where} \quad v_{t,i} = \sqrt{2C_p T_{t,i}} \quad \text{and} \quad X_i^2 = \frac{\frac{\gamma-1}{2}M^2}{1+\frac{\gamma-1}{2}M^2} \tag{11}$$

X is defined as a fraction referred to as the stagnation velocity. Where C_p is the specific heat of air at constant pressure, γ is the ratio of specific heats and M is the Mach number. Equation (11), after substituting into formulas from [13], yielded the following relationships for temperature, pressure, and density in compressible flow:

$$\frac{T_i}{T_{t,i}} = 1 - X_i^2 \tag{12}$$

$$\frac{P_i}{P_{t,i}} = \left(1 - X_i^{\,2}\right)^{\frac{\gamma}{\gamma-1}} \tag{13}$$

$$\frac{\rho_i}{\rho_{t,i}} = \left(1 - X_i^{\,2}\right)^{\frac{1}{\gamma-1}} \tag{14}$$

Manipulating the above relationships gives:

$$v_i = X_i\sqrt{2C_pT_{t,i}} = \sqrt{1 - \left(\frac{P_i}{P_{t,i}}\right)^{\frac{\gamma-1}{\gamma}}}\ \sqrt{2C_pT_{t,i}} \tag{15}$$

$$X_i = \sqrt{1 - \left(\frac{P}{P_{t,i}}\right)^{\frac{\gamma-1}{\gamma}}} \tag{16}$$

$$\rho_i = \frac{P_{t,i}}{RT_{t,i}}\left(1 - X_i^{\,2}\right)^{\frac{1}{1-\gamma}} \tag{17}$$

where the *i* subscript indicates the particular zone where the property is desired, the *t* subscript indicates total or stagnation value, Cp = 1004.4 J/(kg·K), R = 287 $m^2/(s^2 \cdot K)$, and γ = 1.402. The mass flow rate can then be determined by the following:

$$\dot{m}_i = \rho_i v_i A_i \tag{18}$$

Substituting (15), (17) into (18) gives:

$$\dot{m}_i = \frac{P_{t,i}}{RT_{t,i}}\left(1 - X_i^{\,2}\right)^{\frac{1}{1-\gamma}} X_i\sqrt{2C_pT_{t,i}}\,A_i \tag{19}$$

A_i is the area for each region where measurements occur. The bellmouth inlet area is calculated as A_{inlet} = π*D^2/4, where D = 3.25 in (8.26 cm), giving A_{inlet} = 8.2957 in^2 (53.52098 cm^2). At the outlet, the areas were calculated based on the height of each probe in the exit duct and the span of the fan, which is 1.5 inches (3.81 cm). The corresponding zones with their exit duct heights are show in Figure 27. Table 10 shows area calculations.

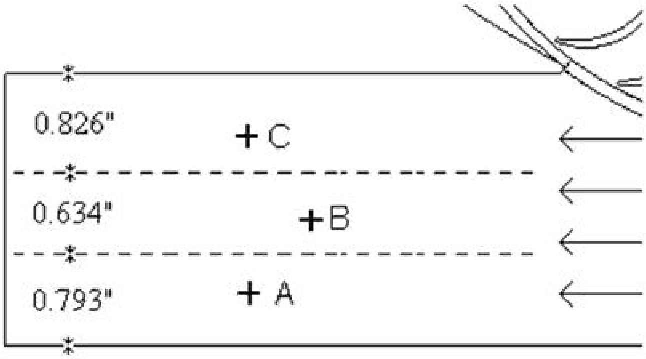

Figure 27. Measured Heights for Zones A, B, and C in the Exit Duct

Table 10. Calculated Exit Duct Areas. After [13]

Zone	Area in^2, (m^2)
A	1.190, (0.0007674)
B	0.951, (0.00061355)
C	1.239, (0.0007995)

Mass averaged total pressure and temperature were then obtained from the following:

$$\overline{P}_{t,out} = \frac{\dot{m}_A P_{t,out,A} + \dot{m}_B P_{t,out,B} + \dot{m}_C P_{t,out,C}}{\sum_{i=A}^{C} \dot{m}_i} \tag{20}$$

$$\overline{T}_{t,out} = \frac{\dot{m}_A T_{t,out,A} + \dot{m}_B T_{t,out,B} + \dot{m}_C T_{t,out,C}}{\sum_{i=A}^{C} \dot{m}_i} \tag{21}$$

Total pressure ratio, total temperature ratio and efficiency were then calculated from the following:

$$\pi = \frac{\overline{P}_{t,out}}{\overline{P}_{t,in}} \tag{22}$$

$$\tau = \frac{\overline{T}_{t,out}}{\overline{T}_{t,in}} \tag{23}$$

$$\eta = \frac{\pi^{\frac{\gamma-1}{\gamma}} - 1}{\tau - 1} \tag{24}$$

Thrust was then calculated from the following relations assuming that u_{in} was zero:

$$F_{thrust} = \dot{m}_{in}\left(u_{out} - u_{in}\right) = \dot{m}_{in}\, u_{out} \tag{25}$$

$$u_{out} = M_{out}\sqrt{\gamma R T_{out}} \tag{26}$$

$$T_{out} = \frac{\overline{T}_{t,out}}{1 + \frac{\gamma-1}{2} M_{out}{}^{2}} \tag{27}$$

$$M_{out} = \sqrt{\frac{2}{\gamma-1}\left[\left(\frac{\overline{P}_{t,out}}{P_{atm}}\right)^{\frac{\gamma}{\gamma-1}}\right]} \tag{28}$$

The absorbed power by the CFF was found from:

$$Power = \dot{m}_{in}\, C_p\left(\overline{T}_{t,out} - \overline{T}_{t,in}\right) \tag{29}$$

The following parameters δ, θ are the correction factors for standard day conditions:

$$\delta = \frac{P_{t,in}}{P_{t,std}} \tag{30}$$

$$\theta = \frac{T_{t,in}}{T_{t,std}} \tag{31}$$

The corrected values for mass flow rate, efficiency, thrust, and absorbed power for the standard day conditions were given by the following:

$$\dot{m}_{corr} = \dot{m}\frac{\sqrt{\theta}}{\delta} \quad (32) \qquad N_{corr} = \frac{N}{\sqrt{\theta}} \quad (33) \qquad F_{corr} = \frac{F}{\delta} \tag{34}$$

$$P_{corr} = \frac{P}{\delta\sqrt{\theta}} \tag{35}$$

where $P_{t,std}$ is 101,325 Pa and $T_{t,std}$ is 288.1 K from [13].

The equations described above and correction factors were applied in real time in the data acquisition software modified for the inlet bellmouth diameter and span length. Time-averaged values of the data were obtained by recording five or more sets of data at each test point throttle position.

D. TEST PLANS

Testing of the 6D1.5L CFF was performed with the new 22-bladed rotor. Two types of housing configurations have been used, one with the cavities blocked (blanked off) and one with cavities open (Table 11). On both experimental models, the inlet region remained horizontal, when the CFD model was only for blanked-off cavities with the horizontal inlet. For each throttling level, runs were conducted from 3,000 rpm to 8,000 rpm in 1,000 rpm increments.

In addition, an inspection of the plastic tubes transmitting pressure from the probes to the pressure brick (DSA) showed some wear and breaks in the tubes. New lines were installed and a re-inspection for possible leaks was conducted. Also, the proper position and insertion depth of the pressure probes were checked at both the inlet and outlet region of CFF. This is important, as a probe too near the wall will measure the boundary layer pressure and lead to inaccurate results, usually higher measured efficiencies. After those modifications, the experimental investigation of the previous tested 30-bladed rotor by Cordero [13] was again necessary.

Experimental results comparison for the 30-bladed rotor with those from Cordero [13] did not show much deviation. The experiment at each test plan was made in two phases in order to incorporate the rotor change (30- or 22-bladed) with fixed housing configuration (open or closed cavities). The CFTA has the flexibility for an easy change of either rotor or the cavities condition (open or closed). At the exit duct, various throttling conditions were simulated from the butterfly valve position. For the almost-closed throttle case, measurements were taken until stall was approached.

Table 11. Experimental CFF Configurations

Test	Housing Configuration
A	Horizontal Inlet, No Cavities (Blanked Off), 22-Bladed Rotor vs. 30-Bladed Rotor
B	Horizontal Inlet, With Cavities (Open), 22-Bladed Rotor vs. 30-Bladed Rotor

IV. PROPULSIVE WING

A. AIRFOIL SETUP

Attempts have been made to have the CFF rotor embedded in the trailing edge of an airfoil, for numerical evaluation and parametric study. In order to do so, it was first necessary to examine some characteristics of airfoils and define a method for designing them correctly. Reference [17, chapter 6] provides valuable information about the designing of an airfoil, either symmetric (example 00XX) or camber type (example XXXX). In this particular problem, an airfoil of camber type NACA 2415 was initially selected. The first number "2" indicates the percent of maximum camber, the second number "4" indicates the percent of chord length, where the maximum camber happens. The last two numbers indicate the percent of chord thickness. This is a simple airfoil and it has a real application in Cessna-type airplanes. Appendix C contains the MATLAB code that generates the geometry of the desired airfoil, given chord length, camber and thickness as input (Figure 28).

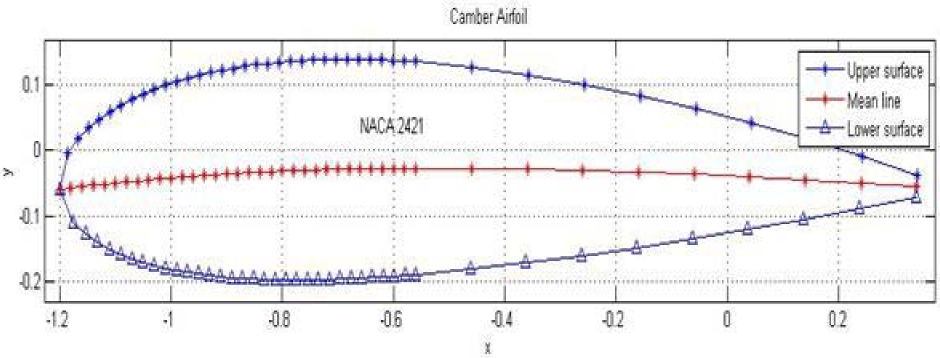

Figure 28. Camber Wing, Typical Airfoil Representation From MATLAB, NACA 2421, Chord Length 1.6m

The airfoil NACA 2415, which was initially selected, was taken to have chord length c = 2.28 m, Figure 29. The next step was to model this airfoil and use it in CFD, trying to predict, as accurately as possible, the lift and the drag. A very thin 3-D solid model was designed in SOLIDWORKS. The thickness of the airfoil was kept small (1.5875 mm) compared to the other dimensions in an effort to approximate the flow as

2-D in a CFD environment, like the CFF model. The thickness was chosen to be the same as the CFF rotor, in order to have matching dimensions between the airfoil and CFF rotor, when assembling them together in the propulsive wing concept. Also, shown in Figure 30 is the bounding box around the airfoil, with much larger size dimensions compared with the airfoil. This drawing was imported using the CFX-mesh tool and then the generated grid at ANSYS-CFX Pre in order to set the problem's parameters.

Figure 29. SOLIDWORKS Representation of NACA 2415 With Boundary Conditions Plane

The number of elements that have been used is sufficient to give satisfactory results regarding the lift and, if possible, the drag. This is very important since the same number of elements were used for further modeling, either for airfoils containing an embedded CFF. The free stream velocity was selected to be 35 meters per second (m/s), or 79 miles per hour (mph), with an angle of attack (AOA) = 8^{o}. The velocity components were u = 34.65938 m/s and υ = 4.8710 m/s, respectively. As inlet boundary conditions for the model are the left and bottom edge of the rectangle box with u, υ velocity input components at the faces. The other two edges are treated as free openings (Figure 31). Also, like the CFF model, the total energy method was selected in ANSYS-CFX Pre.

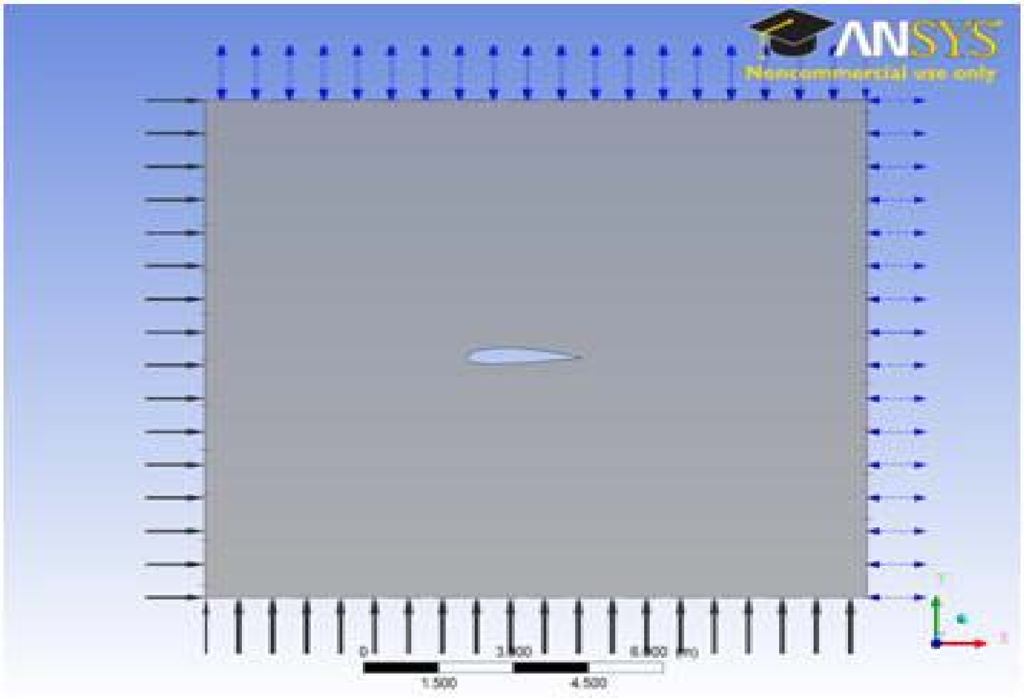

Figure 30. Boundary Conditions Specification with CFX-Pre of the NACA 2415 Airfoil

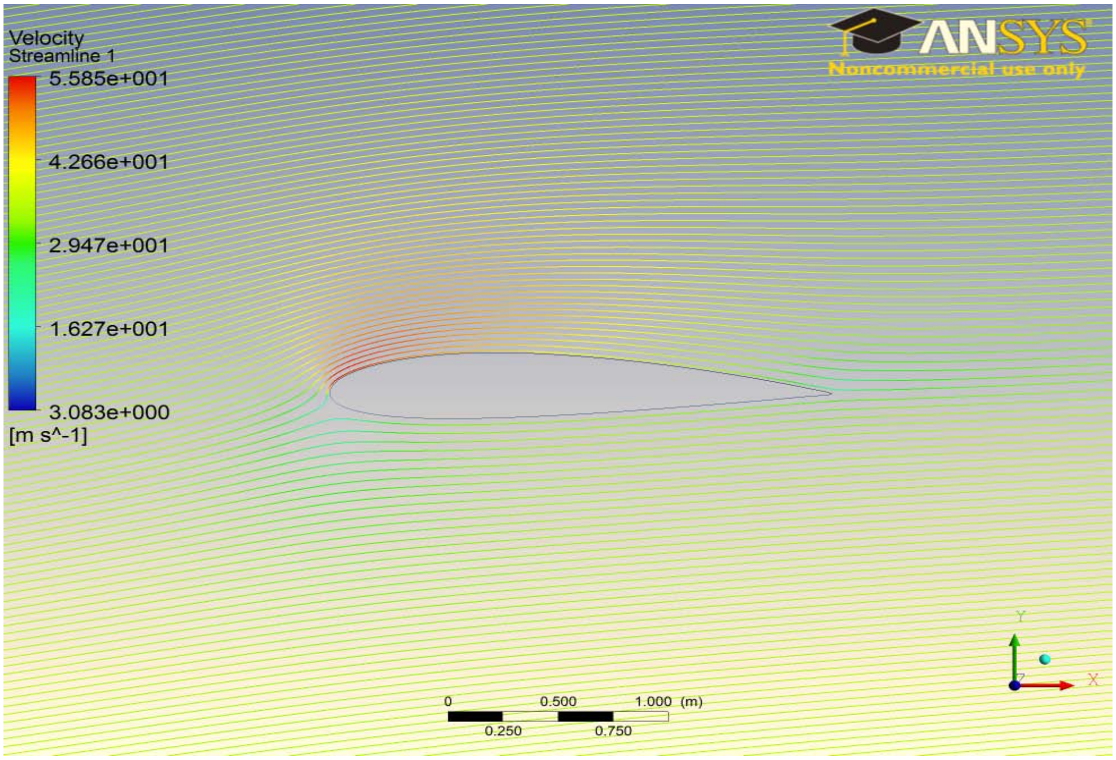

Figure 31. Streamlines for NACA 2415 at AOA 8^o, c = 2.28m, U =3 5 m/s

The following formulas were used from White [18] regarding the lift and drag coefficient:

$$L = \frac{1}{2}\rho \cdot V^2 \cdot A_p \cdot C_L \tag{9}$$

$$D = \frac{1}{2}\rho \cdot V^2 \cdot A_p \cdot C_D \tag{10}$$

Where A_p is the platform area, $A_p = \int cdb$. In our example calculations, we assume that $A_p = c*b$, where c is the chord length and b is the span length of the airfoil, for NACA 2415, c = 2.28 m and b = 1.5875 mm, respectively. The number of elements that have been used in meshing the model was 305,148, in an extruded 2-D mesh, and the analysis was steady-state. The result for the NACA 2415 c = 2.28 m was $C_{L\ ,CFD} = 0.997$, where from Abbot and Von Doenhoff [17] experimental $C_L = 1$. In the above calculations, an average air density of 1.2032 kg/m^3 was selected. The lift was calculated from an ANSYS built-in function, calculating the force around the airfoil walls (viscous walls). Although the lift coefficient was predicted quite accurately, that was not the case for the drag coefficient. The drag was over-predicted and there is no match with the experimental value from [17]. In fact, for the NACA 2415 at 8^o AOA, $C_{D,\ CFD} = 0.0845$ was found. The experimental result with Re = $5.089*10^6$ is $C_{D,exper.} = 0.009$, so the difference is quite high, almost ten orders of magnitude higher, but the absolute difference remained small. Although further simulations were made, with finer grids and residual to the order of 10^{-8} for the solver target, the improvement of the drag was not significant. This conclusion that the CFD software is unable to accurately predict the drag of a simple airfoil is not new. Many other researchers have unsuccessfully tried in the past to do the same (CFD online source). However, there exist some model techniques, like the transition turbulence model in ANSYS CFX, which improve the drag calculations. The author's opinion is that with CFD it is difficult to accurately capture the physics of the problem and exactly define the thin boundary layer around a viscous body. On that point, it is worth noting this as another reason that one should not merely rely on CFD results. Experimental verification with wind tunnel tests is still necessary.

Because it is highly desirable to have the CFF fan embedded in the trailing edge of the airfoil, except in the steady-state solution for the simple airfoil, a transient solution for the same airfoil was conducted. This was done to verify that the transient-type problems will give similar or close results to the steady state regarding the lift and the drag since the CFF is inherently a transient-type problem. The result was that the transient analysis converged to steady-state, something that was encouraging for further simulation of the embedded CFF airfoil. Also, the drag coefficient was improved compared with the experimental value (Table 12).

Table 12. NACA 2415 Lift and Drag Coefficient Results for CFD and Experimental Data

Airfoil NACA2415 ,c = 2.28, density $\rho = 1.2032$ kg/m^3	Solution type	$C_{L,\ CFD}$/ Lift (N) $C_{L,\ exper.} = 1$	$C_{D,\ CFD}$ / Drag (N) $C_{D,\ exper.} = 0.009$
AOA 8^0, free stream velocity 35m/s	Steady-state	0.997/2.6595 (N)	0.0845 /0.2254 (N)
	Transient	0.909/2.4261 (N)	0.04326/0.05061 (N)

In Figure 32 (a) is the streamlines pattern for the transient solution whereas on Figure 32 (b), a stall condition is depicted with the same free stream velocity, but with AOA 30^0. This stall condition predicted on the airfoil was both for transient and steady state flow. In the transient kind of problem of Table 12, the method of fixed time steps was used in ANSYS CFX-Pre.

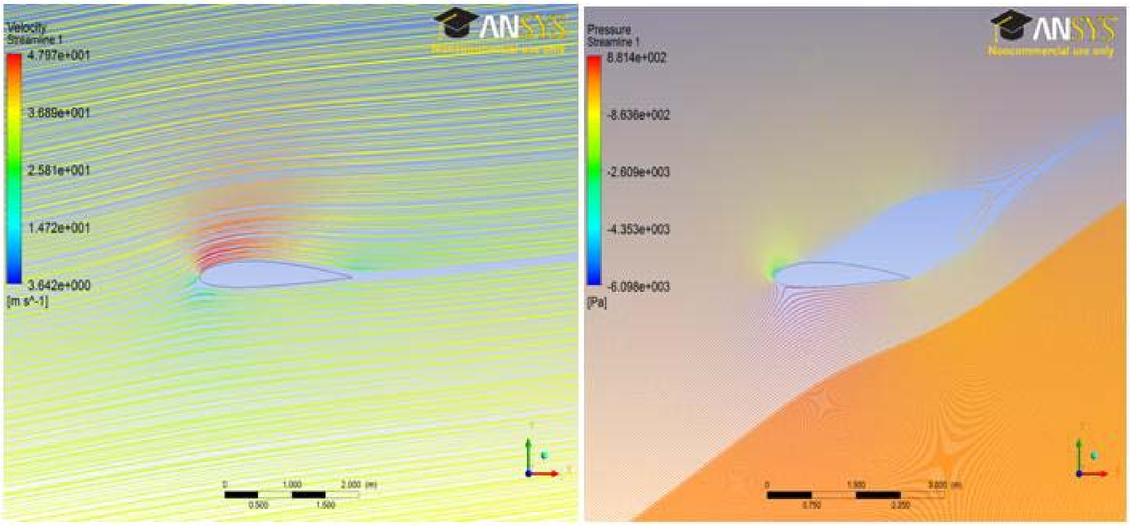

(a) (b)

Figure 32. NACA 2415, (a) Transient Streamlines at AOA 8^o, c = 2.28m, U = 35 m/s, (b) 30^0 AOA Stall Condition Modeling, CFX-Post

B. CFD CALCULATIONS

With those calculations considered and the experience from simple airfoils, a first attempt was made to have the CFF rotor embedded near the trailing edge of an airfoil. A solid model was built in SOLIDWORKS and the first one was the NACA 2415 with CFF rotor and c = 2.28 m. The calculations at two different AOA are in Table 13. Because the length of the airfoil was quite high for the 6-inch rotor, a chord length of c = 1.6 m was then selected. In addition to keep the center of the CFF rotor around 70% chord length from the leading edge, and because the NACA 2415 was not appropriate for that, a “fatter” wing, like NACA 2421, was selected for the next design (Figures 33, 34).

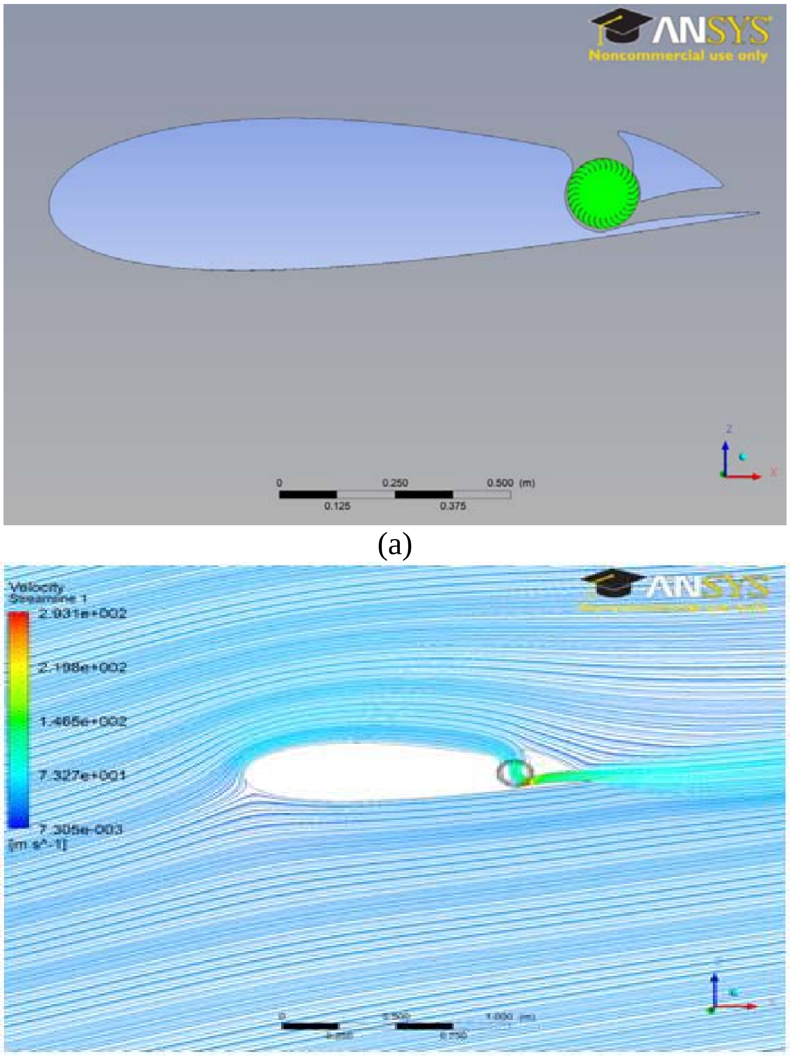

Figure 33. Fully Embedded CFF in a NACA 2421 Airfoil, (a) CFX-Pre Representation, 30 Blades, (b) CFX-Post AOA 15^0, Streamlines, 30 Blades CFF

Table 13. Lift and Thrust Force for Different Types of CFF Embedded Airfoils and AOA

Airfoil type:	Operation speed CFF	Location	Lift force (N)	Thrust force (N)
NACA2415 c = 2.28m AOA = 8^0 U = 35 (m/s) CFF:30 blades	3,000 rpm	Viscous Walls	3.62018	-0.297076
		Blades	-0.1783	0.0154134
		Sum	3.44435	-0.2816626
	8,000 rpm	Viscous Walls	3.51716	-0.34443
		Blades	-0.941273	-0.138146
		Sum	2.57588	-0.482576
	12,000 rpm	Viscous Walls	5.46404	-0.46616
		Blades	-1.53928	-0.34629
		Sum	3.92476/C_L = 1.491	-0.81245
NACA2421 c = 1.6m AOA = 8^0 U = 35 (m/s) CFF:30 blades	3,000 rpm	Viscous Walls	2.32269	-0.207591
		Blades	-0.150156	0.130664
		Sum	2.172534	-0.076927
	8,000 rpm	Viscous Walls	2.67292	-0.837339
		Blades	-0.869949	0.32707
		Sum	1.802971	-0.510269
	12,000 rpm	Viscous Walls	3.61365	-1.52734
		Blades	-1.57996	0.409203
		Sum	2.03369/ C_L = 1.10	-1.118137
Simple NACA2421 airfoil, without emb. CFF, AOA = 8^0, U = 35(m/s)		Viscous Walls	1.8128/ C_L = 0.96	-0.111718
NACA2421 c = 1.6m AOA = 15^0 U = 35 (m/s) CFF:30 blades Figure 33	12,000 rpm	Viscous Walls	5.22734	-1.78402
		Blades	-1.57298	0.387104
		Sum	3.65436/C_L = 1.9522	-1.3969

Simple NACA2421 airfoil, without emb. CFF, AOA = 15^0, U = 35 (m/s)		Viscous Walls	$2.65517/C_L = 1.41845$	-0.42016
Airfoil type:	Operation speed CFF	Location	Lift force (N)	Thrust force (N)
NACA2421 c = 1.6m AOA = 15^0 U = 35 (m/s) CFF:20 blades Figure 35	12,000 rpm Fully embedded CFF	Viscous Walls	5.41829	-2.26376
		Blades	-0.672718	0.599555
		Sum	$4.745512/C_L = 2.535$	-1.66421
NACA2421 c = 1.6m AOA = 15^0 U = 35 (m/s) CFF:20 blades Figure 36	12,000 rpm Partially embedded CFF	Viscous Walls	4.35816	-2.7208
		Blades	0.356951	1.69263
		Sum	$4.71511/C_L = 2.5189$	-1.02817
NACA2421 c = 1.6m AOA = 30^0 U = 35 (m/s) CFF:22 blades Figure 38	12,000 rpm Fully embedded CFF	Viscous Walls	7.94215	-2.70678
		Blades	-0.770399	0.236868
		Sum	$7.171751/C_L = 3.83$	-2.470

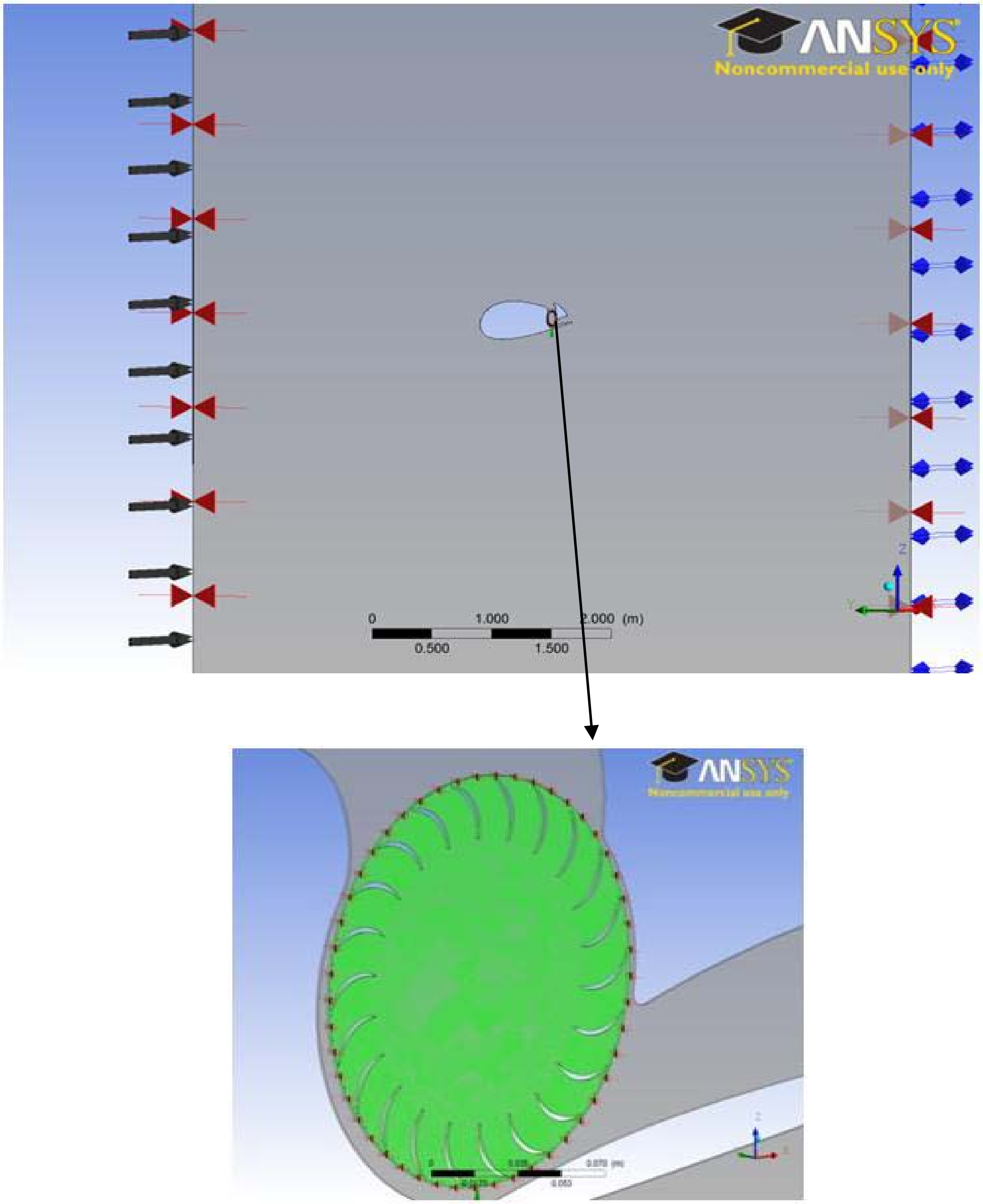

Figure 34. Embedded CFF in a NACA 2421 Airfoil with 22-Bladed Rotor in ANSYS CFX-Pre, 3-D view

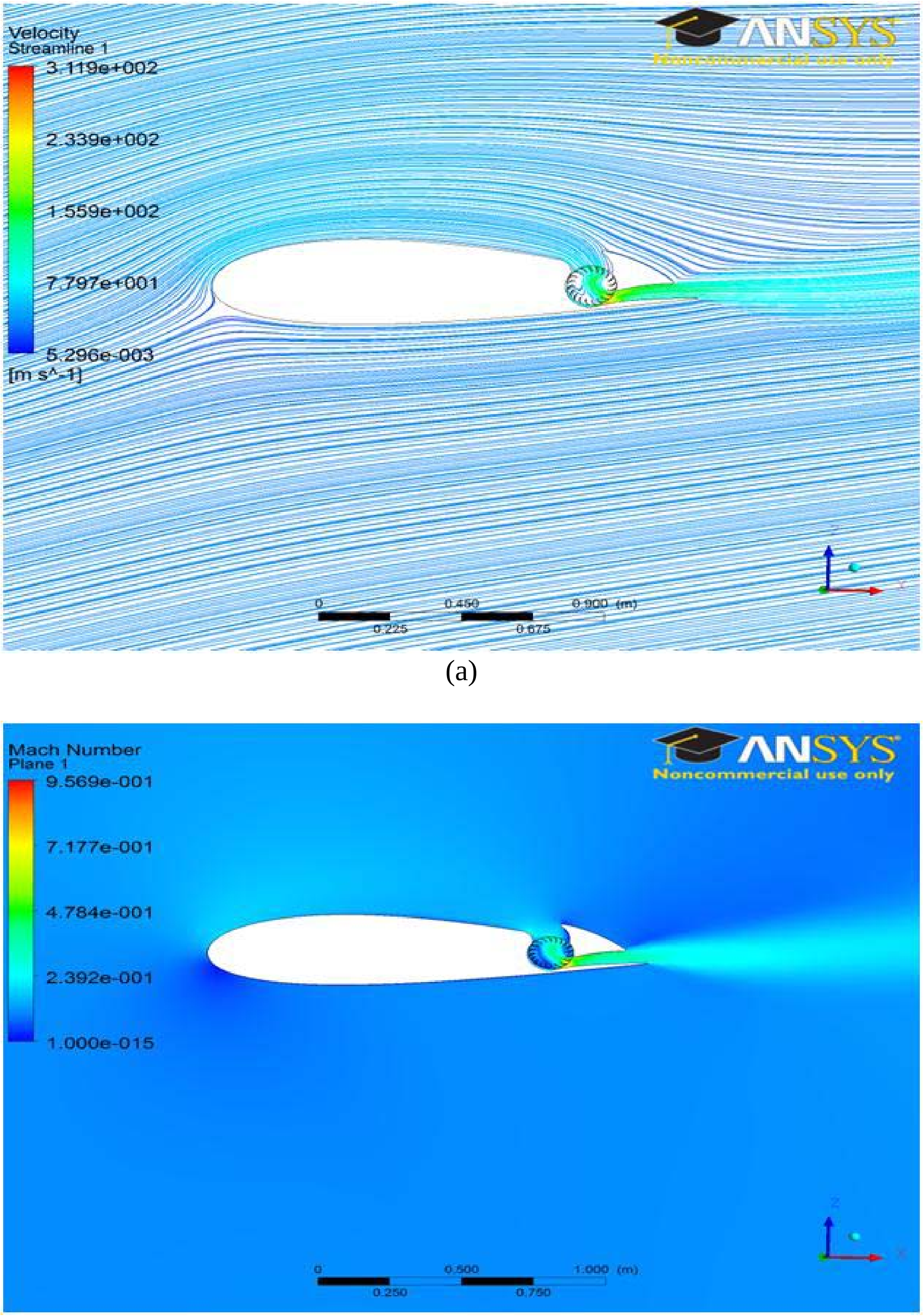

Figure 35. Embedded CFF in a NACA 2421 Airfoil (a) CFX-Post, Fully Embedded CFF Rotor, AOA 15^0, 20 Blades CFF, Streamlines, (b) CFX-Post, AOA 15^0, Mach Number Contour in the Mid-Plane Thickness

In the initial stages, it was envisioned that the CFF would be fully embedded in the airfoil wing. Thus, the NACA 2421, with chord length 1.6m, was selected to accommodate the 6-inch diameter CFF rotor (Figure 33 (a)). Calculations were made at two different AOA (8^0 and 15^0) and for the same free stream velocity conditions.

Table 13 includes data of lift and thrust forces for different AOA and airfoil types. For each CFF embedded airfoil, there are two main areas. The first one is the wing-only without the CFF rotor and the surface of it is characterized as “Viscous Walls.” The second part is the CFF rotor, which has the name “blades” in Table 13, because the forces act only those surfaces. The sum of these two parts, Viscous Walls and blades, form the net force result which is of interest. The minus sign in the force means force direction towards the leading edge of the airfoil, i.e., thrust instead of drag. As mentioned earlier, although the results for the drag and the thrust are questionable, those results will still be used to perform parametric studies between the different configurations.

From Table 13, it can be seen that the blades subtract lift, where the sum of lift remains higher compared with simple airfoils. This negative lift on behalf of blades was reasonable since the flow accelerated at the CFF outlet. The thrust also increased in the same way, because of the CFF rotation. From Table 13, comparing the NACA 2421 airfoil with 15^0 AOA using 30- and 20-bladed rotors at 12,000 rpm, it was concluded that the performance of a 20-bladed rotor CFF is higher. This was important since this study began as a motivation for CFD and experimental investigation, with different numbers of CFF rotor blades, section II.D 2. In addition, moving the axis of rotation of CFF rotor upwards in the aft portion of the airfoil changed its performance. Figure 36 shows the partially embedded CFF. Although the lift increased compared to the fully embedded CFF airfoil, the reduction in thrust was high—from 1.66421(N) to 1.02817(N) (Table 13). This led to the CFD conclusion that the fully embedded CFF airfoil performed better compared with the partially embedded CFF rotor model. The vertical translation upwards of the CFF rotor between the fully (30 mm) and partially embedded CFF rotor (59 mm) is 29 mm, where the center of design for the airfoil is the center of the CFF rotor, Appendix C.

Also, the effect of vertical translation in an embedded airfoil was examined in another profile, the NACA 2418. The chord distance of the CFF rotor was kept the same—1.2 m from the leading edge, approximately 75% of chord length. The vertical translation was 44 mm (Figure 37). The results for this propulsive airfoil at 12,000 rpm were not satisfactory regarding the gain in lift. The lift in Viscous Walls was 2.144 (N) where for the same simple airfoil type the lift from Abbot and Von Doenhoff [17] is 2.41 (N). On the other hand, the CFD thrust result was 1.701 (N), comparable with the fully embedded, 20 bladed CFF in the NACA 2421 at 15^0 AOA (Table 13). This results in the "CFD" conclusion that the upwards translation of the CFF rotor had a penalty either on lift or thrust, depending on the shape of the specific airfoil. For that reason, each case was different but for the configurations of Table 13, the NACA 2421 fully embedded type airfoil with 20 blades showed the higher gain in lift and thrust compared with other cases. Another fact that enhanced the performance of the particular airfoil from Table 13 was the "extended" acceleration length of air on the upper surface compared with the partially embedded CFF (Figure 35 (a)).

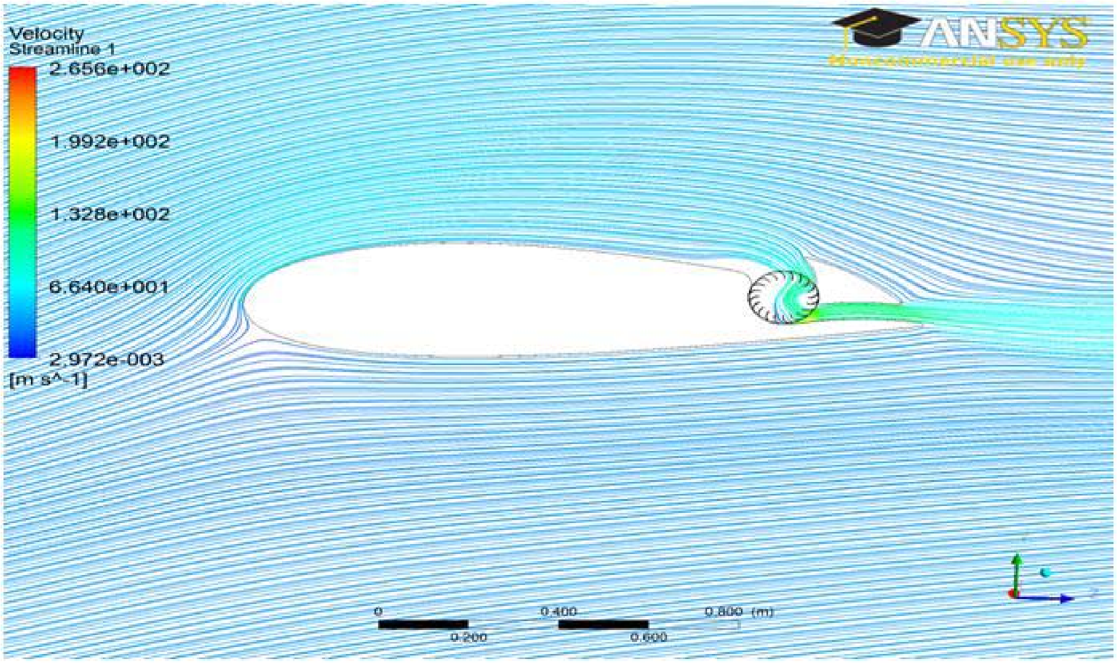

Figure 36. Partially Embedded CFF Rotor in a NACA 2421 Airfoil, AOA 15^0, Streamlines, 20 Blades CFF

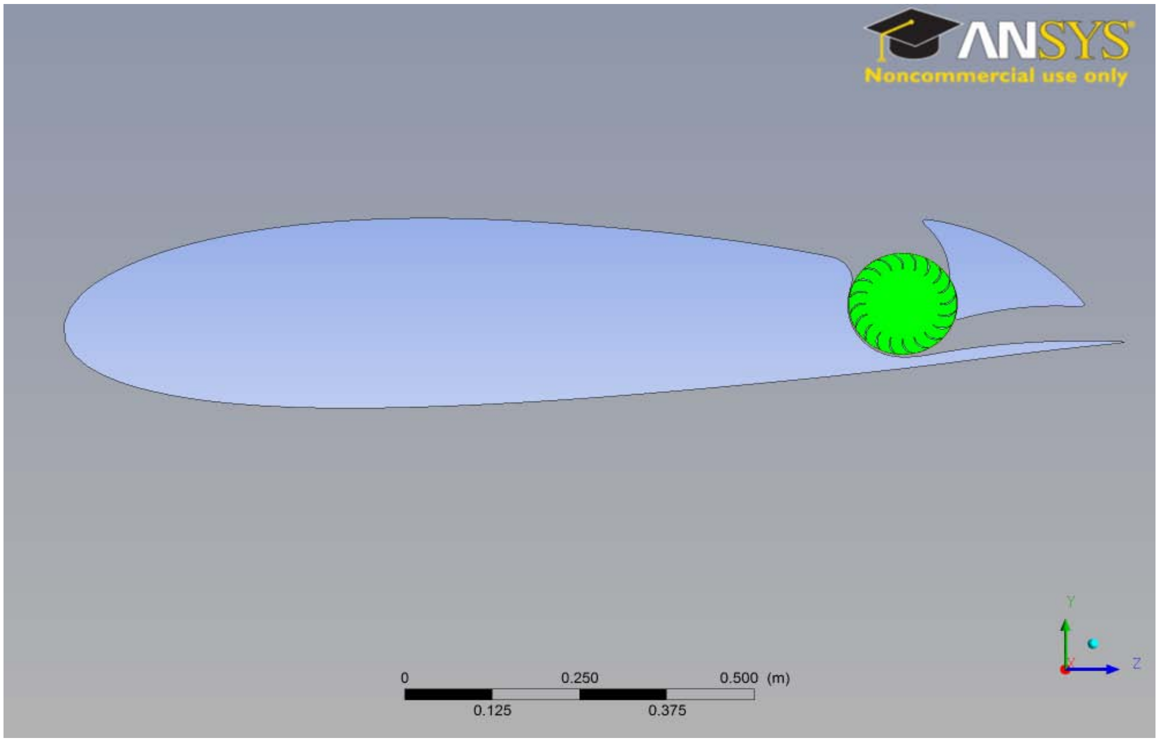

Figure 37. Partially Embedded CFF Rotor in a NACA 2418 Airfoil, 20 Blades, CFX-Pre

Finally, in Figures 38 and 39, it can be seen that the CFF embedded airfoil can withstand high AOAs without stalling, in comparison with Figure 32 (b). This was verified for 30^0 AOA on ANSYS-CFX in Figure 38 (b). Also real flight tests of a small unmanned aerial vehicle (UAV), from [5], have shown similar results. A characteristic like this makes the embedded CFF airfoil highly maneuverable and high gain lift device. In Table 13, using a 22-bladed rotor for the same fully embedded CFF airfoil, a remarkable value of C_L equal to 3.83 was calculated.

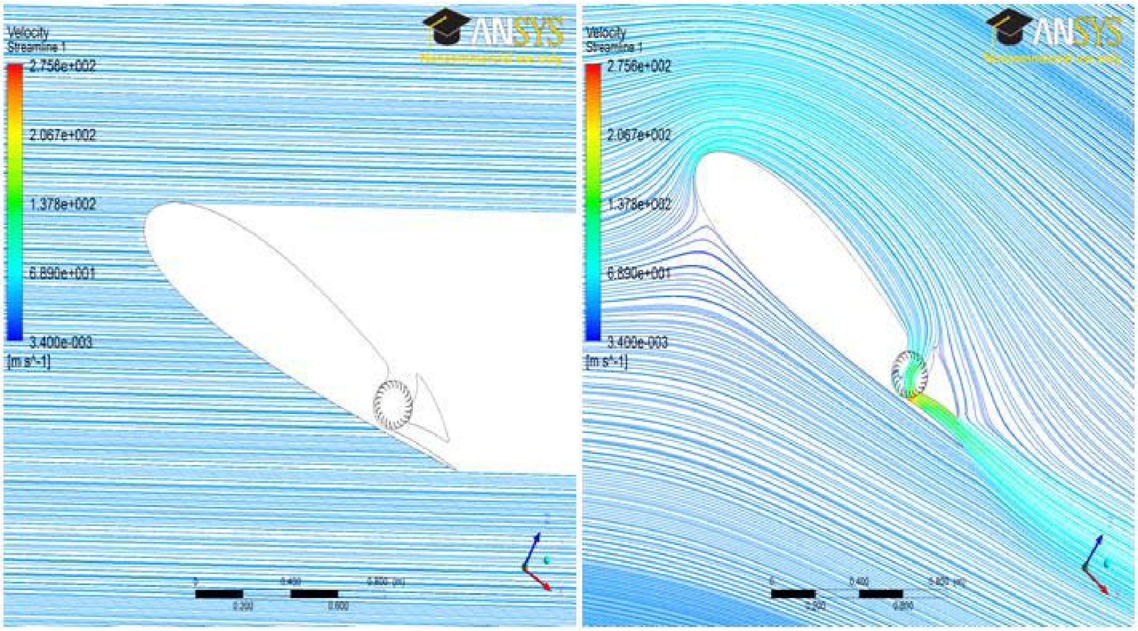

(a) (b)

Figure 38. Propulsive Wing NACA 2421 at 30^0 AOA, Fully Embedded 22-Bladed Rotor CFF (a) Initial Time Step Streamlines, (b) Steady-State' Time Step Streamlines, CFF On

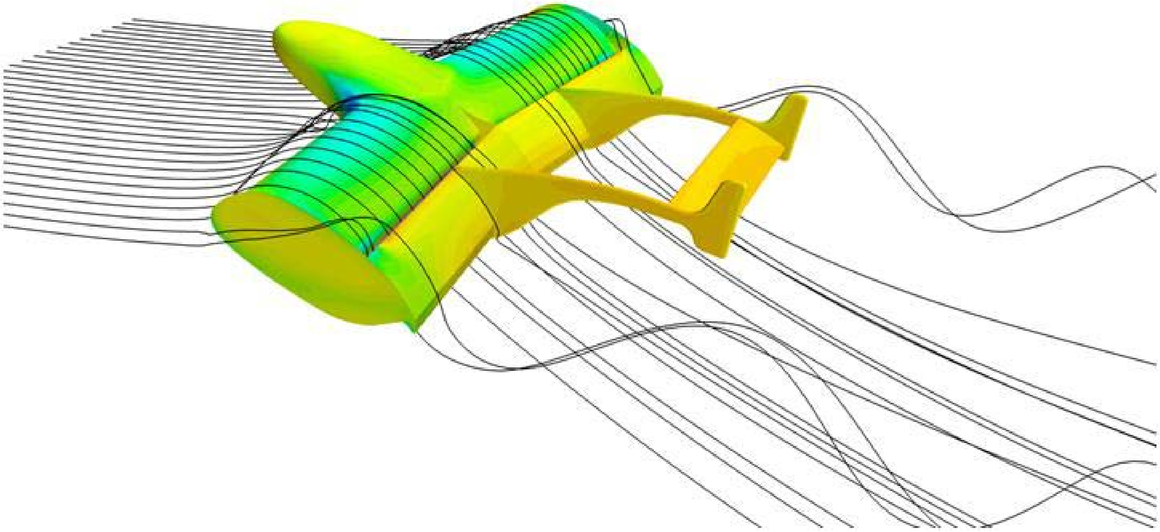

Figure 39. Numerical CFD Simulation of the Propulsive Wing UAV at High AOA. From [5]

V. RESULTS AND DISCUSSION

A. TEST PLAN A EXPERIMENTAL RESULTS

1. Total Pressure Ratio–Thrust per Unit Length

In the case of Test Plan A, the total pressure ratio was reduced for the 22-bladed rotor. Configuration 3, with the 30-bladed rotor, showed an experimentally higher pressure ratio, compared with the 22-bladed rotor. The difference at each speed line became higher above 5,000 rpm. The reduction in total pressure ratio was predicted by CFD, Tables 4, 5, 6 and Figure 41. At that point, Tables 4 and 5 at 4,000 rpm provide very accurate results compared with the experiment. Although the actual mass flow rate was slightly over that estimated from CFD model, the total pressure ratio predictions were satisfactory at 4,000 rpm and open-throttle condition. From Figure 40, the mass flow rate at each speed line and the open-throttle condition was also reduced for the 22-bladed rotor. The reduction of the total pressure ratio is something that affects the STOL distance. A higher pressure ratio helps the propulsive wing to become airborne more easily.

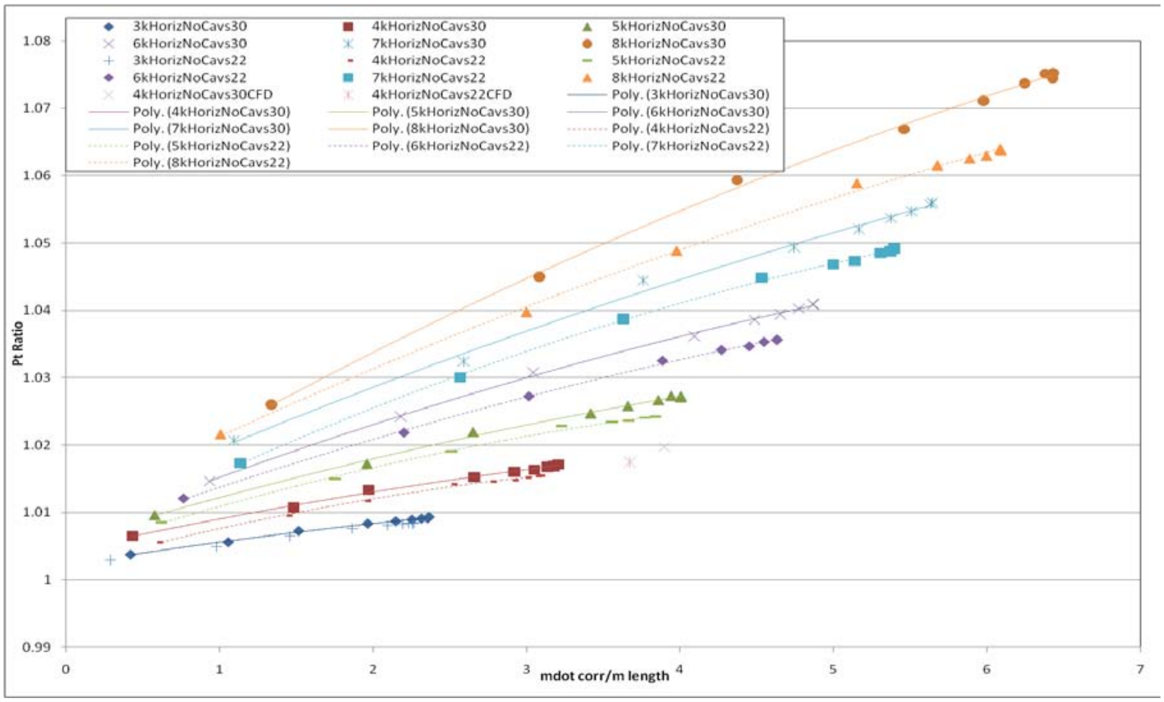

Figure 40. Test Plan A Experimental Results for Total Pressure Ratio

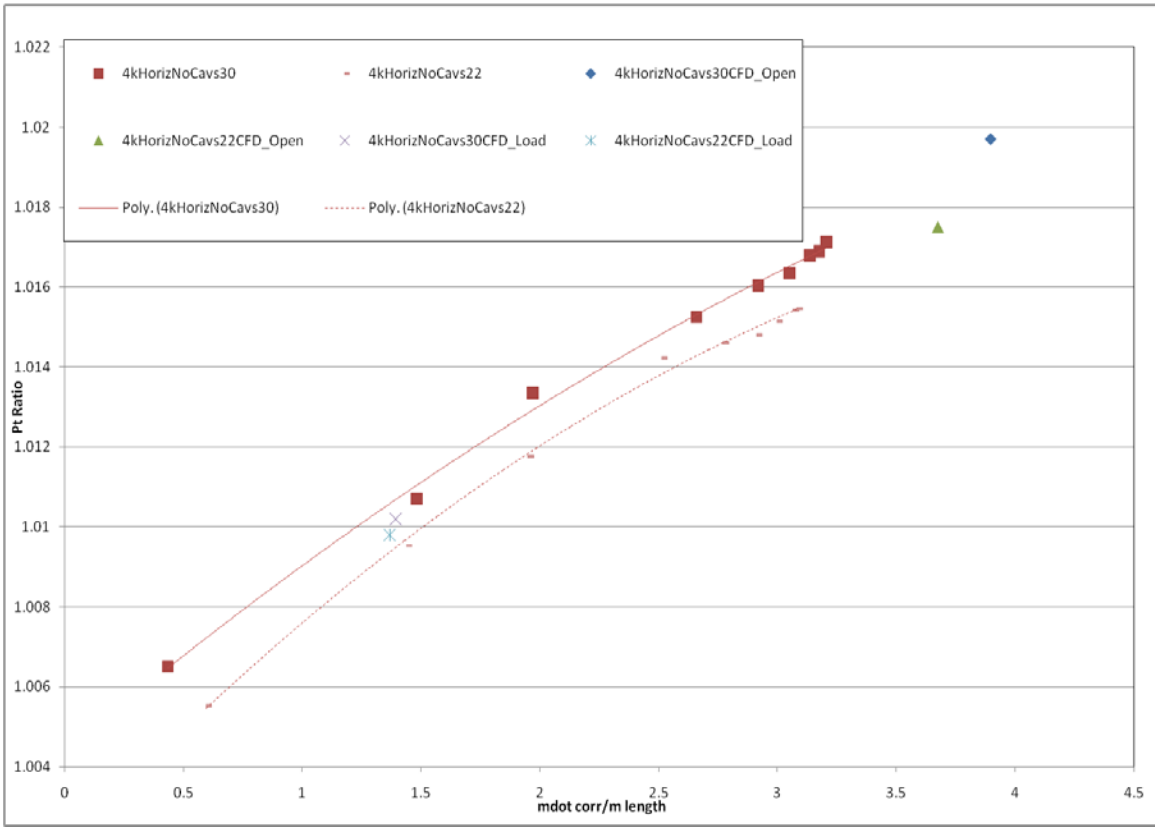

Figure 41. Test Plan A Experimental and CFD Results for Total Pressure Ratio at 4,000 rpm, Tables 4 and 6

In terms of thrust developed per unit length, Test Plan A with the 22-bladed rotor showed a reduction. However, this reduction was not very significant and, as a result, we can say that the two rotors produced similar thrust with Configuration 3 housing. Comparison between the two rotors (30 and 22 blades) from CFD (Tables 4–6) showed a relative reduction of thrust per unit length by 8% and 4% percent for the open-throttle and load conditions, respectively. This prediction was in accordance with experimental results. At higher mass flow rates, higher relative reduction of corrected thrust per unit length for the 22-bladed rotor can be seen (Figure 42).

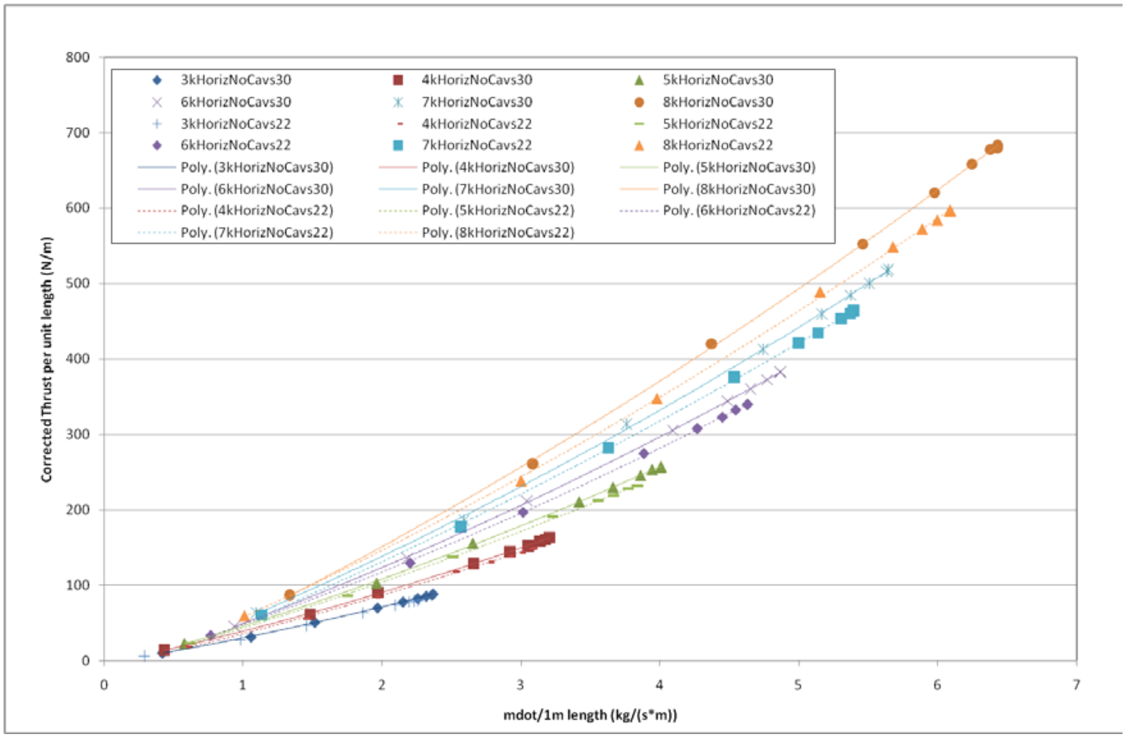

Figure 42. Test Plan A Experimental Results for Corrected Thrust per Unit Length

2. Efficiency–Specific Thrust

Figures 43 and 44 present the efficiency of the rotors (30 and 22 blades) at 3,000, 4,000 and 5,000 rpm. At lower speeds 3,000, 4,000 rpm the 22-bladed rotor operated more efficiently, especially at 3000 rpm. As the speed increased, the 22-bladed rotor became slightly better compared with the 30-bladed rotor (Figure 45). However, at higher mass flow rates and speeds, the 30-bladed rotor was more efficient (Figures 45 and 46). As a general rule, the two cases exhibited similar efficiencies for the intermediate speed ranges of 5,000, 6,000 and 7,000 rpm, whereas in the lower speed ranges of 3,000 to 4,000 rpm the 22-bladed rotor efficiency was better. In the high-speed case of 8,000 rpm, the 30-bladed rotor operated more efficiently (Figure 45).

In Figure 43, the experimental results at 4,000 rpm are compared with the CFD from Table 5 at open throttle condition. The CFD results follow the corresponding efficiency trend lines. With regard the throttle CFD simulation, the efficiencies on Table 6 do not match with those from this experiment. The efficiencies in Table 6, with and without high-speed numerics, were over-predicted. It is believed that the CFD model for efficiency, with the exit nozzle at the exit, is not physically realistic when compared with the actual outlet condition (butterfly throttling). The efficiency map for the whole speed range can be seen in Figure 46.

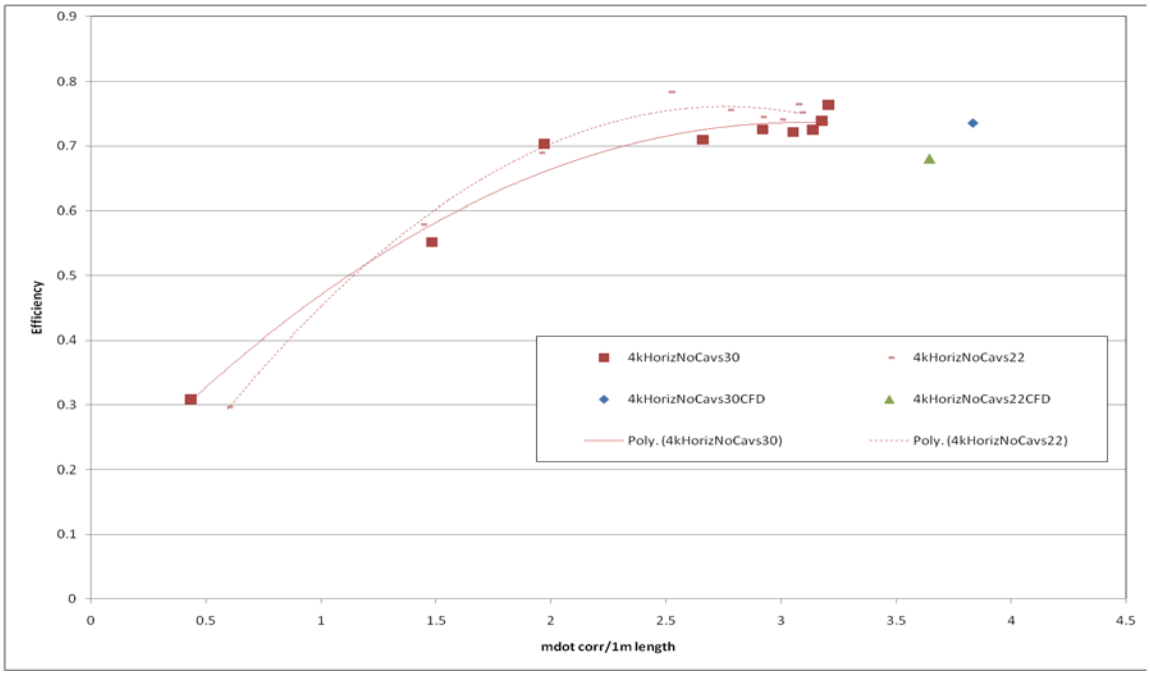

Figure 43. Test Plan A Experimental Results for Efficiency at 4,000 rpm and CFD. Results from Table 5

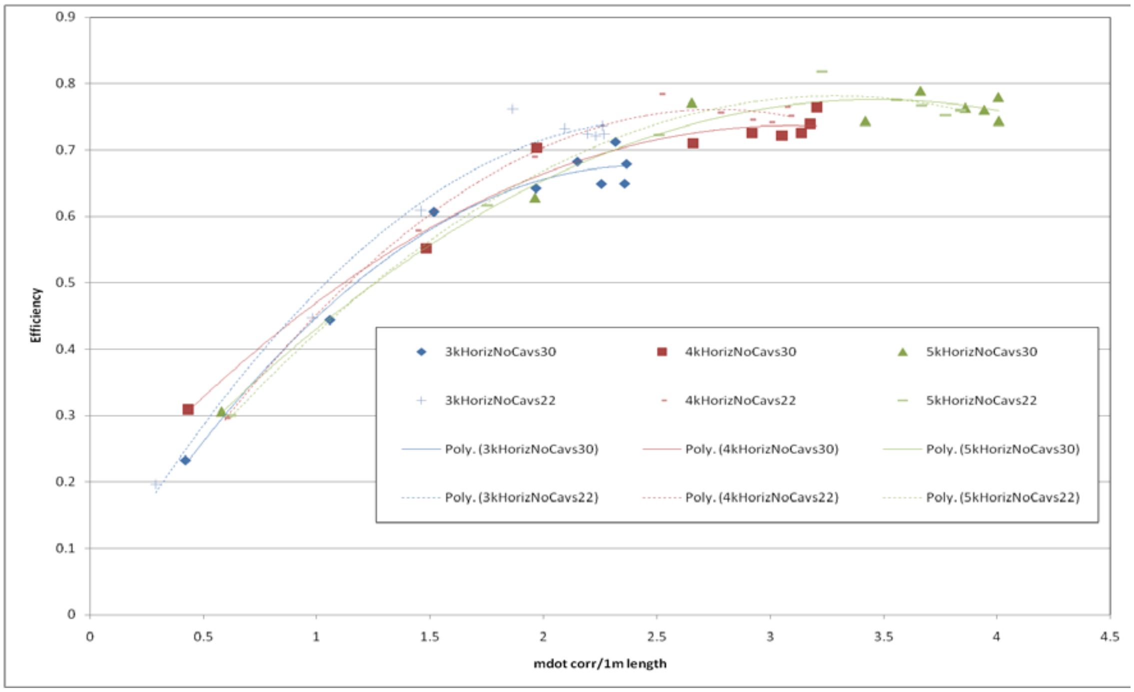

Figure 44. Test Plan A Experimental Results for Efficiency at 3,000, 4,000, and 5,000 rpm

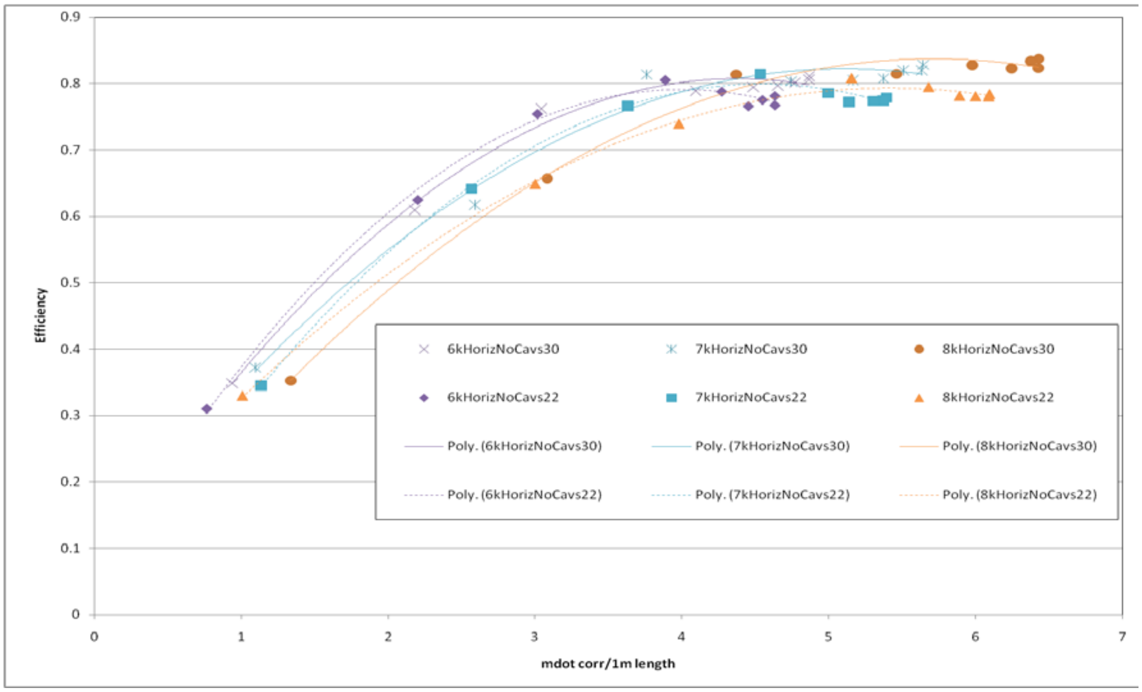

Figure 45. Test Plan A Results for Efficiency at 6,000, 7,000 and 8,000 rpm

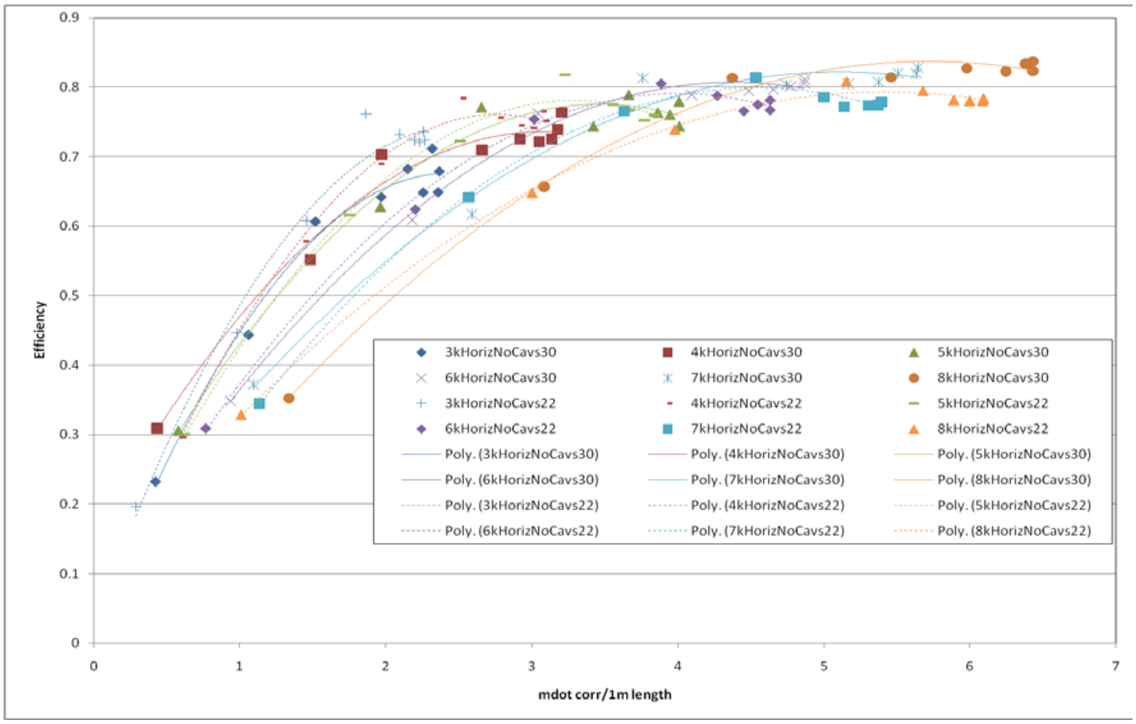

Figure 46. Test Plan A Experimental Results for Efficiency for the Whole Speed Range

The most interesting result was the specific thrust for Test Plan A (Figure 47). The 22-bladed rotor had higher specific thrust compared with the 30-bladed rotor for the whole speed range. This difference was significantly higher at the lower speeds of 3,000 and 4,000 rpm. The importance of specific thrust as a designing feature has already been mentioned. Trend lines at 6,000, 7,000 and 8,000 rpm for specific thrust and 30-bladed rotor, from Cordero [13], were corrected after re-testing. The higher specific thrust was also predicted for the 22-bladed rotor from CFD results of Tables 5 and 6, at 4,000 rpm with satisfactory accuracy. Experimental averaged data values of Test Plans A and B are located on Appendix D (Tables 14 and 15).

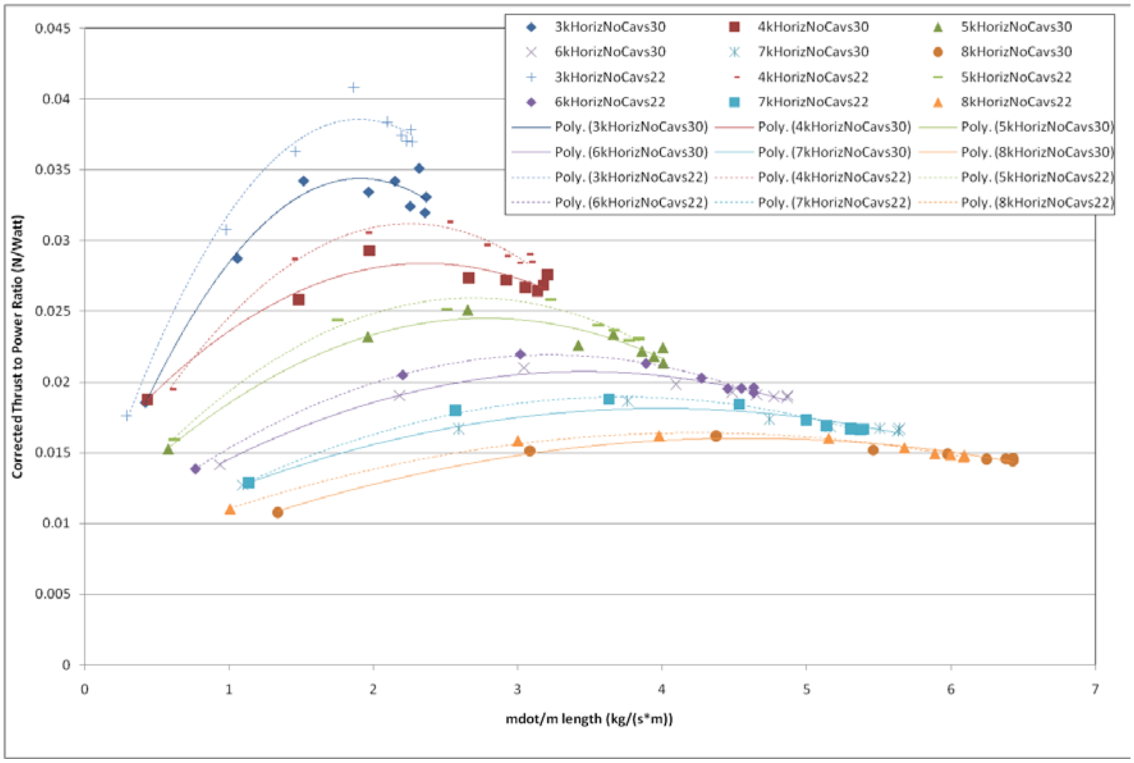

Figure 47. Test Plan A Experimental Results for Specific Thrust for the Whole Speed Range

B. TEST PLAN B EXPERIMENTAL RESULTS

1. Total Pressure Ratio–Thrust per Unit Length

A total pressure ratio graph between the two cases is depicted in Figure 48. Configuration 2 housing with the 22-bladed rotor showed a decrease of total pressure ratio compared with the 30-bladed rotor. This result was also verified from CFD simulations, but for Configuration 3 housing. As the number of rotor blades was decreased, either for open-throttle condition or with load, the pressure ratio became lower as well (CFD Tables 4 and 6). The difference of total pressure ratio in each speed line is quite constant for the whole mass flow range, especially above 4,000 rpm (Figure 48). That observation of constant difference reveals the linear “character” in performance of the new 22-bladed rotor. It is believed that in analogous experiments, with different numbers of rotor blades, that linear fashion will be repeated.

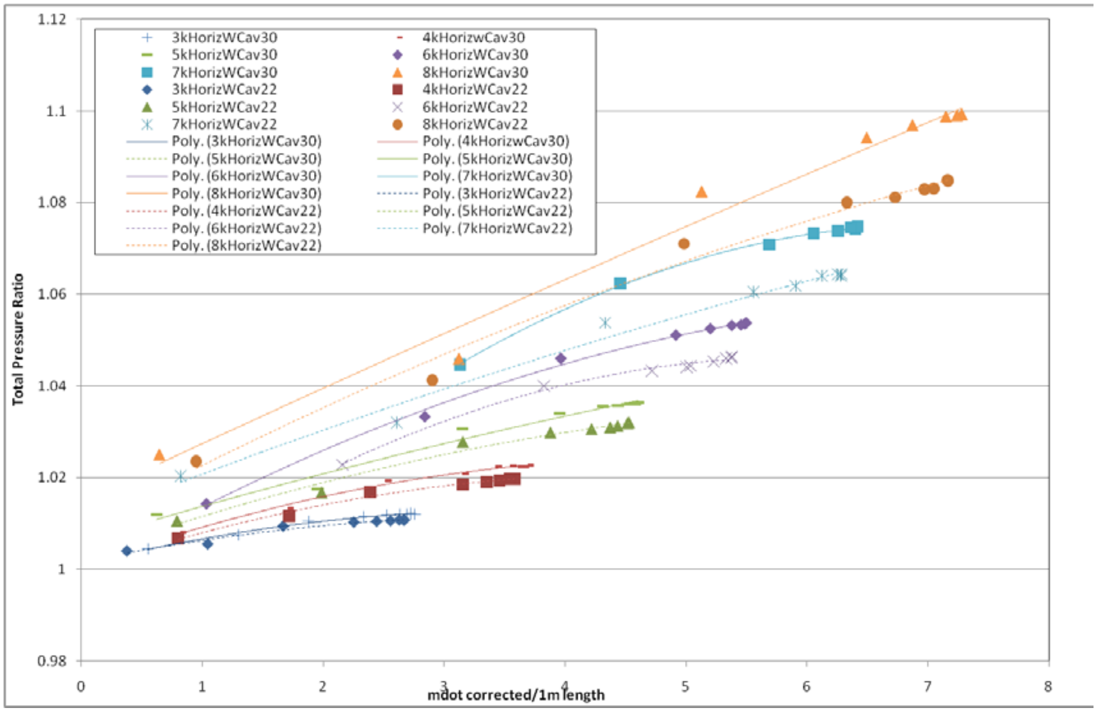

Figure 48. Test Plan B Experimental Results for Total Pressure Ratio

Similarly, the corrected thrust per unit length was decreased for the new 22-bladed rotor. That reduction was greater at higher mass flow rates and rotational speeds. Reduction in corrected thrust per unit length is in accordance with CFD simulations for Configuration 3; see CFD Tables 4 and 5. Also, the same CFD tables predicted lower mass flow rates for Configuration 3, using rotors with fewer blades, something that was verified experimentally for the new 22-bladed rotor. Figure 49 shows the corrected thrust per meter length for the two experimental cases at the speed range 3,000 rpm to 8,000 rpm.

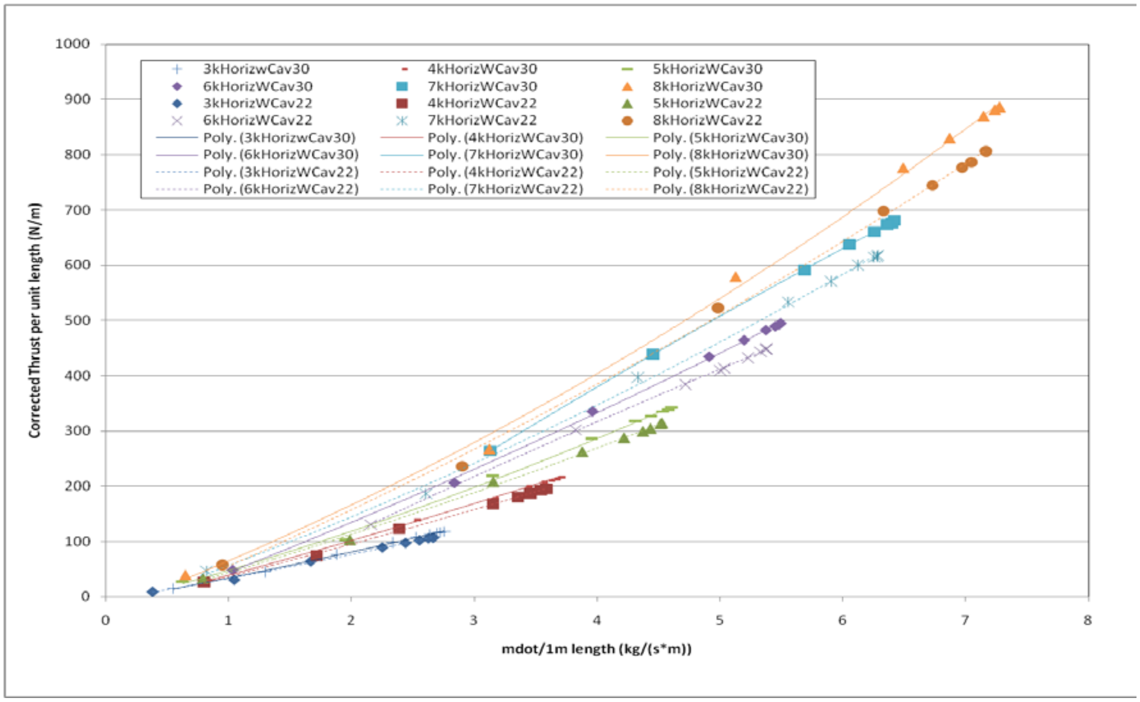

Figure 49. Test Plan B Experimental Results for Corrected Thrust per Unit Length

2. Efficiency–Specific Thrust

The decrease in efficiency for the 22-bladed rotor, compared to the 30-bladed rotor, can been seen in Figure 50. The experimental data for Test plan B referred to Configuration 2 housing. As a reminder, Configuration 2 is horizontal inlet with cavities (Figure 7(b)). For the speed range of 3,000 rpm to 8,000 rpm, we notice a decrease in efficiency by 3–10%. This decrease became greater at higher speeds, above 5,000 rpm. The same happened at higher mass flow rates. No CFD data results exist for Test Plan B because Test Plan A is of more interest and Configuration 3 in general.

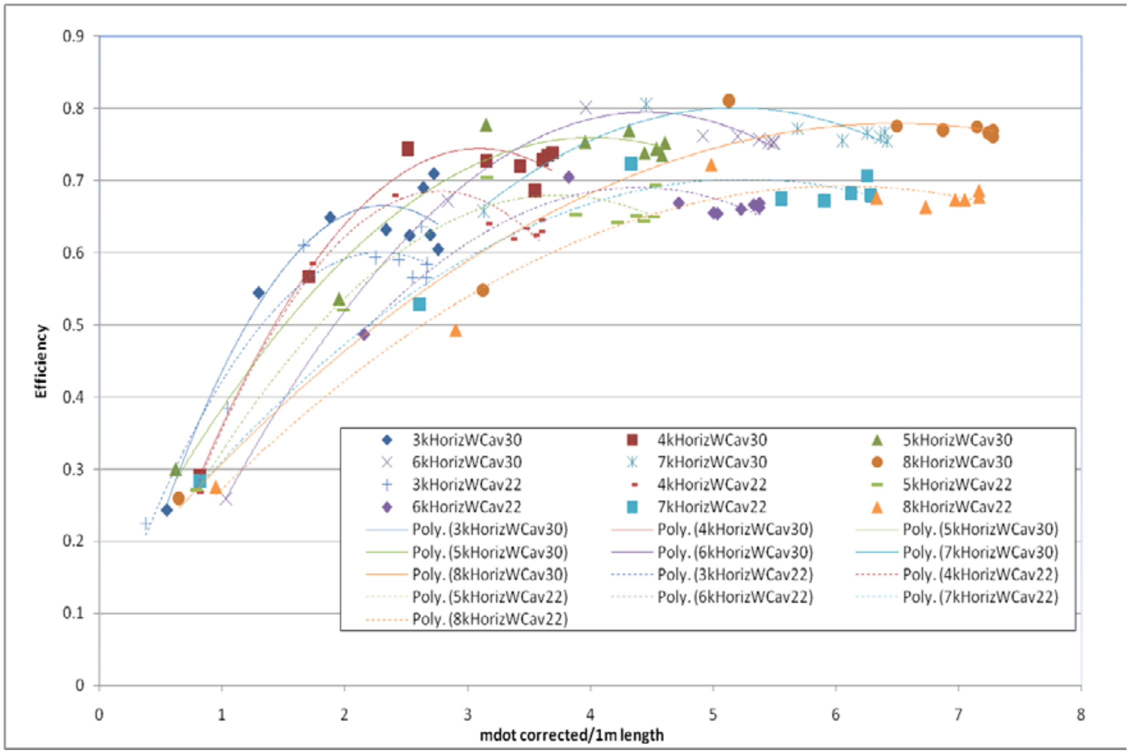

Figure 50. Test Plan B Experimental Results for Efficiency for the Whole Speed Range

On the other hand, the specific thrust in Figure 51 showed the opposite behavior compared to Test Plan A. For nearly all the speed lines, a slightly better performance for the 30-bladed rotor was noticed. At speeds between 7,000 rpm and 8,000 rpm, the trends between the two cases got closer, while from 3,000 rpm to 6,000 rpm the maximum deviation was observed. If the maximum values on each trend line are connected, the optimum operating line is constructed. This is the operating line for the highest power to thrust ratio at different rotational speeds.

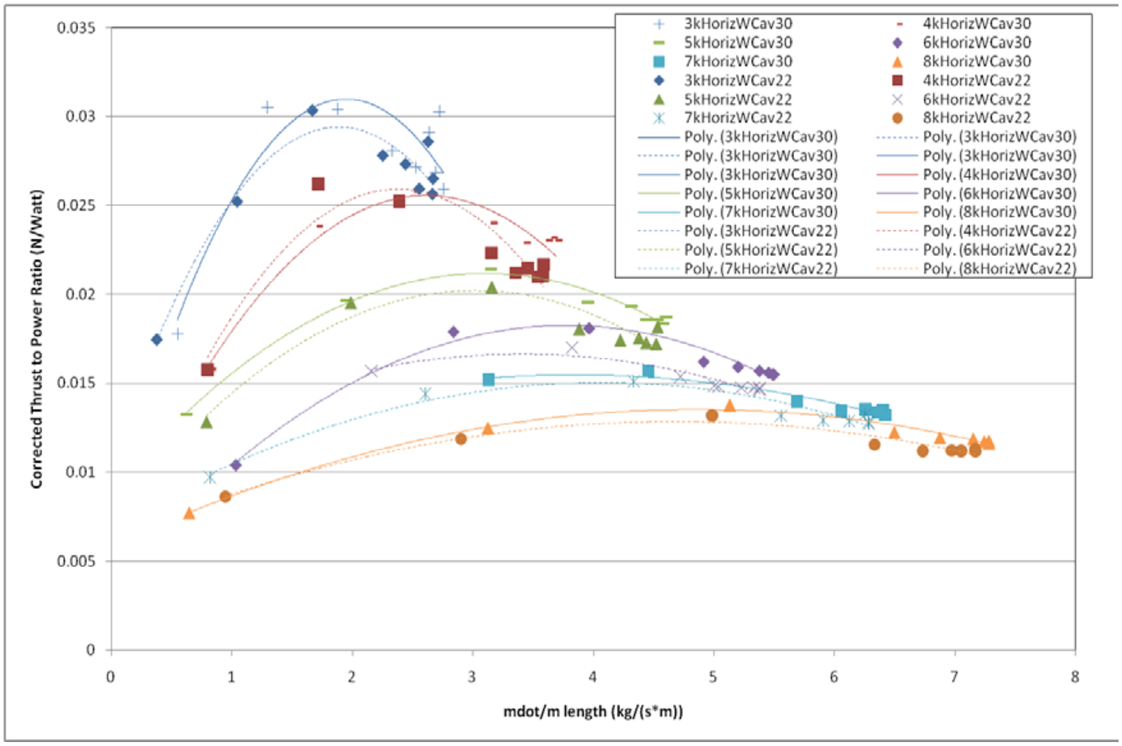

Figure 51. Test Plan B Experimental Results for Specific Thrust for the Whole Speed Range

THIS PAGE INTENTIONALLY LEFT BLANK

VI. CONCLUSIONS

The 22-bladed rotor with 6-inch diameter showed better efficiency for nearly the whole mass flow range and for the configuration with the horizontal inlet with no cavities, compared with the 30-bladed rotor. The increase in efficiency was higher at lower speeds, whereas at higher speeds the two rotors exhibit similar efficiencies. This increase in efficiency at lower speeds can reach 2–6%. In addition, the thrust produced for the two rotors was similar, with that of the 30-bladed rotor only slightly higher. The pressure ratio was also higher for the 30-bladed rotor. The most promising result was the higher thrust-to-power ratio for the 22-bladed rotor at all experimental speeds. Thrust-to-power ratio is a significant design and performance factor, especially if its effect is combined with the lighter weight 22-bladed rotor.

In contrast, for the housing configuration with horizontal inlet and with cavities, the 30-bladed rotor performed better. CFD simulations were conducted to investigate the blade number effect for the blanked-off case. Those CFD results compare favorably with experimental measurements at open throttle and using high-speed numerics in the solver to account for compressibility effects with 10% maximum absolute error.

A major step was the improvement of computational models. The 2-D meshing grid strategy, either for the CFF or propulsive wing, is a valuable tool. Parametric study calculations, among different configurations, needed less computational time to be completed. In addition, a MATLAB tool was developed to aid in the construction of CFF embedded airfoil design in SOLIDWORKS. Also, the high pay-load of the CFF embedded airfoil compared with conventional airfoils at various AOA was verified.

THIS PAGE INTENTIONALLY LEFT BLANK

VII. RECOMMENDATIONS

A CFF configuration with no cavities seems to be the most suitable for the application in a propulsive wing. In the same way, the new 22-bladed rotor seems promising to be embedded in an airfoil. However, other rotors with different number of blades can easily be tested with relatively low cost. In addition, further computational investigation is needed for optimization of the CFF embedded airfoil. In this study, only vertical translations of the CFF rotor were examined. The same investigation for horizontal translations can be performed. Similarly, geometric area changes (inlet, outlet ducts) can have an effect in maximizing the lift and the thrust. Other NACA airfoil types may be selected to accommodate the CFF rotor, for subsonic design, from Abbot and Von Doenhoff [17]. It would also be beneficial to simulate the takeoff condition of the propulsive wing. That simulation could be completed with minimal changes to existing simulation. This would involve changing the boundary conditions and repositioning the airfoil in the computational box.

After those calculations, the next step will be the construction of a real propulsive wing prototype. This step will be before the designing of a small UAV model, analogous to that from Kummer [5]. At this point, it is likely that external help from a private contractor will be needed, which may require additional funds. For improvement reasons, a future prototype model should be capable of easily accepting modifications. For example, the substitution of the rotor for one with a different number of rotor blades should be easy, analogous to the CFTA facility. Finally, further CFD simulations are needed for the investigation of the effect of thrust-vectoring on gain lift at the trailing edge of the embedded CFF airfoil.

THIS PAGE INTENTIONALLY LEFT BLANK

APPENDIX A. ANSYS CFX PRE SETTINGS

Once the casing and fan meshes had been generated and imported into CFX-PRE, the problem definition was completed. All models were run initially with default or solver-chosen initial values. The time selection for each transient problem was set until ten complete revolutions were reached. A settings demonstration for the embedded CFF airfoil is shown below with total time 0.05 sec, rotation speed 12,000 rpm, flight speed 35 m/s and AOA 15^0. Similar settings were used for the rest of the simulations and in close agreement from [13].

<u>10 Revolutions:</u>

- Simulation Type - Basic Settings
  - External Solver Coupling - None
  - Simulation Type
    - Option – Transient
  - Time Duration
    - Option – Total Time
    - Total Time – 0.05 [s] (dependent on rotational speed and desired number of revolutions, e.g. 12000 rpm for 0.05 seconds yields 10 complete revolutions)
  - Time Steps
    - Option – Adaptive (used to control RMS Courant number. Despite ANSYS CFX being an implicit solver, transient solutions can be quite sensitive to Courant or CFL number)
    - First Update Time – 0 [s]
    - Timestep Update Freq –1
    - Initial Timestep – 8.366e-006 [s]
  - Timestep Adaptation
    - Option – RMS Courant Number
    - Minimum Timestep – 8.366e-006 [s]
    - Maximum Timestep – 0.001 [s]
    - Courant Number – 1
  - Initial Time

        - Option – Automatic with Value
        - Time – 0 [s]
- Casing Domain – General Options
    - Basic Settings
        - Location – Select the appropriate domain/mesh file for your casing domain region which depends on how you set it up in CFX Mesh
        - Domain Type – Fluid Domain
        - Coord Frame – Coord 0
        - Fluids List – Air Ideal Gas
        - Morphology
            - Option – Continuous Fluid
    - Domain Models
        - Pressure
            - Reference Pressure – 1 [atm]
        - Buoyancy
            - Option – Non Buoyant
        - Domain Motion
            - Option – Stationary
        - Mesh Deformation
            - Option – None
- Casing Domain – Fluid Models
    - Heat Transfer
        - Option – Total Energy
        - Incl. Viscous Work Term – checked
    - Turbulence
        - Option – k-Epsilon
        - Wall Function – Scalable

    - Combustion
        - Option – None
    - Thermal Radiation
        - Option – None
- Casing Domain – Initialization
    - Domain Initialization – unchecked
- Casing Domain Boundary Conditions (The names of the boundaries will vary depending on how you named the regions in CFX MESH)
    - CasingSym1
        - Boundary Type – Symmetry
        - Location – CasingSym1 (names available in the drop down list again depend on how you name the regions in CFX MESH)
    - CasingSym2
        - Boundary Type – Symmetry
        - Location – CasingSym2 (names available in the drop down list again depend on how you name the regions in CFX MESH)
    - ViscousWalls – Basic Settings
        - Boundary Type – Wall
        - Location – ViscousWalls ((names available in the drop down list again depend on how you name the regions in CFX MESH)
        - Coord Frame – Unchecked
    - ViscousWalls – Boundary Details
        - Mass and Momentum
            - Option – No Slip Wall
            - Wall Velocity – Unchecked
        - Wall Roughness
            - Option – Smooth Wall
        - Heat Transfer
            - Option – Adiabatic
    - Domain Interface 1 Side 1 – Basic Settings
        - Boundary Type – Interface

    - Location – Casing Interface (names available in the drop-down list again depend on how you name the regions in CFX MESH)
    - Coord Frame – Unchecked
- Domain Interface 1 Side 1 – Boundary Details (This boundary is added once a Domain Interface is added by right-clicking on “Simulation” in the outline view in CFX PRE, selecting “Insert”, and then selecting “Domain Interface”)
    - Mass and Momentum
        - Option – conservative Interface Flux
    - Turbulence
        - Option – Conservative Interface Flux
    - Heat Transfer
        - Option – Conservative Interface Flux
    - Nonoverlap Conditions – Unchecked
- Inlet – Basic Settings
    - Boundary Type – Inlet
    - Location – Inlet (names available in the drop-down list again depend on how you name the regions in CFX MESH)
    - Coord Frame – Unchecked
- Inlet – Boundary Details
    - Flow Regime
        - Option – Subsonic
    - Mass And Momentum
        - Option – Cart.Vel.Components
        - U – 33.8074 [m/s]
        - V– 0 [m/s]
        - W– 9.05866 [m/s]
        - Relative Pressure – 0 [Pa]
    - Turbulence
        - Option – Medium (Intensity = 5%)

    - Heat Transfer
      - Option – Static Temperature
      - Static Temperature – 300 [K]
  - Outlet – Basic Settings
    - Boundary Type – Opening
    - Location – Outlet (names available in the drop down list again depend on how you name the regions in CFX MESH)
    - Coord Frame – Unchecked
  - Outlet – Boundary Details
    - Flow Regime
      - Option – Subsonic
    - Mass and Momentum
      - Option – Opening Pres. and Dirn
      - Relative Pressure – 0 [Pa]
    - Flow Direction
      - Option – Normal to Boundary Condition
    - Loss Coefficient – Unchecked
    - Turbulence
      - Option – Medium (Intensity = 5%)
    - Heat Transfer
      - Option – Static Temperature
      - Static Temperature – 300 [K]
- Rotor Domain – General Options
  - Basic Settings
    - Location – (names available in the drop down list again depend on how you name the regions in CFX MESH)
    - Domain Type – Fluid Domain
    - Fluids List – Air Ideal Gas
    - Coord Frame – Coord 0
  - Domain Models
    - Pressure
      - Reference Pressure – 1 [atm]

    - Buoyancy
      - Option – Non Buoyant
    - Domain Motion
      - Option – Rotating
      - Angular Velocity – (-)12,000 [rev min^-1] (+/- depends on how you set your global axis reference when building the solid model)
      - Alternate Rotation Model – Unchecked
      - Axis Definition
        - Option – Coordinate Axis
        - Rotation Axis – Global Y (depends on how you set your global rotation axis)
      - Mesh Deformation
        - Option – None
- Rotor Domain – Fluid Models
  - Heat Transfer
    - Option – total energy
    - Incl. Viscous Work Term – Checked
  - Turbulence
    - Option – k-Epsilon
    - Wall Function – Scalable
  - Combustion
    - Option – None
  - Thermal Radiation
    - Option – None
- Rotor Domain – Initialization
  - Domain Initialization – unchecked
- Rotor Domain – Boundary Conditions (The names of the boundaries will vary depending on how you named the regions in CFX MESH)
  - Blades – Basic Settings
    - Boundary Type – Wall
    - Location – Blades (names available in the drop down list again depend on how you name the regions in CFX MESH)

    - Coord Frame – Unchecked
    - Frame Type – Rotating
- Blades – Boundary Details
    - Mass and Momentum
        - Option – No Slip Wall
        - Wall Velocity – Unchecked
    - Wall Roughness
        - Option – Smooth Wall
    - Heat Transfer
        - Option – Adiabatic
- Domain Interface 1 Side 2 – Basic Settings
    - Boundary Type – Interface
    - Location – Rotor Interface (names available in the drop down list again depend on how you name the regions in CFX MESH)
    - Coord Frame – Unchecked
- Domain Interface 1 Side 2 – Boundary Details
    - Mass and Momentum
        - Option – conservative Interface Flux
    - Turbulence
        - Option – Conservative Interface Flux
    - Heat Transfer
        - Option – Conservative Interface Flux
        - Nonoverlap Conditions – Unchecked
- RotorSym1
    - Boundary Type – Symmetry
    - Location – RotorSym1 (names available in the drop-down list again depend on how you name the regions in CFX MESH)
- RotorSym2
    - Boundary Type – Symmetry

        - Location – RotorSym2 (names available in the drop-down list again depend on how you name the regions in CFX MESH)

- Domain Interface 1
    - Interface Type – Fluid Fluid
    - Interface Side 1
        - Domain (Filter) – CasingDomain (names available in the drop-down list again depend on how you name the regions in CFX MESH)
        - Region List – CasingInterface (names available in the drop-down list again depend on how you name the regions in CFX MESH)
    - Interface Side 2
        - Domain (Filter) – RotorDomain (names available in the drop-down list again depend on how you name the regions in CFX MESH)
        - Region List – RotorInterface (names available in the drop-down list again depend on how you name the regions in CFX MESH)
    - Interface Models
        - Option – General Connection
        - Frame Change/Mixing Model
            - Option – Transient Rotor Stator
        - Pitch Change
            - Option – Automatic
        - Mass and Momentum – Unchecked
    - Mesh Connection Method
        - Option – GGI
- Solver Control – Basic Settings
    - Advection Scheme
        - Option – Upwind
    - Transient Scheme
        - Option – Second Order Backward Euler

- Timestep Initialization
  - Option – Automatic
  - Lower Courant Number – Unchecked
  - Upper Courant Number – Unchecked
- Turbulence Numerics
  - Option – First Order
  - Convergence Control
    - Min. Coeff. Loops – 1
    - Max. Coeff. Loops – 3
    - Fluid Timescale
      - Timescale control – Coefficient Loops
  - Convergence Criteria
    - Residual Type – RMS
    - Residual Target – 1.E-4
    - Conservation Target – Value 1.E-4
  - Elapsed Time Control – Unchecked
- Solver Control – Advanced Options
  - Compressibility Control – Checked
    - Total Pressure Option – Unchecked
  - High Speed Numerics – Checked
- Output Control
  - Trn Results Tab
    - Transient Results
      - Select “add new item” button if nothing is indicated and accept default name of “Transient Results 1”
      - Transient Results 1
        - Option – Standard
        - File Compression – Default
        - Output Boundary Flows – Unchecked
        - Output Equation Residuals – Unchecked
        - Output Frequency
          - Option – Time Interval

- Time Interval – 0.001 [s] (chosen by user; in this case due to the large file size and lengthy processor down time for writing the file, I chose to have a transient results file written every 72 degrees of rotation, which translates to every 0.001 seconds when rotating at 12,000 rpm)

- Expert Parameters (in order to insert an Expert Parameter, user must first select “Insert” from main menu, then select “Solver”, then Select “Expert Parameter”)
  - I/O Control Tab
    - Transient Model and I/o
    - Transient initialization override – Checked
    - Transient initialization o – t
- Select “Write Solver File” Icon in top menu
  - Save the *.def file in your chosen location
  - Solver Menu
    - Select mode of processing
      - PVM Local Parallel
      - PVM Distributed Parallel
      - Etc.
    - Select number of mesh partitions
    - Select Location to write results file
    - Click “Start Run”

Follow on Revolutions or Resuming a Simulation

- Select the appropriate *.pre file
- Adjust time duration as necessary
- Select “Write Solver File” Icon in top menu
  - Save the *.def file in your chosen location
  - Solver Menu
    - Initial Values File – select appropriate *.res or *.trn file from which you are resuming the simulation from.
    - Interpolate Initial Values onto Def File Mesh – Checked

- Select mode of processing
    - PVM Local Parallel
    - PVM Distributed Parallel
    - Etc.
- Select number of mesh partitions
- Select Location to write results file
- Click “Start Run”

THIS PAGE INTENTIONALLY LEFT BLANK

APPENDIX B. CFF ROTOR GEOMETRY

The 6-inch diameter CFF model was first attempted to be presented as a 2-D drawing in MATLAB. For that purpose, an m-file was created with the necessary information for the blade geometry in x, y and z Cartesian coordinates. The blade points have been derived from the 12-inch diameter CFF, using a scaling factor. At the outer tip radius of the blade, the fault point is dictated with a comment on the side (Figure 2, paragraph II.B). Also, on the same code, is described the least square technique used for the blade thickness investigation.

```
%----------------------------------------------
%Curve 1,in in and with origin from O of the circle. Suction surface
A1=[2.95218275 -0.5252078   0 % units in
    2.95020555 -0.5139997   0
    2.94803905 -0.5028266   0
    2.9456839  -0.49169178  0
    2.9431408  -0.48059838  0
    2.9404104  -0.46954957  0
    2.9374935  -0.45854852  0
    2.934391   -0.44759838  0
    2.9311037  -0.43670228  0
    2.92763265 -0.42586333  0
    2.9239787  -0.41508464  0
    2.920143   -0.40436929  0
    2.91612665 -0.39372035  0
    2.91193075 -0.38314086  0
    2.9075565  -0.37263385  0
    2.9030052  -0.36220232  0
    2.8982781  -0.35184926  0
    2.8933766  -0.34157763  0
    2.88830205 -0.33139037  0
    2.88305595 -0.32129039  0
    2.87763975 -0.31128059  0
    2.87205505 -0.30136382  0
    2.86630345 -0.29154292  0
    2.8603865  -0.28182071  0
    2.85430605 -0.27219996  0
    2.8480637  -0.26268342  0
    2.8416613  -0.25327382  0
    2.83510065 -0.24397385  0
    2.8283837  -0.23478618  0
    2.8215123  -0.22571342  0
    2.8144884  -0.21675817  0
    2.8073141  -0.207923    0
    2.79999135 -0.19921044  0
    2.7925223  -0.19062297  0
    2.7849091  -0.18216305  0
    2.7771539  -0.1738331   0
    2.7692589  -0.16563551  0
```

```
2.7612264  -0.15757262  0
2.7530587  -0.14964674  0
2.7447581  -0.14186013  0
2.736327   -0.13421503  0
2.72776775 -0.12671361  0
2.7190829  -0.11935803  0
2.7102749  -0.11215039  0
2.70134625 -0.10509275  0
2.6922995  -0.09818712  0
2.68313725 -0.0914355   0
2.67386215 -0.0848398   0
2.6644768  -0.07840191  0
2.6549839  -0.07212369  0
2.64538615 -0.06600691  0
2.63568635 -0.06005333  0
2.62588725 -0.05426466  0
2.61599165 -0.04864255  0
2.60600235 -0.04318861  0
2.59592225 -0.03790439  0
2.58575425 -0.03279142  0
2.5755012  -0.02785115  0
2.56516605 -0.023085    0
2.5547518  -0.01849432  0
2.54426135 -0.01408044  0
2.5336978  -0.00984462  0
2.5230641  -0.00578806  0
2.5123633  -0.00191194  0
2.5015985   0.00178265  0
2.49077275  0.00529465  0
2.47988915  0.00862305  0
2.4689508   0.0117669   0
2.4579608   0.01472529  0
2.4469224   0.01749739  0
2.4358387   0.02008241  0
2.4247128   0.02247959  0
2.413548    0.02468825  0
2.40234745  0.02670778  0
2.3911143   0.02853757  0
2.37985185  0.03017712  0
2.36856325  0.03162595  0
2.3572518   0.03288365  0
2.34592065  0.03394986  0
2.33457315  0.03482428  0
2.32321245  0.03550664  0
2.3118418   0.03599677  0
2.3004645   0.03629451  0
2.28908385  0.03639979  0
2.277703    0.03631257  0
2.26632525  0.03603288  0
2.25495385  0.03556079  0
2.2435921   0.03489645  0
2.2322432   0.03404005  0
2.2209104   0.03299182  0
2.2095969   0.03175207  0
2.19830605  0.03032115  0
```

```
    2.187041    0.02869947  0
    2.175805    0.0268875   0
    2.16460125  0.02488575  0
    2.15343295  0.0226948   0
    2.1423033   0.02031528  0
    2.13121545  0.01774785  0
    2.12017265  0.01499327  0
    2.10917805  0.01205232  0];
%plot(A1(:,1),A1(:,2),'-')
%Curve 2,in in and with origin from O of the circle. Pressure surface
A2=[2.11313405 -0.01246923 0 % units in
    2.123602   -0.01174153 0
    2.1340786  -0.01115033 0
    2.144562   -0.01069571 0
    2.1550504  -0.01037777 0
    2.1655421  -0.01019655 0
    2.17603525 -0.01015209 0
    2.18652805 -0.01024439 0
    2.1970188  -0.01047344 0
    2.20750565 -0.0108392  0
    2.21798685 -0.0113416  0
    2.22846065 -0.01198056 0
    2.2389252  -0.01275598 0
    2.24937875 -0.01366771 0
    2.25981955 -0.01471561 0
    2.2702458  -0.0158995  0
    2.2806557  -0.01721918 0
    2.29104755 -0.01867442 0
    2.30141955 -0.02026497 0
    2.3117699  -0.02199057 0
    2.32209695 -0.02385092 0
    2.3323988  -0.0258457  0
    2.34267385 -0.02797459 0
    2.35292025 -0.03023721 0
    2.36313625 -0.03263317 0
    2.3733202  -0.03516209 0
    2.38347035 -0.03782352 0
    2.3935849  -0.04061701 0
    2.4036622  -0.04354208 0
    2.41370055 -0.04659825 0
    2.42369815 -0.04978499 0
    2.4336534  -0.05310176 0
    2.4435646  -0.056548   0
    2.45343005 -0.06012312 0
    2.463248   -0.06382652 0
    2.4730169  -0.06765755 0
    2.48273505 -0.07161559 0
    2.49240075 -0.07569994 0
    2.50201245 -0.07990993 0
    2.5115684  -0.08424482 0
    2.5210671  -0.0887039  0
    2.53050685 -0.09328639 0
    2.53988605 -0.09799152 0
    2.54920315 -0.1028185  0
    2.55845655 -0.1077665  0
```

```
2.5676447  -0.11283467 0
2.576766   -0.11802217 0
2.5858189  -0.12332811 0
2.59480185 -0.12875158 0
2.6037134  -0.13429167 0
2.612552   -0.13994744 0
2.6213161  -0.14571792 0
2.63000425 -0.15160213 0
2.638615   -0.15759908 0
2.64714685 -0.16370775 0
2.65559835 -0.16992709 0
2.66396805 -0.17625605 0
2.6722546  -0.18269356 0
2.6804565  -0.18923853 0
2.68857245 -0.19588983 0
2.696601   -0.20264635 0
2.7045408  -0.20950693 0
2.7123905  -0.21647041 0
2.7201488  -0.22353561 0
2.72781435 -0.23070132 0
2.73538585 -0.23796632 0
2.74286205 -0.2453294  0
2.7502416  -0.25278928 0
2.75752335 -0.26034471 0
2.764706   -0.2679944  0
2.7717883  -0.27573706 0
2.77876915 -0.28357136 0
2.78564725 -0.29149598 0
2.7924215  -0.29950957 0
2.79909075 -0.30761077 0
2.8056538  -0.31579821 0
2.81210965 -0.32407048 0
2.8184571  -0.3324262  0
2.8246951  -0.34086393 0
2.8308226  -0.34938224 0
2.8368386  -0.3579797  0
2.842742   -0.36665483 0
2.8485318  -0.37540616 0
2.8542071  -0.38423221 0
2.8597669  -0.39313148 0
2.8652102  -0.40210245 0
2.87053615 -0.41114361 0
2.8757438  -0.42025341 0
2.8808323  -0.42943031 0
2.8858007  -0.43867275 0
2.8906483  -0.44797916 0
2.89537415 -0.45734795 0
2.8999775  -0.46677755 0
2.90445755 -0.47626634 0
2.90881355 -0.48581271 0
2.9130448  -0.49541505 0
2.9171505  -0.5050717  0
2.92113    -0.5147811  0
2.92498265 -0.52454145 0
2.9287077  -0.53435125 0];
```

```
%plot(A1(:,1),A1(:,2),'b-',A2(:,1),A2(:,2),'r-')
%Curve 3,in in and with origin from O of the circle. Outer tip
edge/without correction
A3=[2.9287077  -0.53435125  0 % units in
    2.929338   -0.53567625  0
    2.93041625 -0.5372887   0
    2.93173095 -0.5387149   0
    2.93325045 -0.53992055  0
    2.9349382  -0.5408766   0
    2.93675355 -0.54156005  0
    2.93865275 -0.5419544   0
    2.94059015 -0.54205015  0
    2.942519   -0.54184505  0
    2.9443929  -0.541344    0
    2.9461667  -0.54055905  0
    2.9477977  -0.53950915  0
    2.94924665 -0.53821955  0
    2.95047865 -0.5367213   0
    2.951464   -0.53505045  0
    2.952179   -0.53324735  0
    2.95260645 -0.5313553   0 %fault point, out of circle,|norm|>3 in
    2.952736   -0.5294199   0
    2.9525646  -0.52748775  0
    2.95218275 -0.5252078   0];
%Curve 4,in in and with origin from O of the circle. Inner tip edge
A4=[2.10917805  0.01205232  0 % units in
    2.10564855  0.01045503  0
    2.1041153   0.00927077  0
    2.1027835   0.00786383  0
    2.1016851   0.00626799  0
    2.10084645  0.00452159  0
    2.10028775  0.00266658  0
    2.10002235  0.00074752  0
    2.10005675 -0.0011895   0
    2.10038995 -0.00309795  0
    2.1010141  -0.00493198  0
    2.10191415 -0.00664754  0
    2.10306845 -0.00820342  0
    2.10444935 -0.00956226  0
    2.1060236  -0.0106914   0
    2.1077534  -0.01156373  0
    2.10959725 -0.01215829  0
    2.1115108  -0.0124608   0
    2.11313405 -0.01246923  0];

r=3; % CFF diameter
f=[0:0.01:2*pi];
x=r*cos(f);
y=r*sin(f);
plot(A1(:,1),A1(:,2),'b-',A2(:,1),A2(:,2),'r-',A3(:,1),A3(:,2),'g*-
',A4(:,1),A4(:,2),'y-',x,y,'black')
%List square approximation polynomio for curve 1,suction side
D1=[A1(:,1).^3 A1(:,1).^2 A1(:,1) ones(100,1)];
K1=inv(D1'*D1)*(D1'*A1(:,2)); %coefficients of polynomio a3,a2,a1,a0.
x1=A1(:,1)';
```

```
y1=(K1(1,1))*x1.^3+(K1(2,1))*x1.^2+K1(3,1)*x1+K1(4,1); %magenta
color,suction side
plot(A1(:,1),A1(:,2),'b-',A2(:,1),A2(:,2),'r-',A3(:,1),A3(:,2),'g*-
',A4(:,1),A4(:,2),'y-',x,y,'black',x1,y1,'magenta-')
xlabel('x axis, in'); ylabel('y axis, in'); grid on;
legend('Suction side','Pressure side','Outer tip edge','Inner tip
edge','CFF rotor');
Title('CFF rotor, 2D representation')
%gtext('Trailing edge')
%List square approximation polynomio for curve 2,pressure side
D2=[A2(:,1).^3 A2(:,1).^2 A2(:,1) ones(100,1)];
K2=inv(D2'*D2)*(D2'*A2(:,2)); %coefficients of polynomio a3,a2,a1,a0.
x2=A2(:,1)';
y2=(K2(1,1))*x2.^3+(K2(2,1))*x2.^2+K2(3,1)*x2+K2(4,1); %pressure side
plot(A1(:,1),A1(:,2),'b-',A2(:,1),A2(:,2),'r-',A3(:,1),A3(:,2),'g*-
',A4(:,1),A4(:,2),'y-',x,y,'black',x2,y2,'black-')
xlabel('x axis,in'); ylabel('y axis,in'); grid on;
legend('Suction side','Pressure side','Outer tip edge','Inner tip
edge','CFF rotor');
Title('CFF rotor, 2D representation')
%-----------------------------------------------------------
x1new=[2.176:0.01:2.904]; % x values common for both y1 and y2
size(A1);
size(A2);
y1new=(K1(1,1))*x1new.^3+(K1(2,1))*x1new.^2+K1(3,1)*x1new+K1(4,1);
%suction side
y2new=(K2(1,1))*x1new.^3+(K2(2,1))*x1new.^2+K2(3,1)*x1new+K2(4,1);
%pressure side
D=[x1new' y1new' y2new'];
d=abs(y1new-y2new);
dd=1.4*d; %Increasing by x %
y1new=y2new+dd;
format  short g
T=[x1new' y1new']
T1=(25.4)*T
size(T)
plot(A1(:,1),A1(:,2),'b-',A2(:,1),A2(:,2),'r-',A3(:,1),A3(:,2),'g*-
',A4(:,1),A4(:,2),'y-',x,y,'black',x1new,y1new,'green')%x1,y1,'magenta-
'
xlabel('x axis,in'); ylabel('y axis,in'); grid on;
legend('Suction side','Pressure side','Outer tip edge','Inner tip
edge','CFF rotor');
Title('CFF rotor, 2D representation')
gtext('40% increase thickness')
```

APPENDIX C. PROPULSIVE WING

In this appendix is demonstrated the method to build up 2-D airfoils, either cambered or symmetric, used in CFD simulations. A MATLAB code has been created for each case with equations described from Abbott and Von Doenhoff [17]. The inputs to the code by the user are: the chord length, the thickness as a percent of chord length, percent of maximum chamber and percent of chord length where the maximum camber happens. Below is illustrated a demo of the cambered NACA 2421 airfoil, with chord length 1.6 m. Also, on the same airfoil, the circle position of the CFF is drawn, something that helps in the designing of a propulsive wing at SOLIDWORKS.

```
%--------------------------------------------------------------
%CAMBERAIRFOIL This m-file calculates for a camber airfoil the
%geometric points x,y.The equations comes from wikipedia an on-line
%encyclopedia and Abbott, Ira H., and Von Doenhoff, Albert E. (1959),
%Theory of Wing Sections, Section 4.2, Dover Publications Inc., New
%York, Standard Book Number 486-60586-8 [15]
%Also this m-file calculates the points of mean line.
%Below is the calculation of a NACA 2421.
c=1.6;     %chord length, here in [m]
t=0.21*c;  %thickness, percent of chord
m=0.02;    %percent of maximum camber
p=0.4;     %percent of chord where the maximum camber happens
x1=[0:0.02:p*c];
x2=[p*c+0.1:0.1:c];
x=[x1 x2]; % spatial distribution
y=(t/0.20)*(0.29690*sqrt(x/c)-0.12600*(x/c)-
0.35160*(x/c).^2+0.28430*(x/c).^3-0.10150*(x/c).^4);
%y thickness distribution
yc1=(m/p^2)*(2*p*x1-(x1.^2/c));  %Forward mean camber line
yc2=((m*c)/((1-p)^2))*(1-2*p+2*p.*x2/c- (1/c^2)*x2.^2); %Aft mean
camber line
yc=[yc1 yc2]; % Mean camber line points
dy1=(2*m/(p^2))*(p-(x1/c));     %Derivative1
dy2=(2*m/((1-p)^2))*(p-(x2/c)); %Derivative2
th1=atan(dy1);
th2=atan(dy2);
thita=[th1 th2];
xu=x-y.*sin(thita);
yc=[yc1 yc2];
yu=yc+y.*cos(thita);
xl=x+y.*sin(thita);
yl=yc-y.*cos(thita);
disp(  '          x ,   y     in mm   ')
Au=[(xu'-1.2) (yu'-0.03)]*1000 % Upper surface points
Al=[(xl'-1.2) (yl'-0.03)]*1000 % Lower surface points
size(Au)
```

```
size(Al)
r=2*38.608/1000; f=[0:0.01:2*pi]; %CFF cycle, origin the cycle center
xr=r*cos(f);
yr=r*sin(f);
A=[ x'  y'];
 plot(xu-1.2,yu-0.03,'b-*',x-1.2,yc-0.03,'r-*',xl-1.2,yl-0.03,'b-
^',xr,yr,'b-') %Translation by 1.2 in xu,x,xl
 %plot(xu-1.2,yu-0.059,'b-*',x-1.2,yc-0.059,'r-*',xl-1.2,yl-0.059,'b-
^')
 gtext('NACA 2421')
%Translation by 0.03 in yu,yc,yl
 grid on
 xlabel('x')
 ylabel('y')
 title('Camber Airfoil')
 legend('Upper surface','Mean line','Lower surface')
```

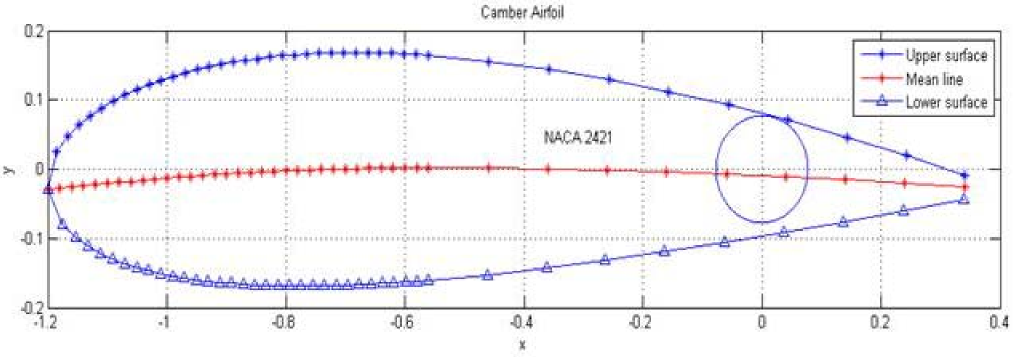

Figure 52. NACA 2421 Airfoil with Fully Embedded CFF

```
%-------------------------------------------------------------
%SYMAIRFOIL This m-file calculates for Symmetric airfoil NACA 00xx
%the geometric points (x/c,y/c) and (x,y) for a given thickness t of %
%chord line.
%Below is the calculation of a NACA 0010.
c=2;         % chord length
t=0.10*c;    % thickness
x=[0:0.025:0.15 0.15:0.05:c];
y=(t/0.20)*(0.29690*sqrt(x/c)-0.12600*(x/c)-
0.35160*(x/c).^2+0.28430*(x/c).^3-0.10150*(x/c).^4);
disp('x/c,   y/c ,   x ,   y')
A=[(x/c)'  (y/c)'  x'  y']
 plot(x/c,y/c,'-*',x/c,-y/c,'-*',x,y,'-*',x,-y,'-*')
 gtext('NACA 0010')
 grid on
 xlabel('x/c,x')
 ylabel('y/c,y')
 title('Symmetric Airfoil')
 legend('Upper surface scaled','Lower surface scaled','Upper
surface','Lower surface')
```

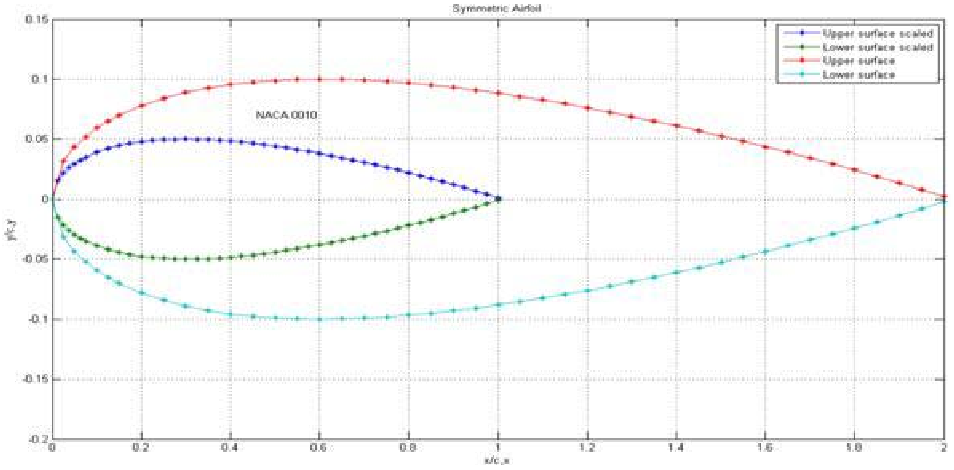

Figure 53. Symmetric Airfoil NACA 0010 Represented in MATLAB, in Actual and Dimensionless Scale

THIS PAGE INTENTIONALLY LEFT BLANK

APPENDIX D. EXPERIMENTAL DATA

The experimental raw data for the test plans used is shown below. For each speed and load state, five or six sample values were recorded and then numerically averaged. In the following tables, bulk data for individual temperatures and pressures is omitted, but it is available electronically at TPL of NPS. The values listed below are those used for sketching the experimental plots, paragraph V.

Table 14. Experimental Data for Horizontal Inlet CFF, No Cavities (Blanked off), 22- vs. 30-Bladed Rotor, Test Plan A.

RPM-Notch	RPM_cor	efficiency	m_dot_corr [kg/s]	F_corr [N]	P_corr [Watt]	mdot/L	F/P	Pt_ratio	F/L
CFF Horizontal Inlet No Cavities (blanked off) 22-bladed rotor, Experimental Averaged Results									
3007.21 - 0	2999.647	0.736095	0.086072	3.06126	80.89549	1.008346	2.259107	0.037842	80.34804
3018.24 - 1	3013.085	0.7235	0.086403	3.09277	83.62858	1.008452	2.267797	0.036982	81.17505
3014.27 - 2	3008.868	0.72086	0.085015	3.0351	81.99251	1.008389	2.231359	0.037017	79.66142
3029.07 - $2^{1/2}$	3021.688	0.72364	0.083634	2.979054	79.59735	1.008316	2.195118	0.037427	78.19038
3020.51 - 3	3014.134	0.732063	0.079797	2.811879	73.27925	1.008105	2.094408	0.038372	73.8026
3007.68 - $3^{1/2}$	3001.502	0.761524	0.071035	2.44456	59.86972	1.007642	1.864447	0.040831	64.16167
3006.50 - 4	2999.234	0.608082	0.055601	1.778102	48.9945	1.006469	1.459349	0.036292	46.66934
2993.38 - $4^{1/3}$	2984.799	0.446885	0.037375	1.053202	34.21984	1.004935	0.980976	0.030778	27.64309
3010.36 - $4^{2/3}$	3002.007	0.19648	0.011052	0.244246	13.8522	1.002968	0.290081	0.017632	6.410667
4025.41 - 0	4015.372	0.751324	0.117433	5.689515	199.6364	1.015468	3.082236	0.028499	149.3311
4021.77 - 1	4012.082	0.7651	0.116838	5.651342	194.6216	1.015427	3.066617	0.029038	148.3292
4017.79 - 2	4007.293	0.740967	0.114205	5.481713	192.8818	1.01515	2.997494	0.02842	143.877
4025.39 - $2^{1/2}$	4012.747	0.744882	0.11096	5.270946	182.2656	1.014811	2.912328	0.028919	138.345
4031.33 - 3	4016.386	0.756063	0.105586	4.996998	168.4303	1.014607	2.771295	0.029668	131.1548
4019.06 - $3^{1/2}$	4004.434	0.783663	0.095787	4.498612	143.5892	1.014226	2.514093	0.03133	118.0738
4023.36 - 4	4008.203	0.689469	0.074337	3.203874	104.7999	1.011759	1.951114	0.030571	84.09119
4025.32 - $4^{1/3}$	4010.17	0.578581	0.054788	2.142171	74.67164	1.009532	1.437993	0.028688	56.22496
4022.77 - $4^{2/3}$	4007.744	0.296548	0.022661	0.681554	34.93685	1.005521	0.594771	0.019508	17.88856
5017.73 - 0	4998.537	0.758747	0.146291	8.850488	383.8867	1.024196	3.83966	0.023055	232.2963
5030.94 - 1	5007.809	0.760535	0.146281	8.851271	383.1933	1.024203	3.839383	0.023099	232.3168
5040.41 - 2	5018.306	0.752077	0.143724	8.69085	378.7709	1.024078	3.772283	0.022945	228.1063
5028.47 - $2^{1/2}$	5004.294	0.766859	0.139725	8.368675	353.8689	1.023593	3.66733	0.023649	219.6503
5032.57 - 3	5010.935	0.77467	0.135492	8.111232	337.7588	1.023453	3.556233	0.024015	212.8932
5030.59 - $3^{1/2}$	5009.228	0.817963	0.123001	7.302576	282.6445	1.022827	3.228363	0.025837	191.6687
5043.45 - 4	5023.624	0.722722	0.095655	5.243842	208.3974	1.019099	2.51064	0.025163	137.6336
5031.48 - $4^{1/3}$	5010.18	0.616274	0.066767	3.27542	134.2742	1.015012	1.752424	0.024394	85.96902
5037.24 - $4^{2/3}$	5015.034	0.300083	0.023633	0.886265	55.60188	1.008531	0.620281	0.015939	23.26155
6000.63 - 0	5970.984	0.78127	0.176496	12.93851	659.3501	1.035606	4.632437	0.019623	339.5934
6027.64 - 1	5994.19	0.767274	0.176514	12.96019	672.9724	1.03569	4.63291	0.019258	340.1624
6043.10 - 2	6010.394	0.77523	0.173278	12.66881	647.2824	1.035331	4.547987	0.019572	332.5146
6036.23 - $2^{1/2}$	6003.53	0.765876	0.169625	12.30311	629.5766	1.034674	4.452088	0.019542	322.9162
6039.01 - 3	6003.512	0.787859	0.162721	11.73515	578.1808	1.034134	4.270903	0.020297	308.0091
6023.89 - $3^{1/2}$	5991.056	0.805277	0.148075	10.47622	491.2349	1.032529	3.886475	0.021326	274.9663
6030.35 - 4	5998.893	0.75424	0.114901	7.51086	341.5216	1.027251	3.015771	0.021992	197.1354
6030.47 - $4^{1/3}$	5996.064	0.624498	0.083877	4.956007	241.6454	1.021848	2.201489	0.020509	130.0789
6030.72 - $4^{2/3}$	5996.699	0.30942	0.029153	1.298629	93.81243	1.012058	0.76518	0.013843	34.08474
7059.35 - 0	7017.499	0.778603	0.205552	17.67996	1059.55	1.049177	5.395063	0.016686	464.0408
7033.17 - 1	6987.22	0.77393	0.204658	17.53956	1052.274	1.048774	5.37161	0.016668	460.3559
7058.29 - 2	7011.877	0.773415	0.202176	17.29174	1034.512	1.048502	5.306458	0.016715	453.8514
7040.12 - $2^{1/2}$	6992.186	0.771732	0.195816	16.55957	979.8865	1.047312	5.13954	0.016899	434.6345
7046.21 - 3	7000.029	0.7853	0.190441	16.05475	927.1283	1.046824	4.998457	0.017317	421.3845
7027.17 - $3^{1/2}$	6976.024	0.814108	0.172754	14.3243	777.4615	1.044847	4.534233	0.018424	375.9658
7044.06 - 4	6994.886	0.765761	0.138349	10.76155	572.863	1.038724	3.631196	0.018786	282.4555
7040.12 - $4^{1/3}$	6990.697	0.641394	0.097832	6.773498	376.2554	1.030041	2.567776	0.018002	177.7821
7030.62 - $4^{2/3}$	6983.271	0.345115	0.043231	2.306332	179.0283	1.017332	1.134673	0.012882	60.53364
8016.10 - 0	7960.901	0.783506	0.232174	22.72783	1534.998	1.063821	6.093807	0.014806	596.5311
8039.63 - 1	7986.311	0.779998	0.231962	22.7312	1545.355	1.064024	6.088237	0.014709	596.6194

8037.06 - 2	7981.604	0.780102	0.228553	22.2467	1498.406	1.062992	5.998762	0.014847	583.9028
8056.23 - $2^{1/2}$	7996.179	0.780894	0.224407	21.78975	1459.983	1.062568	5.889956	0.014925	571.9094
8032.68 - 3	7973.471	0.79424	0.216383	20.89414	1362.373	1.061563	5.679342	0.015337	548.4026
8040.14 - $3^{1/2}$	7980.551	0.807508	0.196382	18.6321	1164.45	1.058895	5.154379	0.016001	489.0315
8039.52 - 4	7978.62	0.738804	0.151615	13.24539	818.2594	1.048876	3.97939	0.016187	347.648
8022.468 - $4^{1/3}$	7961.033	0.648051	0.11435	9.091484	574.0539	1.039753	3.001321	0.015837	238.6216
8066.163 - $4^{2/3}$	8003.709	0.329311	0.038414	2.292463	208.0665	1.021608	1.008236	0.011018	60.16963
RPM-Notch	RPM_cor	efficiency	m_dot_c orr [kg/s]	F_corr [N]	P_corr [Watt]	mdot/L	F/P	Pt_ratio	F/L
CFF Horizontal Inlet No Cavities (blanked off) 30-bladed rotor, Experimental Averaged Results									
3035.53 - 0	3018.571	0.678369	0.090135	3.389531	102.4186	1.009313	2.365754	0.033095	88.96407
3008.18 - 1	2991.295	0.648576	0.089823	3.340289	104.4277	1.009107	2.357557	0.031987	87.67163
3005.02 - 2	2988.566	0.711374	0.088277	3.282421	93.45269	1.009066	2.316984	0.035124	86.15278
3018.86 - $2^{1/2}$	3002.908	0.648244	0.085916	3.167982	97.67124	1.008902	2.255006	0.032435	83.14914
3002.72 - 3	2987.506	0.681889	0.081901	2.990619	87.37889	1.008675	2.14964	0.034226	78.49395
3028.11 - $3^{1/2}$	3012.749	0.641735	0.074929	2.692665	80.50395	1.008327	1.966631	0.033448	70.67363
3016.32 - 4	3000.15	0.606166	0.057794	1.955728	57.12071	1.007237	1.516913	0.034239	51.33143
2999.72 - $4^{1/3}$	2985.369	0.44339	0.040322	1.209777	42.07508	1.005583	1.058313	0.028753	31.75268
3020.48 - $4^{2/3}$	3004.467	0.232103	0.016067	0.400203	21.57233	1.00376	0.421701	0.018552	10.50402
4016.12 - 0	3990.756	0.739123	0.121035	6.127445	228.3834	1.016898	3.176769	0.02683	160.8253
4025.70 - 1	3999.253	0.763772	0.122149	6.232816	226.1407	1.017134	3.206003	0.027562	163.591
4026.82 - 2	4001.028	0.725163	0.119526	6.03956	228.5256	1.016795	3.137156	0.026428	158.5186
4013.39- $2^{1/2}$	3986.909	0.721306	0.116272	5.805721	217.4666	1.016346	3.051765	0.026697	152.3811
4009.86 - 3	3983.222	0.725321	0.111233	5.516018	202.9034	1.016033	2.9195	0.027185	144.7774
4034.79 - $3^{1/2}$	4009.685	0.709719	0.101345	4.921226	179.7749	1.01525	2.659976	0.027374	129.166
4039.02 - 4	4015.366	0.703109	0.075096	3.453477	117.8596	1.013358	1.971014	0.029302	90.64243
4021.10 - $4^{1/3}$	3995.77	0.551576	0.056496	2.342148	90.66116	1.010706	1.482846	0.025834	61.47371
4059.09 - $4^{2/3}$	4033.967	0.308983	0.01653	0.542737	28.93425	1.006515	0.433854	0.018758	14.24507
4985.28 - 0	4957.092	0.779387	0.15264	9.776305	435.9186	1.027074	4.006298	0.022427	256.5959
5024.33 - 1	4992.435	0.743622	0.152721	9.820055	460.0848	1.027255	4.008436	0.021344	257.7442
5024.78 - 2	4994.373	0.760384	0.150277	9.670457	443.4924	1.027303	3.944284	0.021805	253.8178
5043.87 - $2^{1/2}$	5012.17	0.763496	0.147111	9.369308	422.4141	1.026667	3.861183	0.02218	245.9136
5013.92 - 3	4983	0.789014	0.139552	8.77008	375.3287	1.025795	3.662777	0.023366	230.1858
5035.85 - $3^{1/2}$	5007.519	0.743533	0.130297	8.042631	355.9192	1.024687	3.419869	0.022597	211.0927
5030.18 - 4	5001.016	0.771106	0.101115	5.946602	237.0382	1.021949	2.653927	0.025087	156.0788
5020.42 - $4^{1/3}$	4989.13	0.62798	0.074749	3.928153	169.4089	1.017251	1.961919	0.023187	103.1011
5048.14 - $4^{2/3}$	5017.369	0.305656	0.022065	0.879213	57.55692	1.009641	0.579137	0.015276	23.07645
6043.64 - 0	5999.762	0.805789	0.185388	14.57285	769.8051	1.040897	4.865826	0.018931	382.4896
6036.95 - 1	5992.913	0.810482	0.185464	14.59261	766.4289	1.040942	4.867813	0.01904	383.0081
6036.83 - 2	5996.463	0.801276	0.181865	14.1924	747.7138	1.040255	4.773351	0.018981	372.5038
6025.99 - $2^{1/2}$	5983.88	0.796502	0.17733	13.7176	718.0839	1.039405	4.654327	0.019103	360.0419
6051.87 - 3	6009.703	0.794314	0.170934	13.11682	679.9188	1.038591	4.486458	0.019292	344.2736
6046.70 - $3^{1/2}$	6003.05	0.788682	0.156003	11.63247	585.944	1.036151	4.094565	0.019853	305.3143
6033.39 - 4	5995.084	0.762116	0.115944	8.075533	384.3149	1.030772	3.043146	0.021013	211.9562
6034.73 - $4^{1/3}$	5993.711	0.6093	0.083105	5.181826	271.9944	1.024234	2.181246	0.019051	136.0059
6037.68 - $4^{2/3}$	5995.124	0.348459	0.035703	1.753505	123.9091	1.01465	0.937077	0.014152	46.02375
6983.121 - 0	6928.127	0.819549	0.214629	19.66935	1188.966	1.05578	5.633308	0.016543	516.2559
6976.732 - 1	6922.256	0.828183	0.215053	19.76592	1183.699	1.056007	5.644427	0.016698	518.7906
6945.164 - 2	6896.088	0.819788	0.209872	19.06647	1139.396	1.054655	5.508455	0.016734	500.4322
6947.776 - $2^{1/2}$	6895.802	0.80732	0.204784	18.44667	1108.838	1.05367	5.374895	0.016636	484.1646
6956.027 - 3	6901.126	0.804747	0.196871	17.49839	1037.623	1.052048	5.167231	0.016864	459.2753
6979.152 - $3^{1/2}$	6923.462	0.80343	0.180747	15.72075	905.2566	1.049332	4.744027	0.017366	412.6181
7052.067 - 4	6997.251	0.813201	0.143294	11.9477	639.8637	1.044444	3.76099	0.018672	313.5879
7025.919 - $4^{1/3}$	6970.998	0.617124	0.098744	7.106514	425.4184	1.032406	2.591707	0.016705	186.5227
7044.619 - $4^{2/3}$	6988.714	0.372146	0.041715	2.432041	191.1992	1.020698	1.094886	0.01272	63.8331
7994.163 - 0	7931.552	0.823185	0.244957	25.88295	1791.586	1.074448	6.429306	0.014447	679.3425
8024.859 - 1	7970.048	0.837114	0.245034	26.01729	1780.186	1.075213	6.431341	0.014615	682.8685
8053.754 - 2	7995.657	0.833332	0.243038	25.82015	1772.265	1.075152	6.378943	0.014569	677.6943
8059.724 - $2^{1/2}$	7999.027	0.82286	0.237984	25.07972	1724.615	1.073714	6.246303	0.014542	658.2603
8057.608 - 3	7991.012	0.827334	0.227732	23.62495	1584.836	1.071113	5.97722	0.014907	620.0775
8076.223 - $3^{1/2}$	8008.417	0.814153	0.208077	21.03422	1385.849	1.066875	5.461328	0.015178	552.0794
8077.343 - 4	8009.369	0.813254	0.166569	16.00576	987.8773	1.059336	4.371879	0.016202	420.0987
8038.309 - $4^{1/3}$	7971.72	0.656681	0.117514	9.946438	657.5445	1.044981	3.084355	0.015127	261.0614
8043.010 - $4^{2/3}$	7976.671	0.35244	0.050928	3.331714	309.1443	1.026016	1.336688	0.010777	87.44656

Table 15. Experimental Data for Horizontal Inlet CFF, With Cavities, 22- vs. 30-Bladed Rotor, Test Plan B.

RPM-Notch	RPM_cor	efficiency	m_dot_corr [kg/s]	F_corr [N]	P_corr [Watt]	mdot/L	F/P	Pt_ratio	F/L
CFF Horizontal Inlet With Cavities 22-bladed rotor, Experimental Averaged Results									
3022.482 - 0	3010.163	0.58461	0.101619	4.085388	154.2111	1.01072	2.667166	0.026492	107.228
3022.071 - 1	3010.852	0.565311	0.101413	4.079302	159.2035	1.010723	2.661759	0.025623	107.0683
3024.497 - 2	3014.378	0.635871	0.100041	4.033651	141.1742	1.01075	2.625752	0.028572	105.8701
3016.952 - $2^{1/2}$	3006.305	0.565892	0.097266	3.892427	150.1689	1.010562	2.552913	0.02592	102.1635
3018.312 - 3	3006.888	0.590579	0.092939	3.710537	135.8745	1.01044	2.439336	0.027309	97.38943
3016.733 - $3^{1/2}$	3004.319	0.593562	0.085742	3.40399	122.4643	1.01024	2.25045	0.027796	89.34358
3025.950 - 4	3012.765	0.610052	0.063513	2.449187	80.74763	1.009371	1.666998	0.030331	64.28312
3026.695 - $4^{1/2}$	3012.635	0.384307	0.039794	1.179865	46.81249	1.005457	1.044459	0.025204	30.96758
3049.938 - $4^{2/3}$	3035.717	0.224467	0.014422	0.364508	20.90082	1.003926	0.378521	0.01744	9.567149
4041.471 - 0	4021.858	0.629047	0.136527	7.452576	354.1757	1.019801	3.58339	0.021042	195.6057
4024.663 - 1	4008.257	0.645288	0.136596	7.44006	343.3399	1.019678	3.585185	0.02167	195.2772
4031.691 - 2	4014.277	0.624731	0.134841	7.347959	350.0942	1.019679	3.539146	0.020989	192.8598
4036.234 - $2^{1/2}$	4014.931	0.633512	0.131703	7.131237	332.0857	1.019378	3.456766	0.021474	187.1716
4026.479 - 3	4007.631	0.619273	0.127769	6.86809	323.701	1.01901	3.353509	0.021217	180.2648
4035.960 - $3^{1/2}$	4017.439	0.640462	0.120125	6.405418	286.8709	1.018538	3.152885	0.022329	168.1212
4052.523 - 4	4032.259	0.679929	0.091029	4.685434	185.7287	1.016817	2.389214	0.025227	122.9773
4037.296 - $4^{1/3}$	4017.662	0.585175	0.065416	2.813749	107.4093	1.011573	1.716967	0.026197	73.85169
4040.882 - $4^{2/3}$	4017.824	0.267787	0.030436	1.0025	63.59907	1.006764	0.798849	0.015763	26.31234
5028.361 - 0	5011.52	0.693211	0.172624	11.97004	659.1906	1.031966	4.530815	0.018159	314.1743
5056.474 - 1	5026.567	0.64961	0.172156	11.91605	692.7126	1.031849	4.518532	0.017202	312.7572
5042.945 - 2	5014.069	0.64455	0.169033	11.59758	671.7864	1.031205	4.436568	0.017264	304.3985
5041.095 - $2^{1/2}$	5011.408	0.651635	0.166688	11.39453	649.664	1.03092	4.375025	0.017539	299.069
5039.479 - 3	5013.939	0.641075	0.160819	10.95391	629.1163	1.030546	4.220974	0.017412	287.5042
5044.440 - $3^{1/2}$	5016.423	0.652842	0.147841	9.992127	553.9353	1.029786	3.880337	0.018038	262.2606
5055.713 - 4	5026.907	0.705084	0.120208	7.919108	388.4081	1.027712	3.155069	0.020389	207.8506
5034.482 - $4^{1/3}$	5006.086	0.52003	0.075676	3.913397	200.5564	1.016707	1.986254	0.019513	102.7138
5038.064 - $4^{2/3}$	5004.609	0.270644	0.030102	1.241528	96.8354	1.010558	0.790067	0.012821	32.58605
6001.718 - 0	5967.584	0.662352	0.204812	17.05026	1165.093	1.046132	5.375641	0.014634	447.5134
6030.952 - 1	5986.979	0.668525	0.204901	17.10864	1161.015	1.046387	5.377987	0.014736	449.0456
6027.663 - 2	5981.643	0.666147	0.20309	16.89224	1145.224	1.045994	5.330449	0.01475	443.3659
6031.862 - $2^{1/2}$	5985.888	0.660172	0.199164	16.48685	1117.98	1.045367	5.227404	0.014747	432.7258
6035.326 - 3	5989.689	0.65404	0.191839	15.75537	1064.609	1.044423	5.035148	0.014799	413.5269
6015.534 - $3^{1/2}$	5969.77	0.655165	0.190654	15.59738	1049.133	1.04412	5.004037	0.014867	409.3801
6032.939 - 4	5985.517	0.668779	0.179816	14.63719	951.7475	1.043307	4.719578	0.015379	384.1783
6048.744 - $4^{1/3}$	6002.579	0.704451	0.145696	11.51186	677.2011	1.040014	3.824049	0.016999	302.1485
6064.499 - $4^{2/3}$	6017.591	0.486932	0.082155	4.973783	317.1997	1.022831	2.156291	0.01568	130.5455
7013.885 - 0	6960.059	0.680709	0.23927	23.43523	1826.308	1.064009	6.28004	0.012832	615.098
7047.266 - 1	6993.014	0.677859	0.239494	23.53967	1847.358	1.064434	6.285938	0.012742	617.8391
7049.415 - 2	6998.805	0.706523	0.238315	23.40407	1763.811	1.06435	6.254985	0.013269	614.2801
7066.484 - $2^{1/2}$	7018.176	0.682132	0.233274	22.87525	1776.717	1.064014	6.122673	0.012875	600.4003
7041.306 - 3	6988.078	0.672003	0.224989	21.73961	1680.945	1.061816	5.905229	0.012933	570.5935
7038.074 - $3^{1/2}$	6983.308	0.674975	0.211682	20.31582	1541.804	1.060502	5.555966	0.013177	533.2236
7033.683 - 4	6975.361	0.723446	0.165062	15.11147	1000.447	1.053839	4.332347	0.015105	396.6266
7033.835 - $4^{1/3}$	6976.776	0.528756	0.09933	7.101852	492.9037	1.03197	2.607092	0.014408	186.4003
7042.010 - $4^{2/3}$	6969.037	0.282938	0.031218	1.789699	184.2787	1.020338	0.81937	0.009712	46.97374
8024.296 - 0	7957.237	0.686308	0.272971	30.73004	2722.143	1.084925	7.164592	0.011289	806.5628
8037.683 - 1	7975.154	0.677384	0.273032	30.71112	2749.665	1.084641	7.166187	0.011169	806.0661
8001.528 - 2	7936.053	0.673496	0.268551	29.95156	2672.279	1.083109	7.04857	0.011208	786.1303
8048.320 - $2^{1/2}$	7981.862	0.673498	0.26558	29.60072	2635.685	1.082878	6.970604	0.011231	776.9219
8043.385 - 3	7974.766	0.663515	0.256417	28.34853	2530.142	1.081138	6.730098	0.011204	744.0558
8063.892 - $3^{1/2}$	7990.229	0.676436	0.241199	26.58096	2303.217	1.080018	6.330695	0.011541	697.6631
8051.052 - 4	7977.745	0.722376	0.189861	19.91961	1510.625	1.070987	4.983216	0.013186	522.8245
8047.624 - $4^{1/3}$	7977.936	0.492969	0.110569	8.998354	757.82	1.04131	2.902068	0.011874	236.1773
8046.618 - $4^{2/3}$	7940.019	0.275017	0.036091	2.198056	254.6191	1.023576	0.947264	0.008633	57.69177
RPM-Notch	RPM_cor	efficiency	m_dot_corr [kg/s]	F_corr [N]	P_corr [Watt]	mdot/L	F/P	Pt_ratio	F/L
CFF Horizontal Inlet With Cavities 30-bladed rotor, Experimental Averaged Results									
3021.565 - 0	3011.778	0.605095	0.105017	4.48376	172.9788	1.012051	2.756358	0.025921	117.684
3014.495 - 1	3005.522	0.710047	0.1037	4.452212	146.9879	1.012152	2.721772	0.03029	116.8559
3018.651 - 2	3008.439	0.625009	0.102606	4.395402	163.6793	1.012064	2.693069	0.026854	115.3649
3019.994 - $2^{1/2}$	3012.708	0.690464	0.100444	4.301515	147.7852	1.012036	2.636332	0.029107	112.9007
3018.195 - 3	3009.298	0.624264	0.0962	4.095806	150.846	1.011842	2.524934	0.027152	107.5015
3009.588 - $3^{1/2}$	2998.859	0.632392	0.088908	3.742386	133.2608	1.011466	2.333544	0.028083	98.22537
3011.112 - 4	2999.824	0.649223	0.071574	2.914135	95.78283	1.010506	1.878586	0.030424	76.48648
3023.395 - $4^{1/3}$	3011.446	0.544931	0.04941	1.707915	55.95434	1.007454	1.296854	0.030523	44.82717

3006.089 - $4^{2/3}$	2993.307	0.243895	0.020947	0.562757	31.65324	1.004447	0.549778	0.017779	14.77051
4010.145 - 0	3995.089	0.735031	0.139194	8.11467	349.6549	1.022419	3.653377	0.023208	212.9835
4024.978 - 1	4008.247	0.738763	0.140595	8.251792	358.153	1.02269	3.690164	0.02304	216.5825
4013.352 - 2	3994.431	0.728527	0.137571	8.014098	347.8664	1.022331	3.610788	0.023038	210.3438
4038.742 - $2^{1/2}$	4024.995	0.68625	0.135182	7.917038	365.2933	1.022499	3.548084	0.021673	207.7963
4046.986 - 3	4029.614	0.720149	0.130596	7.633097	333.4775	1.022322	3.427717	0.022889	200.3438
3991.004 - $3^{1/2}$	3969.338	0.727725	0.120144	6.816932	283.7363	1.02086	3.153374	0.024026	178.9221
4013.707 - 4	3997.416	0.7443	0.095794	5.279848	204.869	1.019295	2.514284	0.025772	138.5787
4013.347 - $4^{1/3}$	3997.556	0.566562	0.065028	3.000715	125.9408	1.013282	1.70677	0.023826	78.75893
4037.225 - $4^{2/3}$	4019.389	0.29115	0.03121	1.124843	71.27247	1.008024	0.819172	0.015782	29.52344
5016.864 - 0	4990.368	0.752358	0.17544	13.02235	696.0222	1.036391	4.604734	0.01871	341.7939
5024.343 - 1	4991.67	0.734869	0.174524	12.89928	702.5306	1.036099	4.580685	0.018361	338.5637
5028.979 - 2	5001.604	0.744337	0.172782	12.76967	686.6303	1.036065	4.534952	0.018598	335.1618
5019.876 - $2^{1/2}$	4992.928	0.738318	0.169112	12.46619	670.8932	1.035724	4.438644	0.018581	327.1967
5039.505 - 3	5013.875	0.769503	0.164326	12.11495	626.5916	1.03562	4.31301	0.019335	317.9776
5029.274 - $3^{1/2}$	4999.486	0.753448	0.150685	10.90148	557.6177	1.034001	3.95498	0.01955	286.1282
5030.118 - 4	5000.676	0.777679	0.120006	8.329208	388.5506	1.030667	3.149761	0.021437	218.6144
5018.849 - $4^{1/3}$	4989.711	0.53608	0.074415	3.942396	200.4727	1.017515	1.953138	0.019665	103.4749
5053.190 - $4^{2/3}$	5018.254	0.299935	0.023772	1.034695	77.99504	1.011907	0.623944	0.013266	27.15734
6024.818 - 0	5988.293	0.752567	0.208972	18.78153	1211.981	1.053581	5.48483	0.015497	492.9536
6042.878 - 1	6002.064	0.752755	0.209441	18.86293	1217.922	1.053746	5.497134	0.015488	495.0899
6033.308 - 2	5989.925	0.753555	0.207768	18.65517	1197.267	1.053306	5.453239	0.015581	489.6371
6031.485 - $2^{1/2}$	5993.297	0.757363	0.204858	18.38847	1172.315	1.053187	5.376863	0.015686	482.637
6035.568 - 3	6000.778	0.761808	0.198111	17.69872	1112.493	1.052482	5.199763	0.015909	464.5333
6047.972 - $3^{1/2}$	6006.635	0.7622	0.187243	16.56419	1022.787	1.051073	4.914524	0.016195	434.7557
6032.280 - 4	5991.625	0.801186	0.15101	12.79573	707.8745	1.045988	3.963514	0.018076	335.846
6044.648 - $4^{1/3}$	6005.276	0.671751	0.108143	7.871052	440.153	1.033335	2.838387	0.017883	206.5893
6038.247 - $4^{2/3}$	5983.206	0.259102	0.039323	1.864342	179.3583	1.014321	1.032106	0.010395	48.93286
7012.079 - 0	6958.444	0.767256	0.243795	25.74022	1908.189	1.074248	6.39882	0.013489	675.5964
7046.764 - 1	6992.459	0.754575	0.244548	25.93815	1960.355	1.074803	6.418588	0.013231	680.7914
7053.061 - 2	7001.38	0.760298	0.242416	25.66481	1921.986	1.074536	6.362628	0.013353	673.617
7039.549 - $2^{1/2}$	6992.664	0.766374	0.2384	25.1531	1861.297	1.073847	6.257227	0.013514	660.1863
7063.803 - 3	7019.716	0.755379	0.230687	24.2988	1810.248	1.073259	6.054764	0.013423	637.7637
7044.865 - $3^{1/2}$	6996.292	0.771766	0.21676	22.53432	1610.886	1.070831	5.689246	0.013989	591.452
7050.943 - 4	7001.336	0.805818	0.169752	16.72068	1066.113	1.062321	4.45542	0.015684	438.8631
7038.527 - $4^{1/3}$	6990.764	0.657366	0.119287	10.05632	662.2389	1.044661	3.130897	0.015185	263.9454
7012.079 - $4^{2/3}$	6958.444	0.767256	0.243795	25.74022	1908.189	1.074248	6.39882	0.013489	675.5964
8029.742 - 0	7965.587	0.769596	0.277322	33.76618	2867.258	1.099204	7.278791	0.011776	886.2515
8060.890 - 1	7995.261	0.760721	0.277353	33.77546	2901.872	1.09923	7.279606	0.011639	886.4949
8054.138 - 2	7989.952	0.766068	0.275844	33.58049	2859.456	1.098994	7.239993	0.011744	881.3777
8064.921 - $2^{1/2}$	8004.998	0.774406	0.272368	33.14306	2786.356	1.098759	7.148767	0.011895	869.8965
8046.298 - 3	7984.897	0.769822	0.261837	31.62725	2645.054	1.096882	6.872365	0.011957	830.1115
8062.771 - $3^{1/2}$	7999.87	0.775594	0.247438	29.5841	2412.477	1.094119	6.494433	0.012263	776.4856
8044.581 - 4	7981.843	0.811144	0.195424	22.07742	1601.312	1.082405	5.129248	0.013787	579.4599
8052.005 - $4^{1/3}$	7991.26	0.548136	0.118984	10.1973	815.3527	1.045984	3.122931	0.012507	267.6456
8068.259 - $4^{2/3}$	7963.59	0.259904	0.024615	1.510976	195.7831	1.025133	0.64605	0.007718	39.65816

LIST OF REFERENCES

[1] Moller International, “Technology,” http://www.moller.com/ (accessed May 10, 2010), n.d.

[2] P. Peebles, “Aerodynamic lift generating device,” U.S. Patent B1 6 527 229, March 15, 2003 [Online]. Available: www.fanwing.com (accessed May 10, 2010).

[3] J. Kummer, “Simulation of the cross flow fan and application to a propulsive airfoil concept,” PhD dissertation, Syracuse University, Syracuse, NY, 2006.

[4] J. Kummer and T. Dang, “High lift propulsive airfoil with integrated crossflow fan,” *Journal of Aircraft*, vol. 43, no. 4, pp. 1059–1068, July-August 2006.

[5] J. Kummer, “Propulsive wing,” www.propulsivewing.com (accessed May 10, 2010).

[6] C. Gologan, S. Mores, H. Steiner, and A. Seitz, “Potential of the cross-flow fan for powered-lift regional aircraft applications,” presented at the 9th AIAA Aviation Technology, Integration, and Operations Conference (ATIO), September 23, 2009.

[7] Naval Air Systems Command contract N00019-74-C-0434, *Multi-Bypass Ratio System Technology Development*, vol. I-III, Vought Systems Division, LTV Aerospace Corporation, July 24, 1975.

[8] M. Seaton, “Performance measurements, flow visualization, and numerical simulation of a cross flow fan,” M.S. thesis, Naval Postgraduate School, Monterey, CA, 2003.

[9] W. Cheng, “Experimental and numerical analysis of a cross flow fan,” M.S. thesis, Naval Postgraduate School, Monterey, CA, 2003.

[10] C. Schreiber, “Effect of span variation on the performance of a cross flow fan,” M.S. thesis, Naval Postgraduate School, Monterey, CA, 2006.

[11] H. Yu, “Experimental investigation and numerical prediction of a cross flow fan,” M.S. thesis, Naval Postgraduate School, Monterey, CA, 2006.

[12] J. Ulvin, “Experimental investigation of a six inch diameter, four inch span cross-flow fan,” M.S. thesis, Naval Postgraduate School, Monterey, CA, 2008.

[13] S. Cordero, “Investigation of performance improvements including application of inlet guide vanes to a cross flow fan,” M.S. thesis, Naval Postgraduate School, Monterey, CA, 2009.

[14] A. Gannon, J. M. Utschig, G. V. Hobson, and M. F. Platzer, “Experimental investigation of a small-scale cross-flow fan for aircraft propulsion,” presented at the ISROMAC Conference, February 2006.

[15] P. Mortier, “Fan or blowing apparatus,” U.S. Patent 507,445, October 24, 1893.

[16] H. Vesteeg, and W. Malalasekera, *An Introduction to Computational Fluid Dynamics*, *Second Edition*. London: Pearson, 2007.

[17] I. Abbot, and A. Von Doenhoff, *Theory of Wing Sections*. New York, NY: Dover, 1959.

[18] F. White, *Fluid Mechanics*, *Sixth Edition*. New York, NY: McGraw-Hill, 2008.

INITIAL DISTRIBUTION LIST

1. Defense Technical Information Center
   Ft. Belvoir, Virginia

2. Dudley Knox Library
   Naval Postgraduate School
   Monterey, California

3. M.F. Platzer
   Department of Mechanical and Aerospace Engineering
   Naval Postgraduate School
   Monterey, California

4. Garth V. Hobson
   Department of Mechanical and Aerospace Engineering
   Naval Postgraduate School
   Monterey, California

5. M.S. Chandrasechara
   Department of Mechanical and Aerospace Engineering
   Naval Postgraduate School
   Monterey, California

6. Anthony Gannon
   Department of Mechanical and Aerospace Engineering
   Naval Postgraduate School
   Monterey, California